

CONSTRAINED DROP SURFACTOMETER FOR STUDYING
INTERFACIAL STRUCTURE AND RHEOLOGY

A DISSERTATION SUBMITTED TO THE GRADUATE DIVISION OF THE
UNIVERSITY OF HAWAI'I AT MANOA IN PARTIAL FULFILLMENT
OF THE REQUIREMENTS FOR THE DEGREE OF

DOCTOR OF PHILOSOPHY

IN

MECHANICAL ENGINEERING

DECEMBER 2017

By

Jinlong Yang

Dissertation Committee:

Yi Zuo, Chairperson
Marcelo H. Kobayashi
Lloyd H. Hihara
John S. Allen
Zhengqing Yun

Keywords: axisymmetric drop shape analysis, constrained drop surfactometer, Neumann number,
surface dilational rheology, surface tension

Acknowledgements

I would like to express my sincere gratitude to my supervisor Dr. Yi Zuo for assistant and guidance in this work. I have learned much under his supervision and I truly appreciate the support he has given me throughout my study at the University of Hawaii.

I need to acknowledge committee members for their time and effort in serving on my dissertation committee.

I would like to thank my colleagues Kyle Yu, Tomoaki Tsuji, Rohan Jha, and Dayne Sasaki for their invaluable help and friendship.

I am truly grateful of my friends and family who supported me during my time at the University of Hawaii.

Finally, I would like to acknowledge the financial support from the NSF under the grant number CBET-1254795.

Abstract

Measurements of surface tension and interfacial rheology of liquid-fluid surfaces play an important role in a variety of scientific and industrial fields, such as smart material, thin film, soft matter, microfluidics, and biophysics. Being a miniaturized experimental platform for studying surface phenomena, droplets hold great advantages over the traditional experimental methods, such as the classical Langmuir trough, in determining surface tension and interfacial rheological properties. The focus of this thesis was to develop a novel droplet-based experimental platform called the constrained drop surfactometer (CDS) for studying surface tension and interfacial rheology. Axisymmetric drop shape analysis (ADSA) was used as a numerical algorithm to determine the dynamic surface tension as a function of time and surface area variations. We first proposed a new dimensionless parameter, called the Neumann number, $Ne \equiv \Delta\rho g R_0 H / \gamma$, to replace the classical Bond number for evaluating the accuracy of ADSA upon reducing drop volume. We then developed a closed-loop ADSA (CL-ADSA) algorithm for determining and controlling droplet parameters, including the volume, surface area, and surface tension, in real-time. With the CL-ADSA, the CDS was transformed from a traditional surface tension measurement methodology to a sophisticated experimental platform for manipulating millimeter-sized single droplets in real-time. We have demonstrated the accuracy, robustness, versatility, and automation of this droplet manipulation technique. Finally, we engaged the combination of CDS and CL-ADSA in studying interfacial rheology. Understanding the interfacial rheology of complex fluids plays a central role in a range of applications such as food processing, detergency, coating, cosmetic, and pharmacology. For the first time, our methodological advance permitted direct control of surface area oscillated in a sinusoidal pattern, thus resulting in a precise evaluation of the surface dilational rheological properties of complex

fluids, including surfactants and proteins. Our results showed that the CDS, together with the CL-ADSA, holds great promise for advancing the study of interfacial structure and rheology.

Table of Contents

Acknowledgements	i
Abstract.....	ii
List of Tables	vii
List of Figures.....	viii
List of Abbreviations	xiii
Chapter 1. Measurement of surface and interfacial tensions.....	1
1.1 Introduction.....	1
1.2 Axisymmetric drop shape analysis (ADSA).....	3
1.2.1 Computational scheme for a unified drop/bubble coordinate system.....	4
1.2.2 Numerical procedure for surface/interfacial tension calculation	5
1.3 Constrained drop surfactometer (CDS)	9
1.3.1 Benchtop unit.....	9
1.3.2 Controller box	11
1.4 Surface and interfacial tension measurements with drops and bubbles.....	11
1.4.1 Test liquids.....	12
1.4.2 Results and discussion	12
1.5 Summary and scope of this dissertation.....	13
Chapter 2. Accuracy of axisymmetric drop shape analysis.....	22
2.1 Introduction.....	22
2.2 Materials and methods	25
2.2.1 Materials	25
2.2.2 Experimental methods	26
2.3 Results and discussion	26

2.3.1 Accuracy of ADSA evaluated by the capillary constant	26
2.3.2 Accuracy of ADSA evaluated by the Bond number (Bo).....	27
2.3.3 Accuracy of ADSA evaluated by the Worthington number (Wo).....	28
2.3.4 Accuracy of ADSA evaluated by the Neumann number (Ne).....	29
2.3.5 Accuracy of ADSA evaluated by the shape parameter (Ps)	31
2.3.6 Implications of the local Neumann number (Ne_z)	32
2.4 Summary	33
Chapter 3. Development of the closed-loop ADSA.....	46
3.1 Introduction.....	46
3.2 Materials and methods	48
3.2.1 Materials	48
3.2.2 Experimental methods	49
3.3 Results and discussion	51
3.3.1 Control of drop volume and its application in compensating evaporation	51
3.3.2 Control of surface area and its application in studying pulmonary surfactants	53
3.3.3 Control of surface tension/pressure	55
3.4 Summary	57
Chapter 4. Study of surface dilational rheology	65
4.1 Introduction.....	65
4.2 Materials and methods	67
4.2.1 Development of a sinusoidal waveform generator	67
4.2.2 Materials	68
4.2.3 Experimental methods	68
4.3 Results and discussion	71
4.3.1 The accuracy of sinusoidal waveform generator	71

4.3.2 Dilational modulus of surfactants	73
4.3.3 Dilational modulus of proteins.....	78
4.4 Summary	81
Chapter 5. Other research involvements.....	91
5.1 Determining the surface tension of xylem surfactants.....	91
5.1.1 Introduction.....	91
5.1.2 Materials and methods	92
5.1.3 Results and discussion	93
5.2 Development of the subphase replacement technique	94
5.2.1 Introduction.....	94
5.2.2 Materials and methods	95
5.2.3 Results and discussion	97
5.3 Phospholipid self-assembly at oil-water interfaces.....	98
5.3.1 Introduction.....	98
5.3.2 Materials and methods	99
5.3.3 Results and discussion	100
Chapter 6. Summary of main contributions and future directions	113
6.1 Summary of main contributions.....	113
6.2 Future directions	115
6.2.1 Development of high-speed ADSA	115
6.2.2. Surface dilational rheology measurement at oil-water interface	116
6.2.3 Development of the Langmuir-Schaefer transfer technique with the CDS	116
VITA.....	117
References	119

List of Tables

Table 1.1 Physicochemical properties and sources of the tested liquids.	21
Table 2.1 Various definitions of the Bond number $Bo = \left(\frac{L}{c}\right)^2$ for evaluating the accuracy of drop shape analysis.	45
Table 4.1 Fitting parameters for the adsorption isotherm and modulus of C ₁₂ DMPO	90

List of Figures

Figure 1.1 The coordinate system of numerical solution for the four commonly studied axisymmetric drop/bubble configurations	15
Figure 1.2 Procedure of ADSA using a sessile drop as example.....	16
Figure 1.3 Schematic of the experimental setup.....	17
Figure 1.4 Experimental setup of the CDS.	18
Figure 1.5 Surface tensions (in mN/m) of six test liquids, <i>i.e.</i> , water, formamide, DMSO, 1-octanol, hexadecane, and decane, each determined with four drop/bubble configurations, <i>i.e.</i> , PD, SD, SB, and PB, at room temperature (22 ± 1 °C).....	19
Figure 1.6 Interfacial tensions (in mN/m) of three oil-water systems, <i>i.e.</i> , hexadecane-water, decane-water, and 1-octanol-water, each determined with four drop/bubble configurations, <i>i.e.</i> , PD, SD, SB, and PB, at room temperature (22 ± 1 °C).	20
Figure 2.1 Example results of Surface tension-Drop volume-Contact angle-Curvature vs. Time for a sequence of static experiments conducted for a pendant drop (PD) and sessile drop (SD) of decane.	34
Figure 2.2 Example results of Surface tension-Drop volume-Contact angle-Curvature vs. Time for a sequence of static experiments conducted for a pendant drop (PD) and sessile drop (SD) of water.....	35
Figure 2.3 Example results of Surface tension-Drop volume-Contact angle-Curvature vs. Time for a sequence of static experiments conducted for a pendant drop (PD) and sessile drop (SD) of decane-water interface.	36
Figure 2.4 Relative errors of measured surface/interfacial tensions ($\Delta\gamma$) for decane, water, and decane-water systems upon reducing drop volume, using both PD and SD.	37

Figure 2.5 Reproducibility of experiments of the relative errors in measured surface/interfacial tensions ($\Delta\gamma$) upon reducing drop volume for (a) air-decane PD, (b) air-decane SD, (c) air-water PD, (d) air-water SD, (e) decane-water PD, and (f) decane-water SD. 38

Figure 2.6 (a) Relative errors of measured surface/interfacial tensions ($\Delta\gamma$) for decane, water, and decane-water systems as a function of the Bond number (Bo), using both PD and SD. 39

Figure 2.7 (a) Relative errors of measured surface/interfacial tensions ($\Delta\gamma$) for decane, water, and decane-water systems as a function of the Worthington number (Wo), using both PD and SD. 40

Figure 2.8 (a) Relative errors of measured surface/interfacial tensions ($\Delta\gamma$) for decane, water, and decane-water systems as a function of the Neumann number (Ne), using both PD and SD. 41

Figure 2.9 (a) Relative errors of measured surface/interfacial tensions ($\Delta\gamma$) for decane, water, and decane-water systems as a function of the shape parameter (Ps), using both PD and SD. 42

Figure 2.10 Theoretical calculation of the local Neumann number (Ne_z) along the normalized arc length from the drop apex to the three-phase contact line, for PD and SD of water with the volume of 3, 7, and 15 43

Figure 2.11 Theoretical calculation of the local Neumann number (Ne_z) along the normalized arc length from the drop apex to the three-phase contact line for PD and SD of decane, water, and decane-water with the volume of 3, 7, and 15 μL , respectively. 44

Figure 3.1 Diagram of the closed-loop axisymmetric drop shape analysis (ADSA) feedback control system integrated into the constrained drop surfactometer (CDS). 58

Figure 3.2 Demonstration of the closed-loop ADSA for controlling drop volume. 59

Figure 3.3 Demonstration of the closed-loop ADSA for maintaining a constant drop volume by automatically compensating evaporation. 60

Figure 3.4 Nonlinearity of surface area (a) and surface tension (b) with respect to the drop volume.....	61
Figure 3.5 Demonstration of the closed-loop ADSA for controlling surface area.	62
Figure 3.6 Demonstration of the closed-loop ADSA for controlling area variations in biophysical simulation of a natural pulmonary surfactant, Infasurf, under physiologically relevant conditions.....	63
Figure 3.7 Demonstration of the closed-loop ADSA for controlling surface pressure for in situ Langmuir-Blodgett (LB) transfer of DPPC monolayers from the droplet.....	64
Figure 4.1 Schematic of the sinusoidal waveform generator using a closed-loop axisymmetric drop shape analysis (ADSA) feedback control system integrated into the constrained drop surfactometer (CDS).	82
Figure 4.2 Demonstration of the waveform generator for oscillating the surface area (A) of a water droplet following the theoretical sinusoidal curve(Area offset $A_0=0.2 \text{ cm}^2$, Amplitude $A=0.02 \text{ cm}^2$, Period $\tau=10\text{s}$).	83
Figure 4.3 Relative errors ($\varepsilon = \frac{A_{measured} - A_{theoretical}}{A_{theoretical}}$) of area offset (εA_0), relative errors of amplitude (εA), relative errors of period ($\varepsilon \tau$) and R^2 as a function of frequency measured using the water droplet with the offset of 0.2 cm^2 and the amplitude of 0.02 cm^2	84
Figure 4.4 (a) Sinusoidal oscillations of the area of $C_{12}DMPO$ droplet with an offset of 0.2 cm^2 , an amplitude of 0.02 cm^2 , and a period of 10s.....	85
Figure 4.5 (a) Real and (b) imaginary parts of complex surface dilational modulus as a function of $C_{12}DMPO$ concentration at oscillation frequency of (●) 0.2, (▲) 0.1, (▼) 0.05, (◆) 0.025, (◄) 0.01 Hz.....	86
Figure 4.6 Adsorption isotherm of the surfactant $C_{12}DMPO$	87

Figure 4.7 (a) Adsorption isotherm and (b) dynamic modulus and viscous phase angle vs. surface pressure for BSA and β -casein solutions at concentration of 10 mg/L and frequency of 0.1 Hz.....	88
Figure 4.8 (a) Surface tension and (b) surface area as a function of time during adsorption of BSA using closed-loop ADSA to maintain the surface area at constant values.....	89
Figure 5.1 Visual model of the predicted dynamics of surfactant-coated nanobubbles in xylem.	102
Figure 5.2 Surface tension of xylem sap residue and cell contamination control residue of <i>Geijera parviflora</i> and <i>Distictis buccinatoria</i> measured with CDS as a function of surface area relative to the initial drop size.....	103
Figure 5.3 Schematic of the CDS set-up with subphase replacement.	104
Figure 5.4 Surface activity check of the subphase after subphase replacement with once, twice, and three times of the original volume.	105
Figure 5.5 (a) Surface tension, (b) surface area, and (c) drop volume vs. Time during subphase replacement for the drop of Infasurf.	106
Figure 5.6 The characteristic AFM topographic images of Infasurf films at 37 °C.	107
Figure 5.7 Schematic of the oil-water system.....	108
Figure 5.8 Validation of the influence of Chloroform on the isotherms.....	109
Figure 5.9 Isotherms of DPPC at three oil-water systems, i.e., heptane-water interface, decane-water interface, and hexadecane-water interface.	110
Figure 5.10 Film compressibility of DPPC monolayer in heptane-water interface, decane-water interface, and hexadecane-water interface.....	111

Figure 5.11 AFM topographic images of the DPPC monolayer at decane-water interface with surface pressure at 10, 20, 30, 42 mN/m..... 112

List of Abbreviations

A	surface area
ADSA	axisymmetric drop shape analysis
Bo	Bond number
BSA	bovine serum albumin
c	capillary constant
CDS	constrained drop surfactometer
CMC	critical micelle concentration
$\Delta\rho$	density difference across the interface
DMPC	dipalmitoyl phosphatidylcholine
C ₁₂ DMPO	dodecyldimethylphosphine oxide
V	drop volume
E _r	elastic modulus
g	gravitational acceleration
E ₀	limiting elasticity
Ne	Neumann number
PD	pendant drop
PB	pendant bubble
PID	proportional-integral-derivative
R ₀	radius of curvature at the drop/bubble apex

Ps	shape parameter
SB	sessile bubble
π	surface pressure
γ	surface/interfacial tension
SD	sessile drop
E	total modulus
Ei	viscous modulus
Wo	Worthington number

Chapter 1. Measurement of surface and interfacial tensions

1.1 Introduction

Being a miniaturized experimental platform for studying interfacial phenomena, droplets have been involved in a wide range of scientific and industrial applications, such as synthesis of thin-film materials,¹ control of interfacial reactions,² study of surface rheology,³ and operation of digital microfluidics.⁴ Compared to the traditional interfacial models such as the classical Langmuir trough, droplet-based platforms have several advantages.⁵ First, the small volume of droplets facilitates study of scarce or expensive samples, such as biological or clinical fluids. Second, compared to bulk systems, droplets possess a much larger surface-area-to-volume ratio which makes them an ideal soft platform for studying surface reaction and interfacial assembly. Third, due to system miniaturization, it is feasible to ensure a rigorous environmental control, such as temperature and experimental atmosphere, with the droplet system, thus allowing for environmental studies across the droplet surfaces.⁶

Surface/interfacial tension is one of the most important properties of the interfacial structures at the liquid-fluid interface. The determination of the surface tension of air-liquid surfaces and the interfacial tension of liquid-liquid interfaces plays an important role in a variety of scientific and industrial fields. Various methods have been developed to measure the surface/interfacial tension, such as the Wilhelmy plate, drop weight/volume method, drop shape analysis, and maximum bubble pressure method. Among these methods, drop shape analysis, using a droplet as an interfacial model, stands out with a number of advantages aforementioned. Along the lines of early efforts in analyzing liquid-fluid menisci,^{7, 8, 9} Neumann and coworkers have developed

the numerical algorithm of axisymmetric drop shape analysis (ADSA) for determining surface and interfacial tensions from the shape of drops or bubbles.^{10, 11, 12} To date, ADSA has been widely used in a variety of applications, such as the biophysical study of pulmonary surfactant (PS),^{6, 13} adsorption of proteins and phospholipids,^{1, 2, 14} cellular biomechanics,¹⁵ and oil recovery.¹⁶

Surface and interfacial tensions characterize the static properties of the surface. However, in a variety of situations, the system is subjected to dynamic conditions, such as the formation and stabilization of emulsions and foams. It is commonly believed that the reduction of the surface/interfacial tension places the most important effect on the emulsions and foams. Thus, one may think emulsion can be made from liquid with low interfacial tensions. However, it is impossible to generate emulsions with any degree of stability from pure liquid with low interfacial tension, in absence of any surface active materials. In such conditions, the dynamic response of the surface/interfacial tension to the change of the surface area, *i.e.*, dilational rheology, denominates the behavior of the interfacial layers.^{17, 18} The study of surface dilational rheology provides information about mechanisms of the interfacial layers affecting the evolution of the system, such as emulsions and foams. In addition to the industrial applications, the surface dilational rheology indicates a close relationship to the adsorption mechanisms, making it a unique tool to characterize the transport and kinetic processes of surfactant adsorbing on the surface.¹⁹ The surface dilational modulus is determined from the amplitudes of the surface area and surface tension oscillations, and from the phase shift between area and tension changes. A variety of methods have been developed for dilational rheology measurement, such as oscillating barrier,^{20, 21} capillary waves,²² bubble pressure,^{23, 24} and drop/bubble shape analysis.^{25, 26, 27} Among these methods, drop/bubble shape analysis owns several advantages in studying surface

dilational rheology. First, the surface/interfacial properties are calculated from the profile the drop/bubble without directly contacting the surface, thereby avoiding potential contaminations. Second, the drop/bubble can be oscillated with uniform expansion and compression, providing accurate results in characterizing the surface dilational rheology. Finally, usage of small quantities of liquid sample usage facilitates the study of scarce or expensive sample, such as biological or clinical fluids.

In the present context, the goal is to develop a methodology for studying interfacial tension and rheology based on a constrained droplet. ADSA was used to determine the properties of the drop, *i.e.*, surface/interfacial tension, surface area, and drop volume. An experimental setup called constrained drop surfactometer (CDS) was developed for measuring interfacial tension and rheology. We first evaluated the accuracy of the ADSA in measuring surface and interfacial tensions in the CDS. Taking advantage of real-time calculation, we then extended the applications of ADSA from a surface tension measurement methodology to a sophisticated tool for manipulating droplets in real-time. ADSA was developed to a closed-loop control system for manipulating millimeter-sized droplets in the CDS. Using the closed-loop ADSA, the CDS was capable of directly generating sinusoidal oscillations of surface area for surface dilational modulus measurement.

1.2 Axisymmetric drop shape analysis (ADSA)

In a gravitational field, the shape of a drop/bubble is determined by the balance between the surface tension force, which tends to keep the drop spherical to minimize the excess energy of the interface, and the gravity, which tends to deform the drop (elongate a pendant drop or flatten a sessile drop). When gravity and surface tension forces are comparable, surface tension can be calculated from analyzing shape of the drop/bubble. The shape of a drop can be determined from

the known physical parameters, when the surface tension γ is known. Inversely it is possible to determine the surface tension from a given profile of the drop shape. However, calculation of the analytical solution for surface tension from the drop profile is mathematically difficult. Thus, numerical solutions have been widely proposed and developed by researchers.⁵ Among these numerical solutions, ADSA, which was developed by Neumann and coworkers,^{10, 12, 28} is proven to be the most advanced method. Surface tension is determined by fitting the experimental drop profile to the theoretical Laplace equation in ADSA. Four drop/bubble configurations are commonly used for surface/interfacial tension measurements, *i.e.*, pendant drop (PD), sessile drop (SD), pendant bubble (PB), and sessile bubble (SB). In this section, we first propose a computational scheme for the unified drop/bubble coordinate system and then review the numerical procedure of surface/interfacial tension calculation.

1.2.1 Computational scheme for a unified drop/bubble coordinate system

ADSA determines the surface/interfacial tension by numerically fitting the experimental profile to theoretical profiles generated by integrating the Laplace equation of capillarity until the best match is found.^{10, 12} **Figure 1.1** illustrates a unified coordinate system for the four commonly used axisymmetric drop/bubble configurations, *i.e.*, PD, SD, PB, and SB. The origin of the coordinate system is universally set at the apex of the drop/bubble. Direction of the z-axis is set as the same direction of the gravitational acceleration (g). Theoretical profiles of these drop/bubble configurations are described by the Bashforth-Adams equation (Eq. 1.1), in which the tangential angle (φ), radius (x), and height (z) at any point of the drop/bubble profile are expressed as functions of the arc length (s):

$$\frac{d\varphi}{ds} + \frac{\sin \varphi}{x} = \frac{2}{R_0} + \frac{\Delta\rho g}{\gamma} z$$

$$\frac{dx}{ds} = \cos \varphi \tag{Eq. 1.1}$$

$$\begin{cases} \frac{dz}{ds} = \sin \varphi & z > 0 \\ \frac{dz}{ds} = -\sin \varphi & z < 0 \end{cases}$$

Boundary conditions for φ , x , and z are given at the apex of the drop/bubble,

$$\varphi(0) = x(0) = z(0) = 0 \tag{Eq. 1.2}$$

In Eq. 1.1, R_0 is the radius of curvature at the drop/bubble apex; g is the gravitational acceleration; γ is the surface/interfacial tension; $\Delta\rho \equiv \rho_{in} - \rho_{out}$ is defined as the density difference between the fluid inside the discrete drop/bubble and the immiscible fluid outside the drop/bubble. When $\Delta\rho > 0$, it defines a “general drop” that include both a liquid drop in air and a liquid drop in another lighter immiscible liquid. When $\Delta\rho < 0$, it defines a “general bubble” that include both an air bubble in liquid and a liquid drop in another denser immiscible liquid.

The combination of signs for $\Delta\rho$ and z uniquely defines four drop/bubble configurations in the unified coordinate system shown in Figure 1.1.

$\Delta\rho > 0$ and $z > 0$ defines a sessile drop (SD); $\Delta\rho > 0$ and $z < 0$ defines a pendant drop (PD);

$\Delta\rho < 0$ and $z > 0$ defines a pendant bubble (PB); $\Delta\rho < 0$ and $z < 0$ defines a sessile bubble (SB).

Since growth of the hydrostatic pressure along the drop/bubble profile is determined by $\Delta p = \Delta\rho g z$, with the unified coordinate system defined in Figure 1.1, it is consistent that the gravity tends to elongate a pendant drop/bubble ($\Delta\rho < 0$) but flatten a sessile drop/bubble ($\Delta\rho > 0$).

1.2.2 Numerical procedure for surface/interfacial tension calculation

The general procedure of ADSA for calculating the surface/interfacial tension from the shape of drop/bubbles is illustrated in **Figure 1.2**, using sessile drop as an example. Conceptually, three

steps are involved in the determination of surface/interfacial tensions. First, the image of a drop or bubble is acquired by a camera or other image acquisition device. The image is then analyzed and the experimental profile of the drop/bubble is extracted using edge detection technique. For noise images, an extra smoothing step should be followed to remove the outliers. Finally, a series of Laplacian curves with known surface tension values and physical properties are generated to fit to the experimental profile. The best fit gives liquid-fluid properties, *i.e.*, interfacial tension, surface area, and the drop volume. The detail description of image acquisition, image analysis, and numerical fitting will be discussed in the following sections.

Image acquisition. The image of drop/bubble is acquired using a machine vision camera. To obtain a sharp edge of the drop/bubble, a red-color parallel backlight is used to illuminate the drop/bubble. A digitized image from the machine vision camera stores the image data in the form of pixels, the value of which is called the intensity or grey level. A maximum resolution of 1280×1024 pixels is used in our laboratory with 256 grey levels to characterize an image where 0 and 255 represent black and white. Once an image of the drop/bubble is obtained, the image can either be stored in the computer for future analysis or be directly fed to ADSA for real-time analysis.

Image analysis. To extract the edge of the drop/bubble, the Canny edge detector is used. A comparison of the edge detection techniques used in ADSA can be found in a recent review.²⁹ The Canny edge detector is a gradient edge detector, which involves the derivatives of the gray levels of an image. Thus, a filter based on the first derivative of a Gaussian function is used in Canny.²⁸ Generally, the Canny algorithm consists of three steps. In the first step, the Gaussian filter is applied to the image to reducing the noise, generating a slightly blurred version of the original image. The second step is to search whether a pixel with a finite (non-zero) gradient

magnitude is a local maximum or not, reducing the edge width to only one pixel. The pixel is selected as an edge if the gradient magnitude at the pixel is larger than the gradients of its neighbors in the gradient direction. Otherwise the pixel is marked as background. In the last step, hysteresis thresholding is performed. Two user specified thresholdings are defined to get a continuous edge. In this step, any pixel with a gradient magnitude above the high threshold is selected as a valid edge pixel, while non-edge pixels are those with gradient magnitude less than the low threshold. Any pixel with a gradient magnitude above the low threshold and connected to edge pixels is also selected as an edge pixel.

It should be noted that, the coordinates of the detected experimental profile are presented in terms of pixels. The theoretical Laplacian curves are obtained in millimeters. Therefore, the value of pixels should be scaled to the millimeters. Generally, the scaling factor is known from the experimental setup and can be held constant once determined.

Numerical fitting. The numerical scheme, which was first introduced by Rotenberge et al.¹⁰ and further developed by del Rio et al.,¹² used to find the best fit between an experimental profile and the theoretical curves with known surface/interfacial values. Prior to the fitting process, the theoretical curve is generated by integrating the Laplace equation for given values of surface properties and the curvature at the apex of the drop as described in Figure 1.1. The initial value of the curvature at the apex can be estimated by a least-square elliptical fit of several points near the drop apex.¹² The normal distances (e_i) between the experimental coordinate and the corresponding closet Laplacian profile can be calculated as

$$e_i = \frac{1}{2}d_i^2 = \frac{1}{2}[(x_i - X_i)^2 + (z_i - Z_i)^2] \quad (\text{Eq. 1.3})$$

where (X_i, Z_i) are the experimental drop coordinates and (x_i, z_i) are the Laplacian coordinates which are closest to (X_i, Z_i) . The goal of the numerical fitting is to find the minimum of an

objective function E , defined as the sum of the weighted e_i for all the points (e.g., N points) along the experimental profile.

$$E = \sum_{i=1}^N w_i e_i \quad (\text{Eq. 1.4})$$

where w_i is the weighting factor indicating the contribution of i^{th} point to the fitted curve. It will be discussed in Chapter 2 that the sensitivity of the point along the profile to the surface/interfacial tension differs at different locations. A potential way to determine the w_i will also be discussed in Chapter 2. Otherwise w_i can be generally set to 1.0. The optimizing parameters were selected from the vertical alignment of the camera α , the surface tension γ , the coordinate of the apex of the drop x_0 , and z_0 , and the curvature of the apex b , denoted as $\mathbf{a}=[\alpha, \gamma, x_0, z_0, b]$. Thus, the optimization problem can be written as

$$\min E(\mathbf{a}) = \sum_{i=1}^N w_i e_i(\mathbf{a}) \quad (\text{Eq. 1.5})$$

Equation 1.5 is a multidimensional nonlinear least-square problem that requires an iterative optimization procedure. When the minimum has been found, the optimization parameters determine the Laplacian profile that best fits the given profile, from which γ and other properties can be readily computed.

Assuming a single absolute minimum value in the 5 dimensional space of E , the necessary conditions for the extremum are

$$\frac{\partial E}{\partial \mathbf{a}_k} = \sum_{i=1}^N \frac{\partial e_i}{\partial \mathbf{a}_k} = 0, \quad k = 1, 2, \dots, 5 \quad (\text{Eq. 1.6})$$

The above equations generate a set of nonlinear algebraic equations in the variables \mathbf{a}_k , $k = 1, 2, \dots, 5$. In order to get the value of these variables, an iterative solution is required. A combination of the Newton-Raphson and Levenberg-Marquardt methods are used in the optimization.¹² The

outputs of the numerical solvers are the aforementioned optimization parameters that give the best fit between the measured points and a Laplacian curve. Once the best fitting theoretical curve is found, surface tension can be determined directly from the outputs of the optimization parameters. The other properties of the drop/bubble, such as surface area (A) and the drop/bubble volume (V) can be determined using Equations 1.7-1.8.

$$\frac{dV}{ds} = \pi x^2 \sin \varphi \quad (\text{Eq. 1.7})$$

$$\frac{dA}{ds} = 2\pi x \quad (\text{Eq. 1.8})$$

1.3 Constrained drop surfactometer (CDS)

To facilitate the surface/interfacial tension measurement, an experimental setup called constrained drop surfactometer (CDS) is developed, using ADSA as the numerical procedure for determining the properties of the droplet. The CDS is made of three fundamental components: the benchtop unit, the control box, and the software for control and data analysis. The software is developed based on the aforementioned ADSA algorithm. To generate and control the drop/bubble and the subsequent image acquisition, we developed the benchtop unit and the controller box. The benchtop consists of the drop/bubble holder, the environmental control system, the image acquisition system, and the liquid flow control system. The control box is an interface to connect the hardware to the software. The schematic and a picture of the CDS are illustrated in **Figure 1.3** and **Figure 1.4**, respectively.

1.3.1 Benchtop unit

The benchtop unit consists of four components: drop/bubble holder, environmental control system, image acquisition system, and liquid flow control system.

The four drop/bubble configurations were formed on a carefully machined pedestal in the holder with a sharp edge that prevents the drop/bubble from spreading or detaching, especially at low surface/interfacial tensions. The schematic of the four configurations is illustrated in Figure 1.3. The pedestal is machined from stainless steel with the size usually set to a diameter of 3 mm, which is close to the capillary constant of pure water. The angle between the horizontal and the side surfaces of the pedestal is machined to be $\sim 60^\circ$. A central hole of 1 mm is designed for liquid transportation through the holder. When measuring the interfacial tension, a drop/bubble of the discrete liquid was contained within another immiscible liquid held in a disposable acrylic cuvette.

The environmental control system provides the drop/bubble a local environmental condition of temperature and humidity, e.g., a body temperature of 37°C with 100% humidity. It is composed of a thermoelectric plate (Model CP-061HT, TE Technology) and a homemade environmental chamber. The thermoelectric plate is controlled by a bipolar temperature controller, increasing or decreasing the temperature (range from -20°C to 100°C). Two glass windows are mounted on the walls of environmental chamber where illumination light can pass through. Temperature is monitored inside the environmental chamber by a thermistor (Model MP-3022, TE Technology).

The image acquisition system is composed of a camera (Model PLD-721MU, PixeLink), a telemetric lens (65 mm WD, 1x, Edmund), and an illumination light source (ICS 3, Advanced illumination). The camera, which is mounted on a three-dimensional manipulator, takes images with an acquiring rate between 0 and 30 frames per second (FPS) with maximum resolution of 1280×1024 pixels. A red light source is used to illuminate the experimental drop/bubble. With a

diffusing lens, parallel backlight is provided for the illumination. Thus, drop/bubble images with a high contrast liquid-fluid interface can be obtained.

The liquid flow control system is composed of a servo motor (Model LTA-HS, Newport) and a syringe (1002C, Gastight, Hamilton). It allows manipulating fluid flow of the droplet automatically, such as drop formation, removal and dynamic cycling. Hence the volume of the droplet can be precisely manipulated. The servo motor can provide a maximum displacement speed of 5 mm/s and a resolution of 0.1 μm (equivalent to a volume resolution of approximately 4 nL).

1.3.2 Controller box

The CDS controller box functions as an interface between the benchtop unit and the software. It consists of three parts: motor controller (Model SMC100-CC, Newport), temperature controller (Model TC-720 OEM, TE Technology), and backlight controller.

The motor controller is connected with the servo motor and controls the motorized syringe. The temperature controller is connected to the thermoelectric plate and controls the temperature of the environmental chamber. The backlight controller is connected with the illuminator to provide power supply. Both the motor controller and the temperature controller are programmable.

1.4 Surface and interfacial tension measurements with drops and bubbles

To demonstrate the feasibility and accuracy of the CDS in surface and interfacial tension measurement, we measured the surface tensions of six commonly used solvents and interfacial tensions of three oil-water systems.

1.4.1 Test liquids

Six commonly used solvents, which cover a broad range of surface tensions, were tested for surface and interfacial tension measurements. These were water, formamide, dimethyl sulfoxide (DMSO), 1-octanol, hexadecane, and decane. Physicochemical properties and sources of these liquids are summarized in **Table 1.1**. Both surface tension of these liquids^{30, 31, 32} and interfacial tension of three immiscible solvents with water,^{33, 34} have been well studied. Water, formamide, DMSO, 1-octanol, and decane were used without further purification. Hexadecane was purified with aluminum columns prior to experiments to remove surface active impurities.^{34, 35}

1.4.2 Results and discussion

We demonstrate the accuracy of ADSA in determining surface/interfacial tension under normal measurement conditions, *i.e.*, using well-deformed drop/bubble with large enough volumes. **Figure 1.5** shows the surface tension measurements of six commonly studied liquids, including water, formamide, DMSO, 1-octanol, hexadecane, and decane, each determined with four drop/bubble configurations, *i.e.*, PD, SD, SB, and PB. Volumes of the drop/bubble were maintained at around 15-20 μL to ensure well-deformed shapes (see Figure 1.5 for sample drop/bubble images). It is found that surface tensions determined with four configurations are consistent with each other, and have a good agreement with literature values.^{30, 31, 32}

Figure 1.6 shows the interfacial tension measurements of three oil-water interfaces, *i.e.*, hexadecane-water, decane-water, and octanol-water interfaces, each determined with four drop/bubble configurations. Volumes of the drop/bubble were maintained in the range of 50-100 μL to ensure well-deformed shapes (see Figure 1.6 for sample drop/bubble images). Again, the interfacial tensions determined with these four configurations are consistent with each other. It should be noted that interfacial tension values reported in literature show slight inconsistency, as

summarized in Figure 1.6. The inconsistency was most likely caused by the accuracy of different methods, measurement temperatures,^{33, 34} and impurities of liquids used.³⁵ It is found that our measurements are in general agreement with the literature values.^{33, 34}

1.5 Summary and scope of this dissertation

The determination of surface tension and interfacial rheology play an important role in a variety of scientific and industrial fields. Droplets, as a miniaturized experimental platform for studying surface phenomena, have a number of advantages over the traditional experimental methods. In this chapter, the numerical procedure of ADSA in determining the surface tension from the droplet was reviewed. A droplet-based experimental platform called the constrained drop surfactometer (CDS) was then developed using ADSA for determining surface tension and interfacial rheology.

The rest of the thesis is organized as the following. Chapter 2 will investigate the accuracy of ADSA in surface and interfacial tension measurement. A new dimensionless parameter, called the Neumann number, will be proposed to replace the classical Bond number for evaluating the accuracy of ADSA upon reducing drop volume. Chapter 3 will discuss the development of the closed-loop of ADSA (CL-ADSA) for droplet manipulation and its applications in surface science researches. With the CL-ADSA, the CDS is transformed from a traditional surface tension measurement methodology to a sophisticated experimental platform for manipulating millimeter-sized single droplets in real-time. Chapter 4 will demonstrate the development of a sinusoidal waveform generator to study the surface dilational rheology. For the first time, our novel methodological invention permits direct control of surface area oscillated in a sinusoidal pattern, thus resulting in a precise evaluation of the surface dilational rheological properties of complex fluids, including surfactants and proteins. Chapter 5 lists some other researches we have

done with the CDS, including determination of surface tension of xylem surfactants, development of subphase replacement technique, and study of phospholipid self-assembly at oil-water interface. Chapter 6 concludes the work finished in this thesis and the prospective future directions that has stemmed from this thesis.

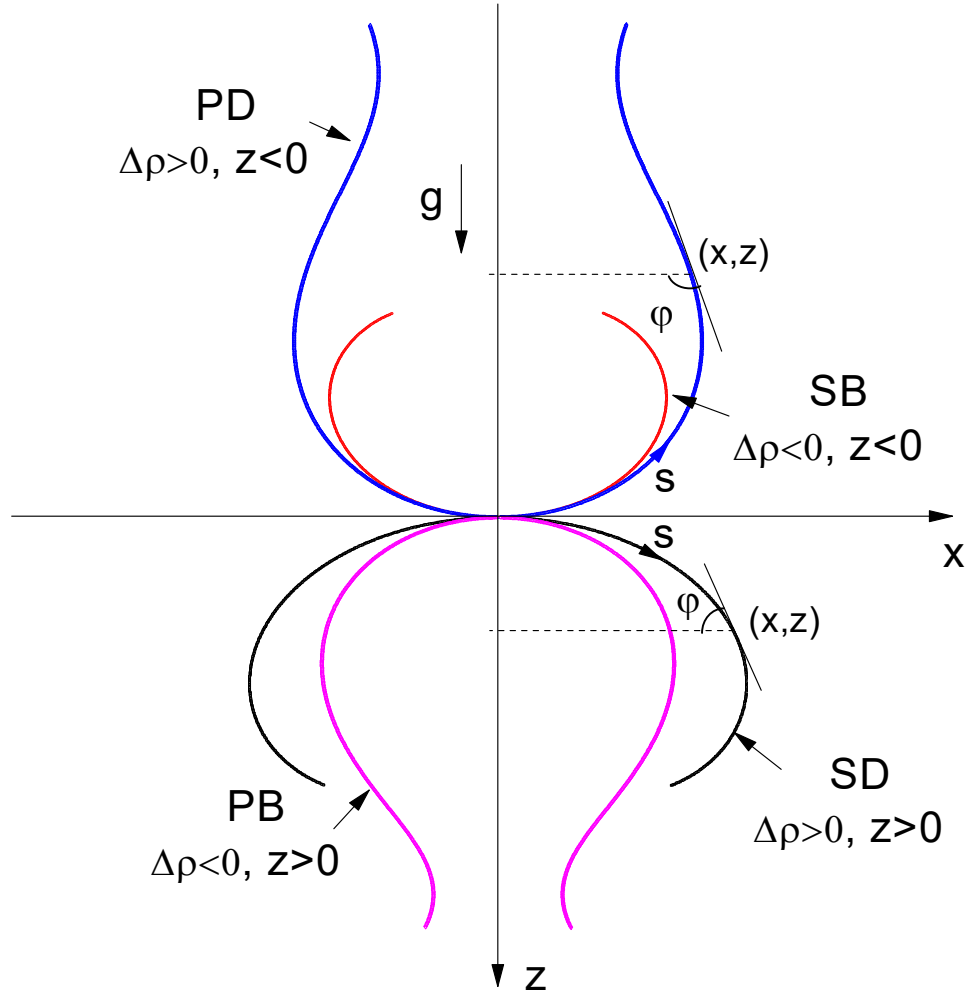


Figure 1.1 The coordinate system of numerical solution for the four commonly studied axisymmetric drop/bubble configurations: pendant drop (PD), sessile drop (SD), sessile bubble (SB) and pendant bubble (PB). The four drop/bubble configurations are differentiated by the combination of signs for $\Delta\rho$ and z . $\Delta\rho = \rho_{\text{in}} - \rho_{\text{out}}$ is the density difference between the fluid inside the discrete drop/bubble and the fluid outside the drop/bubble. $\Delta\rho$ of PD and SD is positive; while $\Delta\rho$ of SB and PB is negative. z coordinate is positive for SD and PB; while negative for SB and PD. This coordinate system is applicable to both surface tension and interfacial tension measurements.

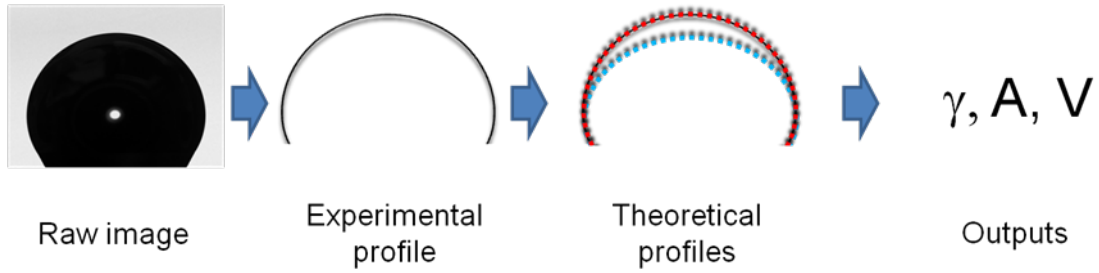


Figure 1.2 Procedure of ADSA using a sessile drop as example. Raw image acquired from camera is fed to ADSA. The edge of the drop profile is extracted using edge detection technique. A series of theoretical profiles are generated to match the experimental profile. Once the best fitting is reached, the properties of the surface, such as surface tension, surface area, and drop volume are obtained.

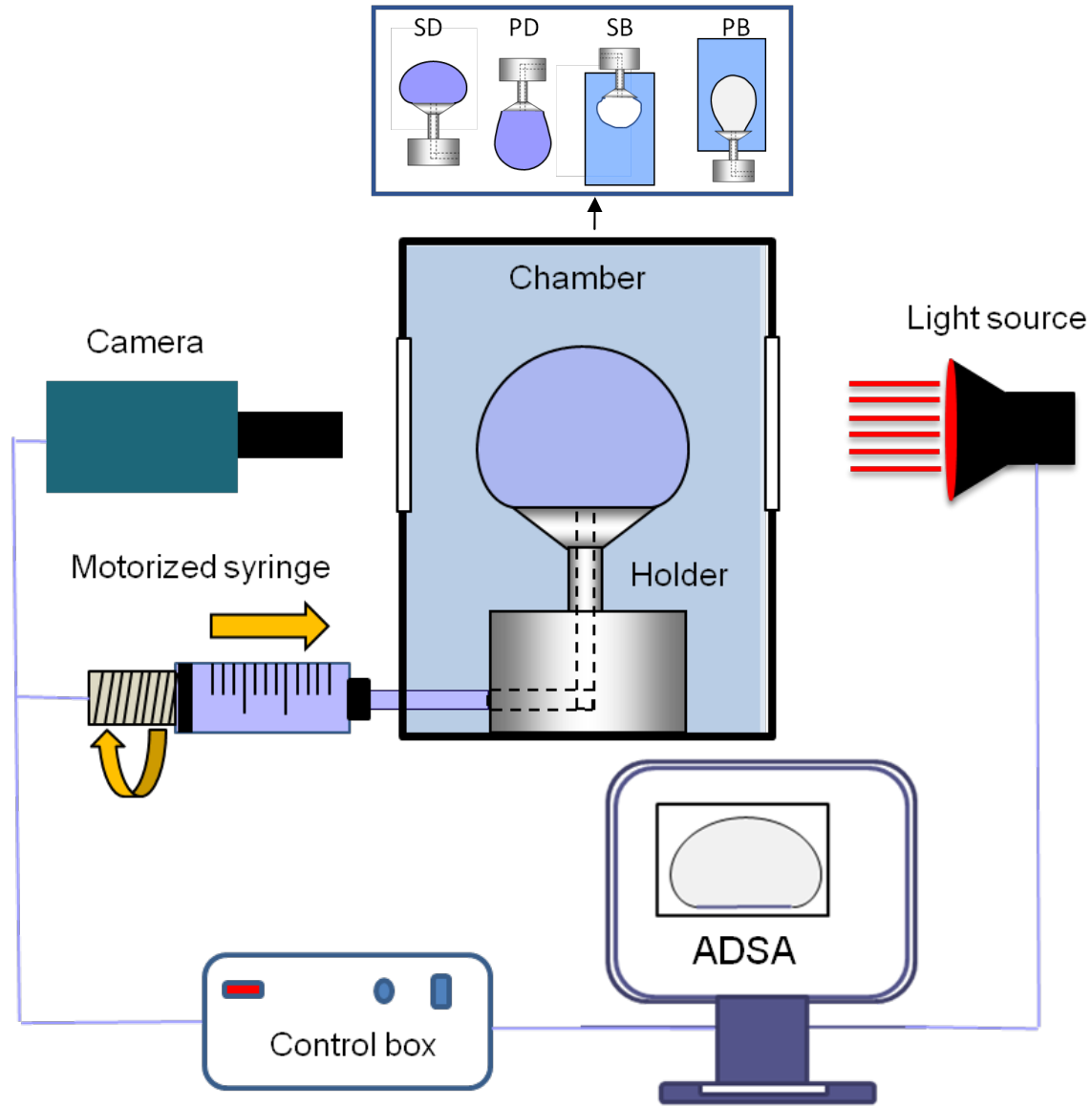


Figure 1.3 Schematic of the experimental setup. A drop is formed on a pedestal with sharp edge. The pedestal is then placed in a chamber with temperature controlled by a thermoelectric plate. Other configurations can also be achieved using the same pedestal as indicated in the figure. The pedestal is connected to a motorized syringe for droplet formation and oscillation. A light source is used to illuminate the drop and a CCD camera is used to acquire on-line the drop image, which is directly sent to the ADSA for further analysis. The motor, light source, and the thermoelectric plate is connected to the control box, which interfaces with ADSA.

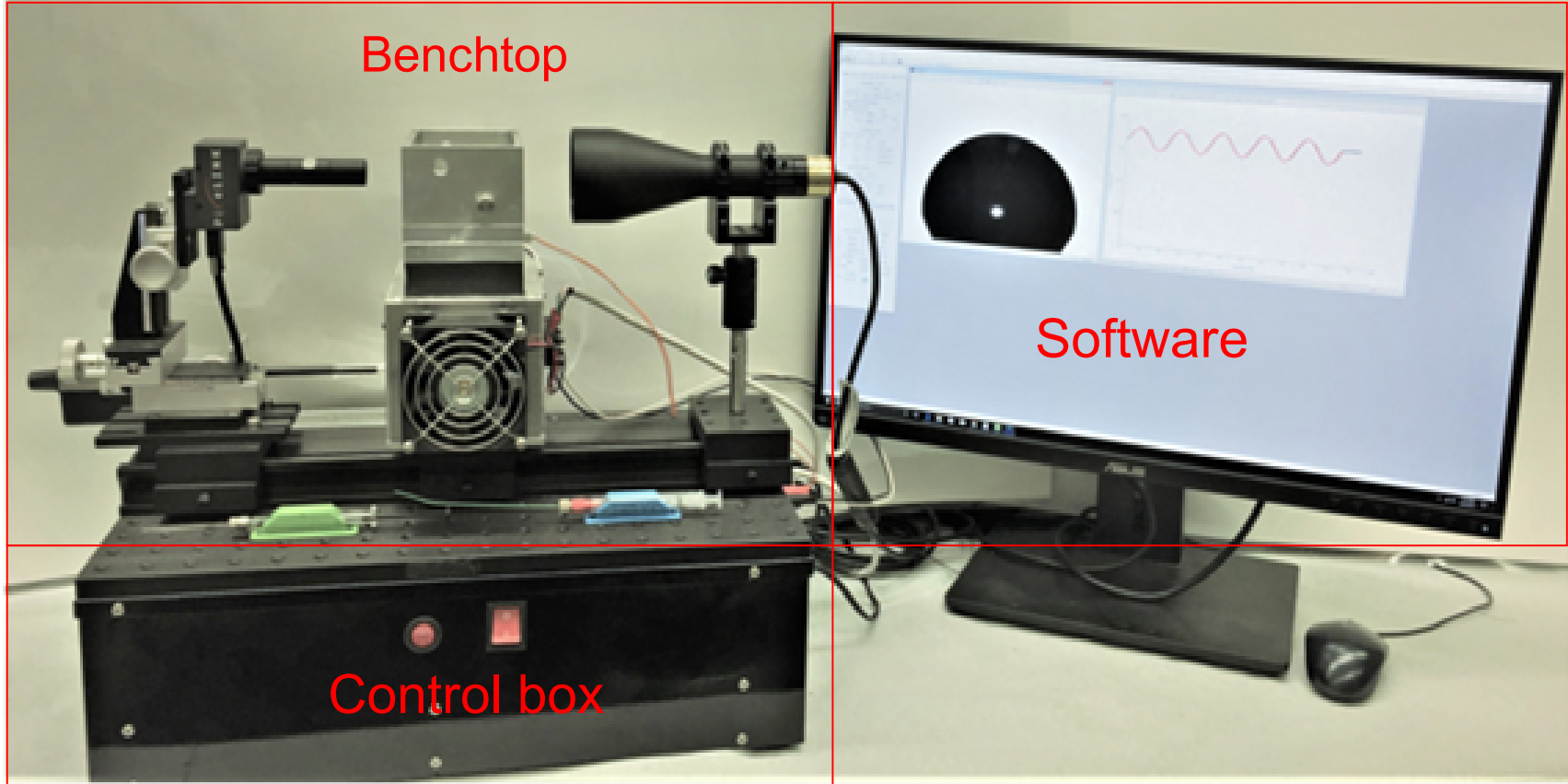


Figure 1.4 Experimental setup of the CDS. The CDS is composed of three parts: the benchtop, the control box, and the software.

Literature (mN/m)	PD	SD	SB	PB
Water				
72.88 ³⁰ 72.75 ³²	72.87±0.08	72.74±0.12	73.02±0.10	72.41±0.18
Formamide				
57.46 ³¹ 57.49 ³²	57.93±0.04	57.98±0.19	57.64±0.13	57.52±0.10
DMSO				
43.72 ³¹ 43.58 ³²	43.46±0.10	43.26±0.12	43.49±0.08	43.28±0.06
1-octanol				
27.50 ³⁰	27.29±0.10	27.43±0.06	27.35±0.07	27.39±0.03
Hexadecane				
27.47 ³⁰ 27.76 ³²	27.61±0.05	27.48±0.06	27.58±0.07	27.54±0.04
Decane				
23.83 ³⁰ 23.43 ³²	23.62±0.04	23.66±0.05	23.46±0.03	23.44±0.15

Figure 1.5 Surface tensions (in mN/m) of six test liquids, *i.e.*, water, formamide, DMSO, 1-octanol, hexadecane, and decane, each determined with four drop/bubble configurations, *i.e.*, PD, SD, SB, and PB, at room temperature (22 ± 1 °C). All measurements are shown in mean \pm standard deviation ($n=20$). Literature values are listed in the first column as a reference. It is demonstrated that surface tensions of the same liquid determined with different drop/bubble configurations are consistent with each other and are in good agreement with the literature value.

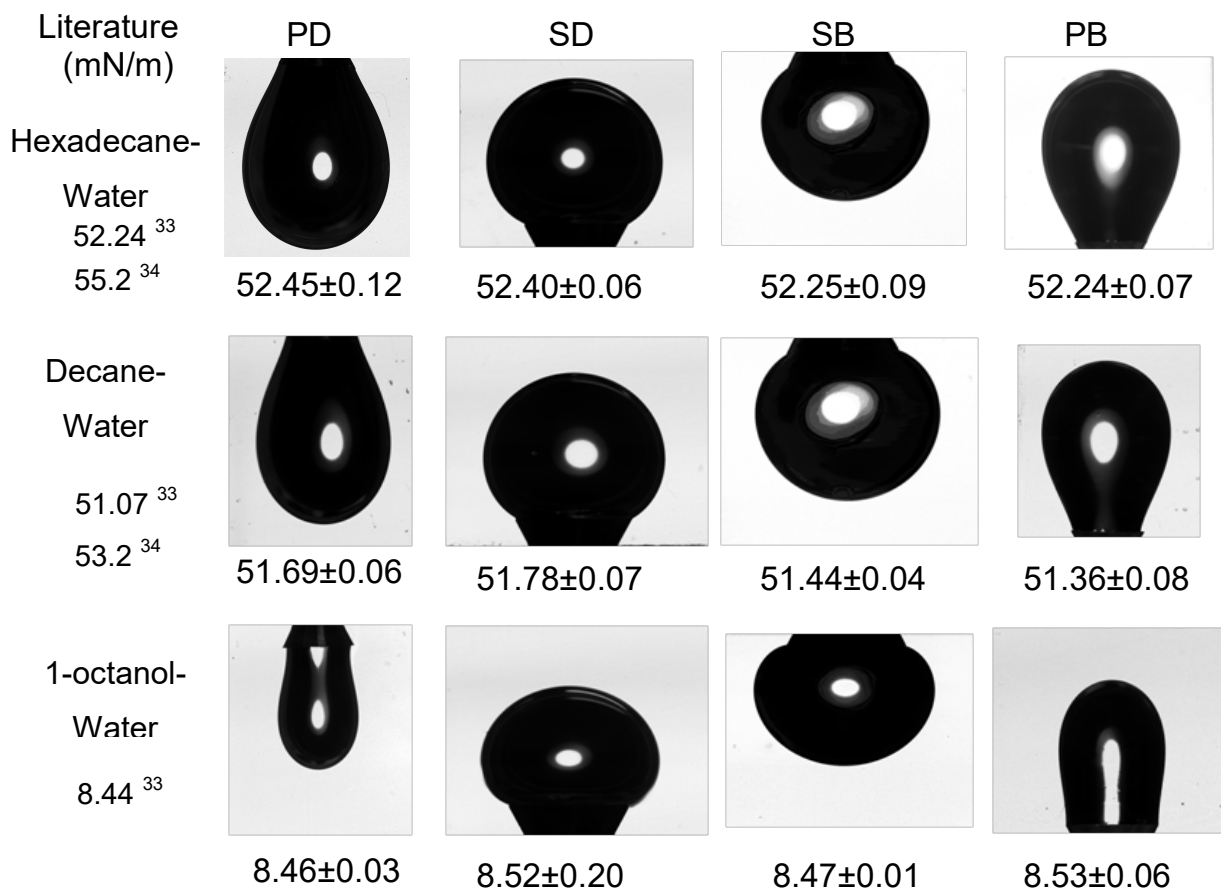


Figure 1.6 Interfacial tensions (in mN/m) of three oil-water systems, *i.e.*, hexadecane-water, decane-water, and 1-octanol-water, each determined with four drop/bubble configurations, *i.e.*, PD, SD, SB, and PB, at room temperature (22 ± 1 °C). All measurements are shown in mean \pm standard deviation ($n=20$). Literature values are listed in the first column as a reference. It is demonstrated that interfacial tensions of the same oil-water interface determined with different drop/bubble configurations are consistent with each other and in general agree with the literature value.

Table 1.1 Physicochemical properties and sources of the tested liquids.

Liquid	Chemical formula	Density (g/cm³)	Purity (%)	Miscibility with water	Supplier
Water	H ₂ O	0.997	99.9	-	Millipore
Formamide	CH ₃ NO	1.130	99.9	miscible	Fisher scientific
DMSO	(CH ₃) ₂ SO	1.096	99.9	miscible	Fisher scientific
1-octanol	C ₈ H ₁₈ O	0.824	99.0	immiscible	Alfa Aesar
Hexadecane	C ₁₆ H ₃₄	0.773	99.0	immiscible	Acros Organics
Decane	C ₁₀ H ₂₂	0.730	99.8	immiscible	Fisher scientific

Chapter 2. Accuracy of axisymmetric drop shape analysis

2.1 Introduction

Although ADSA has been extensively used in a variety of applications, it is well known that ADSA only applies to well-deformed drop/bubble.^{29, 36, 37} Similar to any other drop shape analysis methods, the accuracy of ADSA deteriorates for non-deformed nearly-spherical drop/bubble.^{38, 39, 40} Traditionally, drop deformation is quantified by the Bond number

$Bo = \frac{\Delta\rho g L^2}{\gamma}$,^{41, 42} in which $\Delta\rho$ is the density difference across the surface/interface, g is the

gravitational acceleration, γ is the surface/interfacial tension, and L is a characteristic length that represents the size of the drop/bubble. When grouping the physicochemical properties of the surface/interface into a parameter with a length scale called the capillary constant $c = \sqrt{\frac{\gamma}{\Delta\rho g}}$,

the Bond number can be rewritten as $Bo = \left(\frac{L}{c}\right)^2$. The radius of curvature at the drop/bubble apex

(R_0) is commonly used as the characteristic length. Hence, the Bond number is generally defined

as $Bo = \frac{\Delta\rho g R_0^2}{\gamma} = \left(\frac{R_0}{c}\right)^2$. With this well-accepted definition, a low Bo much less than unity

indicates a non-deformed nearly-spherical drop/bubble at which the capillary forces significantly overweigh the gravity. Alternatively speaking, a low Bo means that the size of the drop/bubble is much smaller than the intrinsic capillary constant of the surface/interface. Therefore, the Bo has

been commonly used as a criterion for determining the accuracy of ADSA and other drop shape analysis methods.^{40, 43}

Despite its wide use, the Bo under certain circumstance fails to predict the accuracy of drop shape analysis.^{38, 39, 40} Although multiple variables collectively determine the accuracy of drop shape analysis, it is well accepted that a small drop volume is usually the primary source of errors in many practical applications. To quantify the effect of drop volume on the measurement accuracy, Berry et al. defined a new dimensionless group called the Worthington number

$Wo = \frac{V}{V_{\max}}$, primarily used for analyzing pendant drops.⁴⁰ In this definition, V is the actual drop

volume, and V_{\max} is the theoretical maximum volume for a pendant drop suspended below a

capillary tube with the diameter D_t , *i.e.*, $V_{\max} = \frac{\pi D_t \gamma}{\Delta \rho g}$. Hence, the Wo can be written as

$Wo = \frac{\Delta \rho g V}{\gamma \pi D_t}$, which is equivalent to the Bo by using $L = \sqrt{\frac{V}{\pi D_t}}$ as the characteristic length.

Hence, the Wo is intrinsically a variation of the classical Bo. However, by redefining the characteristic length directly related to the drop volume, it was found that the Wo is more reliable than the Bo in predicting the accuracy of pendant drop analysis.⁴⁰

Although being plausible for quantifying drop deformation, both Bo and Wo have limitations since the measured surface/interfacial tension (γ) is needed to evaluate both parameters. For non-deformed nearly-spherical drop/bubble, the γ value calculated from drop shape analysis can be significantly deviated from the true value and consequently introduces errors to the evaluation of these dimensionless parameters. To overcome this limitation, Neumann and coworkers proposed a purely geometrical parameter called the shape parameter (Ps) to predict the accuracy of ADSA calculation.^{38, 39, 44} The Ps measures how much the geometrical shape of a drop/bubble is

deviated from a perfect sphere. The larger the deviation, the more the drop/bubble is deformed and hence the ADSA calculation is expected to be more accurate. Since the Ps is defined purely based on geometrical comparisons, the evaluation of Ps does not require knowledge about physiochemical properties of the surface/interface, *i.e.*, independent from the capillary constant(c). Therefore, the Ps is capable of predicting the accuracy of ADSA calculation *prior to* measuring the surface/interfacial tension.

The Ps was first evaluated by calculating the sum of normal distances between the drop/bubble profile and a reference circle with the radius of R_0 .³⁸ The reference was later improved by the best-fit circle to all points along the drop/bubble profile.³⁹ In the latest development, it was found that the shape of a drop/bubble can be evaluated by a purely geometrical parameter called the total Gaussian curvature $\kappa = 2\pi(1 - \cos \theta)$, where θ is the contact angle of the drop/bubble.⁴⁴ The detail derivation of the κ is as follows.

For a Laplacian curve (*i.e.*, PD, SD, PB, and SB), the Gaussian curvature (K) can be calculated from the two principal radii (R_1 and R_2),⁴⁵ denoted by $K = \left(\frac{1}{R_1}\right)\left(\frac{1}{R_2}\right)$. For the axisymmetric interfaces, R_1 and R_2 can be calculated from tangential angle (φ), radius (x), and height (z) in the coordinate system as defined in Figure 1.1, denoted by $\frac{1}{R_1} = \frac{d\varphi}{ds}$ and

$\frac{1}{R_2} = \frac{\sin \varphi}{x}$. The total Gaussian curvature (κ) can be calculated $\kappa = \int_A K dA$ by integrating K

from the surface area, which can be calculated from s and x as $\frac{dA}{ds} = 2\pi x$. Thus κ can be

calculated by $\kappa = \int_A \left(\frac{1}{R_1}\right)\left(\frac{1}{R_2}\right) dA = \int_0^\theta 2\pi \sin \varphi d\varphi = 2\pi(1 - \cos \theta)$, where θ is the contact angle of

the drop/bubble. When the drop/bubble is formed from the pedestal, θ is the apparent contact

angle. In microgravity, both the pendant and sessile drop/bubble become spherical caps (SC). The total Gaussian curvature can still be calculated by $\kappa_s = 2\pi(1 - \cos\theta_s)$, where θ_s is the apparent contact angle of SC which can be numerically calculated from the volume and the diameter of the pedestal. The shape parameter is defined as the difference between κ of the drop/bubble and κ_s of the reference spherical cap $Ps = |\kappa - \kappa_s| = 2\pi|\cos\theta - \cos\theta_s|$. The Ps has been successfully used to predict the accuracy of ADSA for both pendant drop and sessile drop.⁴⁴

In this chapter, we systematically compared the different criteria/parameters in evaluating the accuracy of ADSA upon reducing drop volume. Taking advantage of a newly developed versatile experimental apparatus CDS, we studied the accuracy of PD and SD in determining both surface tension and interfacial tension for a large range of the drop volume. By scrutinizing the dependence of ADSA accuracy on various parameters, including the capillary constant (c), the Bond number (Bo), the Worthington number (Wo), and the shape parameter (Ps), we concluded that the classical Bond number failed to predict the accuracy of drop shape analysis at very low drop volumes. We proposed a replacement of the classical Bond number, called the Neumann number (Ne), which takes account of the effect of the drop height. It was found that being a simple variation of the classical Bond number, the Neumann number is capable of evaluating the accuracy of drop shape analysis.

2.2 Materials and methods

2.2.1 Materials

Water and decane were used for surface and interfacial tension measurements. The water used was Milli-Q ultrapure water (Millipore, Billerica, MA) with a resistivity greater than 18 M Ω ·cm

at room temperature. The decane was purchased from Fisher scientific and used without further purification.

2.2.2 Experimental methods

The PD and SD configurations were studied with the CDS which has been described in Chapter 1. In CDS, the drop was formed on a carefully machined pedestal with a sharp edge that prevents the drop from spreading or detaching, especially at low surface/interfacial tensions. The size of the pedestal was set at 3 mm in diameter, which is close to the capillary constant of pure water. When measuring the interfacial tension, a drop/bubble of the discrete liquid was contained within another immiscible liquid held in a disposable acrylic cuvette.

The volume of the drop/bubble was carefully controlled using closed-loop ADSA (CL-ADSA) as described in chapter 3. To determine the accuracy of various configurations, the drop volume was gradually decreased until the measured surface/interfacial tension value deviates from the true value by at least 1%. All measurements were carried out at room temperature (22 ± 1 °C). Each measurement was conducted for a minimum of 3 times. Results are shown in mean \pm standard deviation.

2.3 Results and discussion

2.3.1 Accuracy of ADSA evaluated by the capillary constant

We first investigated the deterioration of accuracy upon reducing the drop/bubble volume. The accuracy was quantified by the relative error between the measured surface/interfacial tension and the true value determined with well-defined drops/bubbles (as shown in Figures 1.5-1.6), *i.e.*, $\Delta\gamma = (\gamma_{\text{measured}} - \gamma_{\text{true}}) / \gamma_{\text{true}}$. We focused on three representative surface/interfacial systems, *i.e.*, the air-decane surface, the air-water surface, and the decane-water interface. Capillary

constants (c) of these three representative systems are 1.8, 2.8, and 4.5 mm, respectively. For each of the three systems, we studied the accuracy of two drop configurations, *i.e.*, PD and SD. These results are expected to be also applicable to the bubble configurations since the PB and SB can be considered as geometrical inversion of the corresponding drop configurations. Representative experimental results for air-decane, air-water, and decane-water systems can be found in **Figures 2.1-2.3**

Figure 2.4 summarizes the results of $\Delta\gamma$ for decane, water, and decane-water surface/interfacial tension measurements upon reducing the drop volume, using both PD and SD. (Reproducibility of these results can be found in **Figures 2.5**). It is clear that the measured surface/interfacial tension with both PD and SD configurations are consistent and accurate ($\Delta\gamma < 1\%$) with a sufficiently large drop volume. However, the results become inaccurate when the drop volume is smaller than a critical value at which $\Delta\gamma > 1\%$. As shown in the inset, the critical volume (V_{crit}) for both PD and SD increases with increasing the capillary constant of the surface/interface. For example, the air-water surface has a capillary constant of 2.8 mm, which requires a drop volume of at least 7.04 μL for the PD or 7.58 μL for the SD to ensure an accurate surface tension measurement ($\Delta\gamma < 1\%$). Although the differences in V_{crit} for PD and SD are only moderate for surface/interface of the small capillary constant, the differences increase with increasing the capillary constant. For the decane-water interface whose capillary constant is 4.5 mm, the V_{crit} for PD and SD become 17.58 and 18.98 μL , respectively. In general, these results indicate that the PD method has a larger volume range of applicability than the SD method, especially for the measurement of interfacial tensions.

2.3.2 Accuracy of ADSA evaluated by the Bond number (Bo)

Figure 2.6a shows the results of $\Delta\gamma$ against the Bo, for decane, water, and decane-water surface/interfacial tension measurements using both PD and SD. It is found that except for the decane-water measurements, $\Delta\gamma$ randomly scatters in the entire range of the Bo obtained in experiments (from 0.1 to 1.6). No clear relations between the Bo and the accuracy of surface/interfacial tensions ($\Delta\gamma$) can be found, which indicates that the Bo fails to predict the accuracy of ADSA as a general criterion for PD and SD.

To explain the failure of the Bo in predicting ADSA accuracy, **Figure 2.6b** shows the dependence of the Bo on the drop volume. It is clear that the Bo is not a monotonic function of the drop volume for surface tension measurements. The Bo only decreases with decreasing drop volume when the droplet is sufficiently large. However, for very small droplets, *i.e.*, when the drop volume is close to the V_{crit} shown in the inset of Figure 2.6, further reducing the drop volume increases the Bo. The non-monotonic relation between the Bo and the drop volume is due to the characteristic length scale used in defining the classical Bo number, *i.e.*, R_0 . Inset in Figure 2.6b shows that the point inflexion in R_0 (*i.e.*, the point inflexion in the Bo) is associated with the transition of contact angle (θ) across 90° . Consequently, the same Bo represents two drop volumes, a larger volume with $\theta > 90^\circ$ and a smaller volume with $\theta < 90^\circ$. It is also found that the non-monotonic nature of the Bo is only predominant for the surface tension measurement rather than the interfacial tension measurement. Hence, although the Bo fails to predict the accuracy of ADSA in determining surface tensions, it is still a valid criterion for evaluating interfacial tension measurements.

2.3.3 Accuracy of ADSA evaluated by the Worthington number (Wo)

Figure 2.7a shows the results of $\Delta\gamma$ against the Wo, for decane, water, and decane-water surface/interfacial measurements using both PD and SD. It appears that different from the

random dependence of $\Delta\gamma$ on the Bo as shown in Figure 2.6a, the accuracy of surface/interfacial tension measurements only deteriorates ($\Delta\gamma > 1\%$) for low Wo. The lower the Wo, the worse is the accuracy of ADSA. The critical Wo (Wo_{crit}) for decane, water, and decane-water systems was found to be 0.13, 0.10, and 0.10 for the PD, and 0.14, 0.11, and 0.10 for the SD (shown in the inset). In spite of the range of the capillary constant varying from 1.8 to 4.5 mm, the change of the Wo_{crit} is very limited, only between 0.14 and 0.10.

Figure 2.7b shows the dependence of the Wo on the drop volume. It can be seen that the Wo and the drop volume are linearly correlated. Slope of the linear curve is reversely correlated with the capillary constant. For the same surface/interface (*i.e.*, a certain capillary constant), the slopes for PD and SD are identical. These relations can be easily explained by the definition of the Wo.

Slope of the Wo vs. V curve is calculated as $\frac{1}{V_{max}} = \frac{\Delta\rho g}{\pi D_c \gamma} = \frac{1}{\pi D_c c^2}$, which is only a function of the capillary constant and the size of the capillary tube. In our experiments with the CDS, we used a 3-mm drop pedestal to replace the capillary tube. Hence, the definition of the Wo ensures that the Wo linearly correlated with the drop volume, and the slope of the linear curve only depends on the capillary constant of the system rather than the specific drop configuration used in measurements (see inset in Figure 2.7b).

2.3.4 Accuracy of ADSA evaluated by the Neumann number (Ne)

To investigate the validity of the Bo in evaluating the accuracy of drop shape analysis, we non-dimensionalized Eq. 1.1 as follows,

$$\frac{d\varphi}{ds} + \frac{\sin\varphi}{dx} = 2 + \frac{\Delta\rho g}{\gamma} zR_0 \quad (\text{Eq. 2.1})$$

Eq. 2.1 indicates that the shape of a drop/bubble is ultimately controlled by the dimensionless group on the right-hand side of the equation. We therefore define this dimensionless group to be

a new parameter called the Neumann number ¹ $Ne \equiv \frac{\Delta\rho g}{\gamma} R_0 H = \frac{R_0 H}{c^2}$, where H is the height of

the drop/bubble. The Neumann number (Ne) can be considered as a modified Bond number

$Bo = \left(\frac{L}{c}\right)^2$ in which the characteristic length of the drop/bubble is defined as $L = \sqrt{R_0 H}$, which

is the geometric mean of the radius of curvature at the drop apex (R_0) and the drop height (H).

Table 2.1 summarizes the different variations of the Bond number. It is clear that

$Ne = Bo \frac{H}{R_0}$. Hence, the Ne is different from the classical Bo mainly by considering the drop

height. The effect of the drop height on the accuracy of drop shape analysis was largely ignored

in previous studies. However, it has long known that surface/interfacial tension of a SD or SB is

the function of the ratio between drop diameter and drop height.^{46, 47} Recent experimental studies

by Neumann and coworkers concluded that in comparison with other factors, such as the drop

volume and the size of the capillary tube, the drop height plays a predominant role in affecting

the accuracy of ADSA.⁴⁸ The larger the drop height, the lower is the surface tension error.

Therefore, both theoretical analysis of the Laplace equation of capillarity and the experimental

evidence support the rational design of the new Neumann number.

Figure 2.8a shows the results of $\Delta\gamma$ against the Ne, for decane, water, and decane-water surface/interfacial tension measurements using both PD and SD. It can be seen that different

from the classical Bo, the Ne is capable of predicting the accuracy of ADSA for both PD and SD.

The smaller the Ne, the larger is the $\Delta\gamma$. In general, a Ne larger than 0.5 is required for accurate

¹ In honor of A. Wilhelm Neumann for his contribution to drop shape analysis.

surface tension measurements with both PD and SD. As shown in the inset of Figure 2.8a, the critical Ne (Ne_{crit}) decreases with increasing the capillary constant. For the same capillary constant, the Ne_{crit} for PD is always slightly lower than that of the SD, indicating that the PD method has a larger volume range of applicability than the SD. This conclusion drawn from the Ne is consistent with the prediction by the capillary constant as shown in Figure 2.4.

Figure 2.8b shows the dependence of the Ne on the drop volume. It is clear that different from the classical Bo , the Ne is a monotonic function of the drop volume. With decreasing the drop volume, the Ne decreases near-linearly. As shown in the inset, similar to the Wo , the slope of the linear curve decreases with increasing the capillary constant. However, different from the Wo , curves at the same capillary constant for PD and SD do not overlap with each; but with a slightly higher slope for the SD than the PD, indicating that the SD has a faster decay of drop deformation than the PD upon reducing volume.

2.3.5 Accuracy of ADSA evaluated by the shape parameter (Ps)

Figure 2.9a shows the results of $\Delta\gamma$ against the Ps , for decane, water, and decane-water surface/interfacial measurements using both PD and SD. Similar to the Wo and Ne , the accuracy of surface/interfacial tension measurements only deteriorates ($\Delta\gamma > 1\%$) for low Ps . The lower the Ps , the worse is the accuracy of ADSA. As shown in the inset, the critical Ps (Ps_{crit}) for decane, water, and decane-water systems with both PD and SD is identical and is equal to 0.31. This result is not unexpected because the Ps considers only the geometrical information of the drop/bubble but ignore its physicochemical properties, *i.e.*, irrelevant to the capillary constant.

Figure 2.9b shows the dependence of the Ps on the drop volume. Similar to the Wo and Ne , the slope of the Ps vs. V curve decreases with increasing the capillary constant. For the same capillary constant, the slope for PD is increasingly larger than SD with increasing drop volume.

This is particularly obvious for the decane-water interfacial tension measurement. It means that to achieve the same level of drop deformation, a SD needs a larger volume than the PD. Hence, the PD is more favorable than the SD for measuring interfacial tensions. However, at very low drop volumes when $Ps < 0.31$, both PD and SD become inaccurate.

2.3.6 Implications of the local Neumann number (Ne_z)

We have demonstrated the usefulness of the Neumann number (Ne) in determining the accuracy of the drop shape analysis (Figure 2.8). Here we show that the Neumann number can be used as a localized parameter to measure the contribution of points along the drop profile to the overall accuracy of the drop shape analysis. As a counterpart of the global Neumann number, we

define a local Neumann number $Ne_z \equiv \frac{\Delta\rho g R_0}{\gamma} z$, where z is the height of any point along the

drop profile (see Figure 1.1).

Figure 2.10 shows the theoretical calculation of the Ne_z along the normalized arc length(s) from the drop apex ($s=0.0$) to the three-phase contact line ($s=1.0$) for PD and SD of water with the volume of 3, 7, and 15 μL , respectively. (Similar theoretical analyses for the air-decane surface and the decane-water interface can be found in **Figure 2.11**) It can be seen that the Ne_z value increases from 0 to the maximum along the drop profile. This indicates that the drop profile close to the apex is insensitive to the change of surface tension. However, the drop profile close to the three-phase contact line contributes the most to the change of surface tensions. It is also found that although the Ne_z curves for PD and SD overlap for points close to the drop apex, the SD curve increases quicker than the PD curve when approaching the three-phase contact line, thus indicating that the accuracy of the SD is more dependent on the points close to the three-

phase contact line than the PD. This theoretical analysis is consistent with the general experimental observation that the SD method is trickier than the PD method to achieve the same accuracy.

2.4 Summary

In this chapter, we studied different criteria/parameters in evaluating the accuracy of drop shape analysis upon drop volume reduction. By scrutinizing the dependence of ADSA accuracy on the Bo, Wo, and Ps, for three representative systems with various capillary constants, we concluded that the classical Bo failed to predict the accuracy of drop shape analysis at very low drop volumes. Consequently, we proposed a replacement of the classical Bond number, called the Neumann number $Ne \equiv \Delta\rho g R_0 H / \gamma$. The design rationale of this new dimensionless number lies in the use of the geometric mean of the radius of curvature at the drop apex (R_0) and the drop height (H) as the new characteristic length to represent the drop size, *i.e.*, $L = \sqrt{R_0 H}$. It is found that the Neumann number is capable of evaluating the accuracy of drop shape analysis. We have also demonstrated the usefulness of the local Neumann number, $Ne_z \equiv \Delta\rho g R_0 z / \gamma$, in evaluating the contribution of the local drop profile to the surface tension measurement.

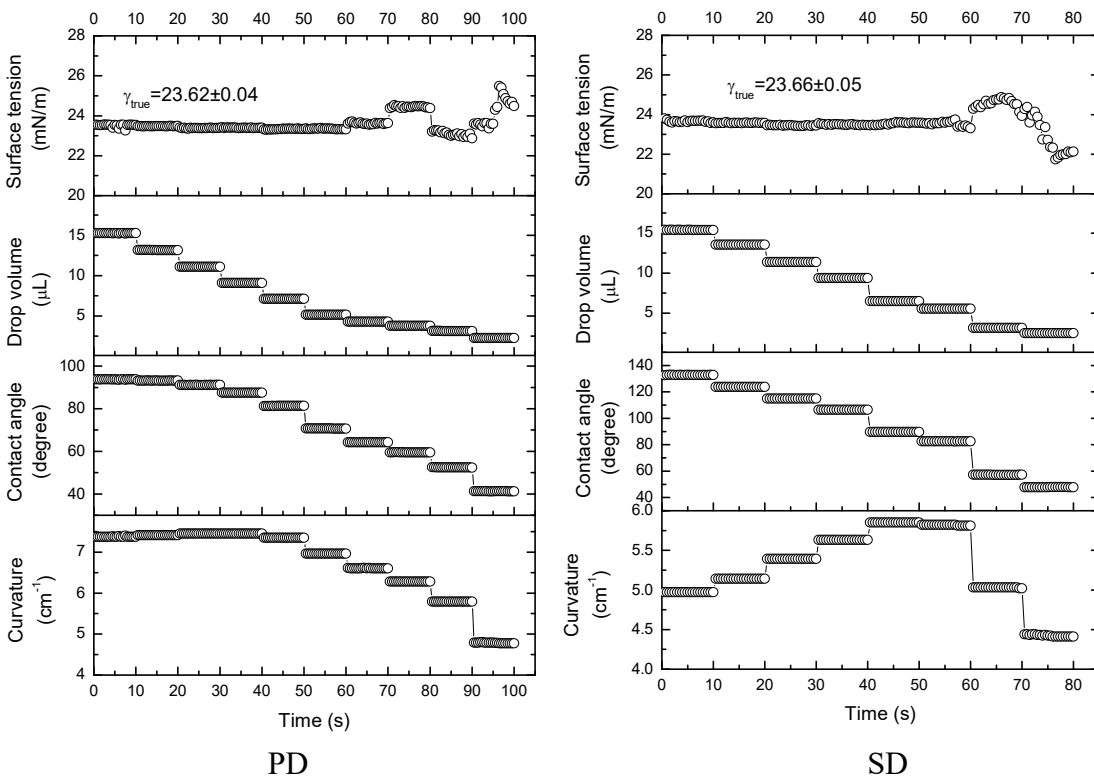


Figure 2.1 Example results of Surface tension-Drop volume-Contact angle-Curvature vs. Time for a sequence of static experiments conducted for a pendant drop (PD) and sessile drop (SD) of decane. A large drop of the liquid ($\sim 15 \mu\text{L}$) was formed on a 3-mm pedestal connected to a motorized syringe. The drop volume was then decreased slowly in steps of $2 \mu\text{L}$ until the volume that led to a large deviation in the measured surface tension was reached. During each interval, 20 images were acquired and saved for further analysis.

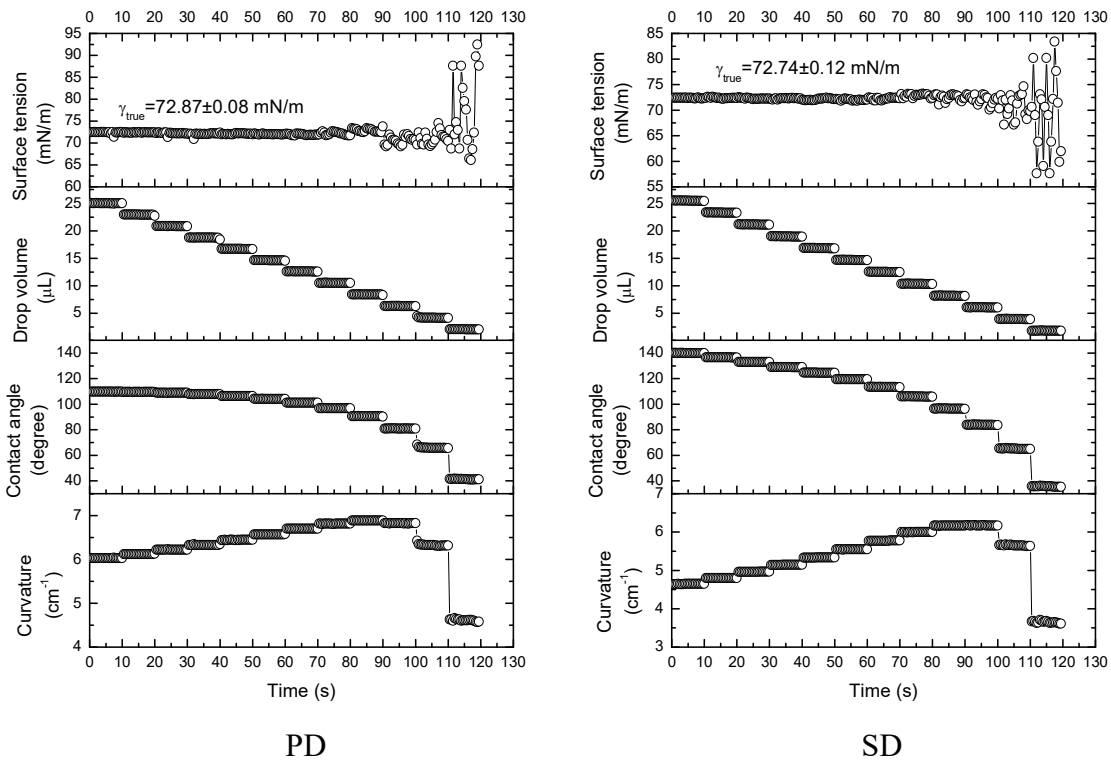


Figure 2.2 Example results of Surface tension-Drop volume-Contact angle-Curvature vs. Time for a sequence of static experiments conducted for a pendant drop (PD) and sessile drop (SD) of water. A large drop of the liquid ($\sim 25\mu\text{L}$) was formed on a 3-mm pedestal connected to a motorized syringe. The drop volume was then decreased slowly in steps of $2\mu\text{L}$ until the volume that led to a large deviation in the measured surface tension was reached. During each interval, 20 images were acquired and saved for further analysis.

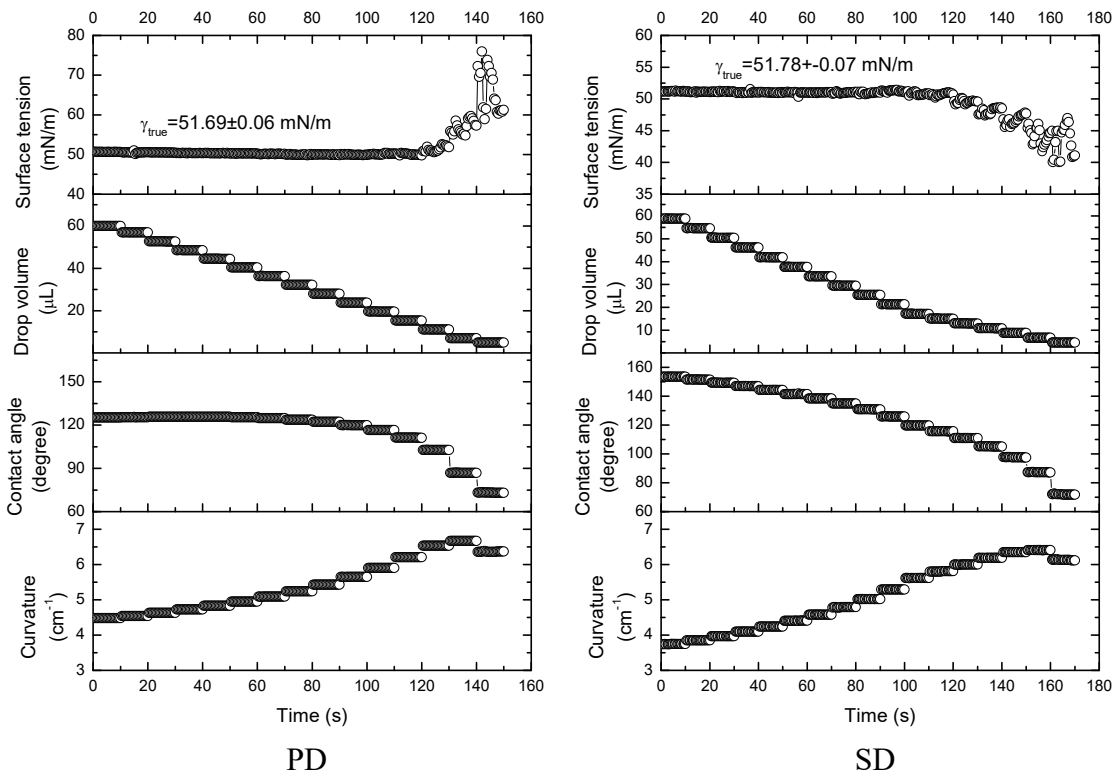


Figure 2.3 Example results of Surface tension-Drop volume-Contact angle-Curvature vs. Time for a sequence of static experiments conducted for a pendant drop (PD) and sessile drop (SD) of decane-water interface. A large drop of the liquid ($\sim 60\mu\text{L}$) was formed on a 3 mm pedestal connected to a motorized syringe. The drop volume was then decreased slowly in steps of $4\mu\text{L}$ until the volume that led to a large deviation in the measured surface tension was reached. During each interval, 20 images were acquired and saved for further analysis.

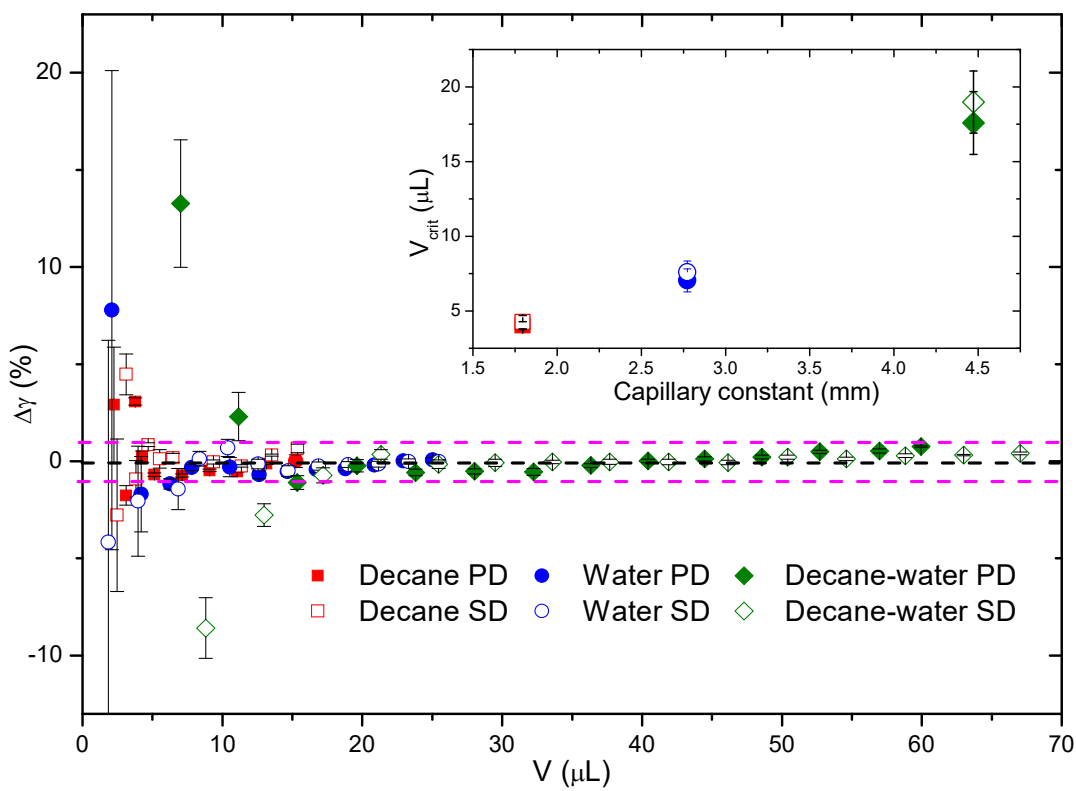


Figure 2.4 Relative errors of measured surface/interfacial tensions ($\Delta\gamma$) for decane, water, and decane-water systems upon reducing drop volume, using both PD and SD. The measurements become inaccurate ($\Delta\gamma > 1\%$) when the drop volume is smaller than a critical value (V_{crit}). Inset shows the V_{crit} for both PD and SD as a function of the capillary constant of the surface/interface.

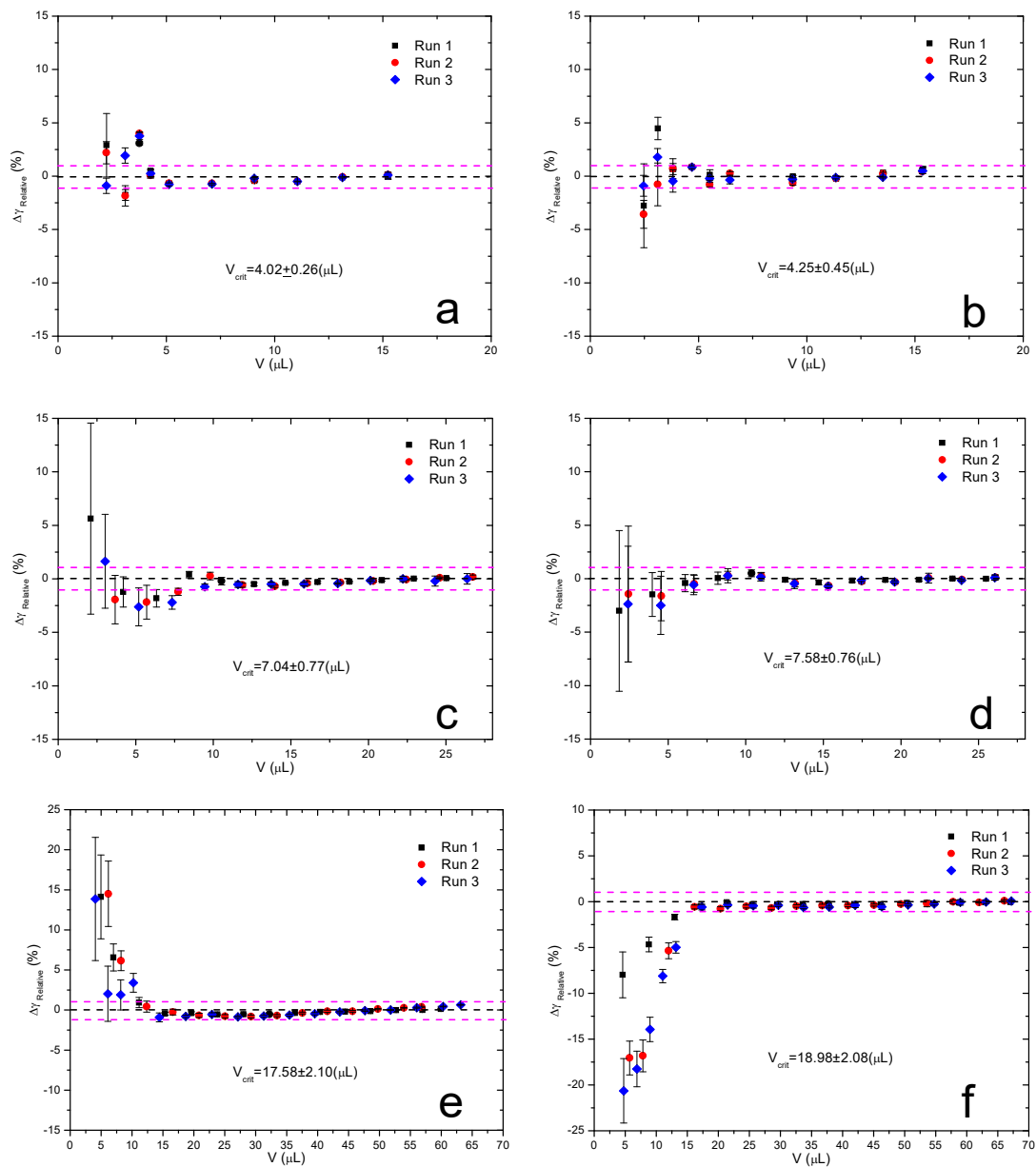


Figure 2.5 Reproducibility of experiments of the relative errors in measured surface/interfacial tensions ($\Delta\gamma$) upon reducing drop volume for (a) air-decane PD, (b) air-decane SD, (c) air-water PD, (d) air-water SD, (e) decane-water PD, and (f) decane-water SD.

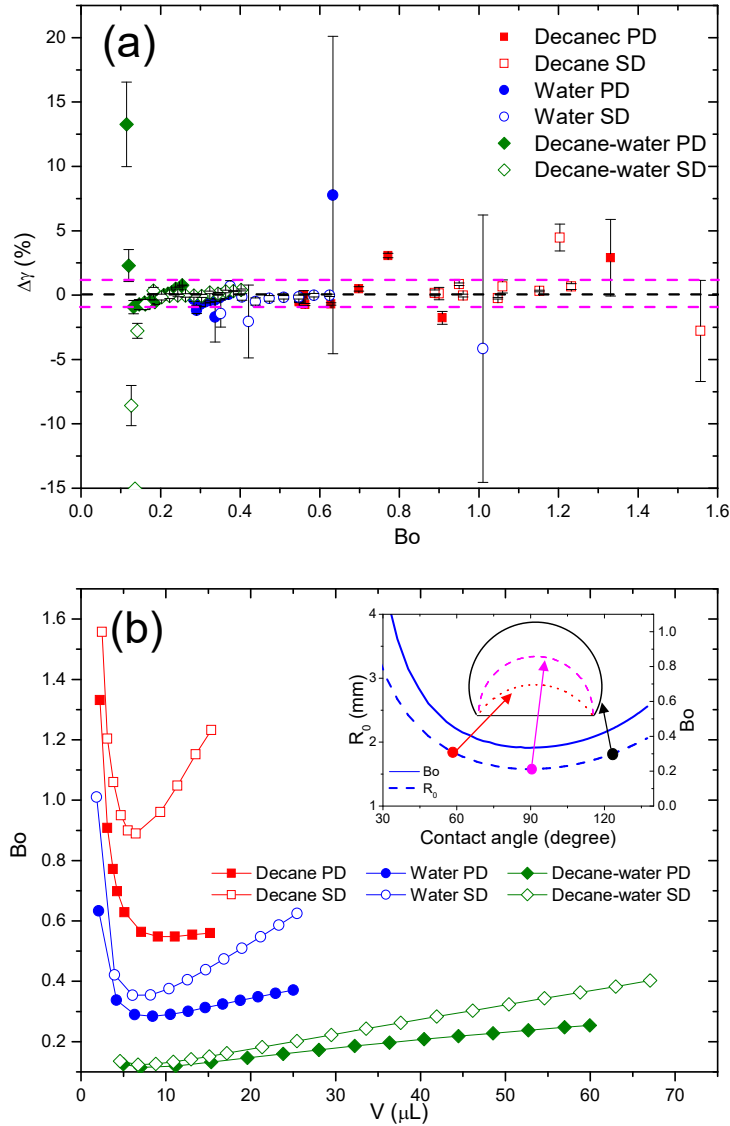


Figure 2.6 (a) Relative errors of measured surface/interfacial tensions ($\Delta\gamma$) for decane, water, and decane-water systems as a function of the Bond number (Bo), using both PD and SD. It is found that $\Delta\gamma$ randomly scatters in the entire range of the Bo obtained in experiments (from 0.1 to 1.6) except for the decane-water measurements, *i.e.*, no clear relations between the Bo and the accuracy of ADSA can be established. (b) The Bo as a function of the drop volume (V). It is found that the Bo is not a monotonic function of V . The inset shows the point inflexion in the R_0 (as well as the Bo) is associated with the transition in contact angle (θ) across 90° .

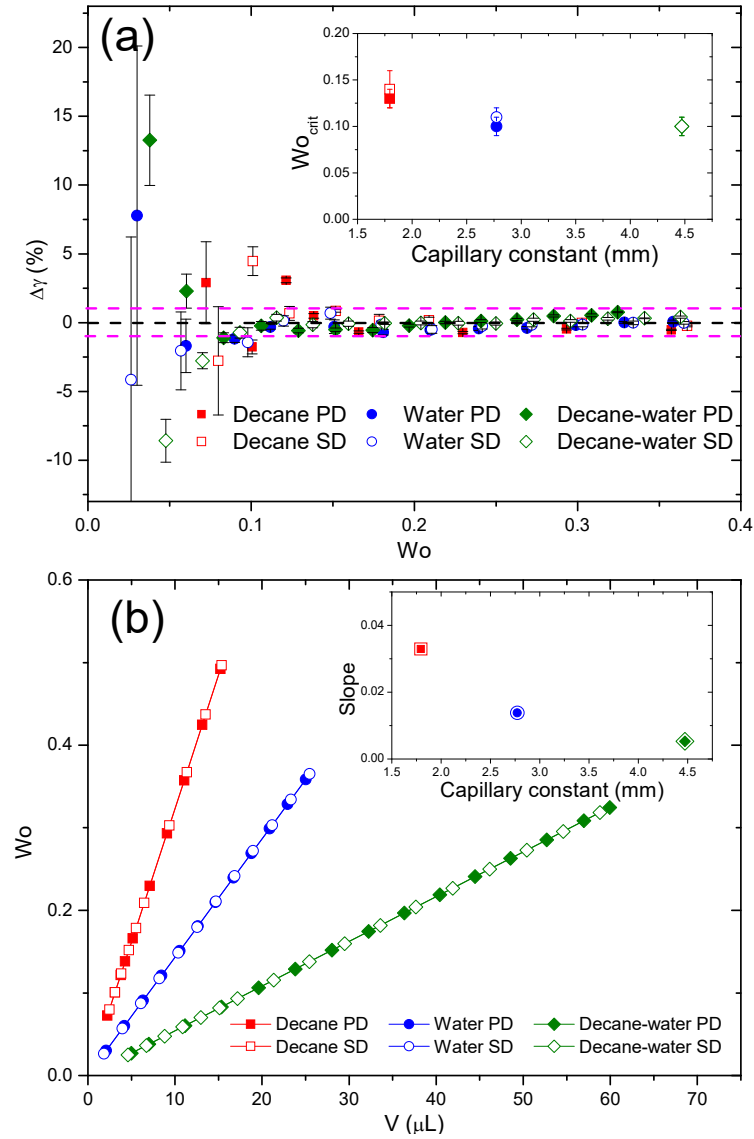


Figure 2.7 (a) Relative errors of measured surface/interfacial tensions ($\Delta\gamma$) for decane, water, and decane-water systems as a function of the Worthington number (Wo), using both PD and SD. It is found that the accuracy of ADSA deteriorates ($\Delta\gamma > 1\%$) upon reducing the Wo . The inset shows the critical Wo (Wo_{crit}) as a function of the capillary constant. (b) The Wo as a function of the drop volume (V). It is found that the Wo and V are linearly correlated, with the slope inversely dependent on the capillary constant (as shown in the inset).

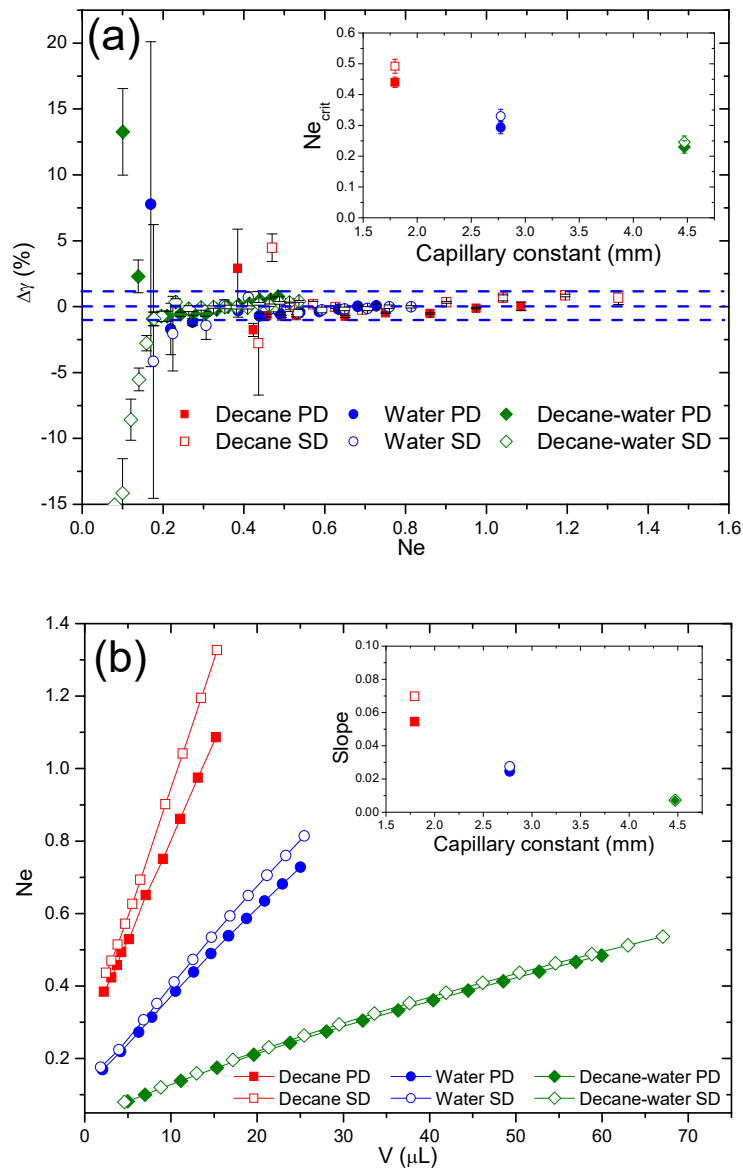


Figure 2.8 (a) Relative errors of measured surface/interfacial tensions ($\Delta\gamma$) for decane, water, and decane-water systems as a function of the Neumann number (Ne), using both PD and SD. It is found that the Ne is capable of predicting the accuracy of ADSA for both PD and SD. The inset shows the critical Ne (Ne_{crit}) as a function of the capillary constant. (b) The Ne as a function of the drop volume (V). It shows that the Ne is a monotonically near-linear function of V, with the slope inversely dependent on the capillary constant (as shown in the inset).

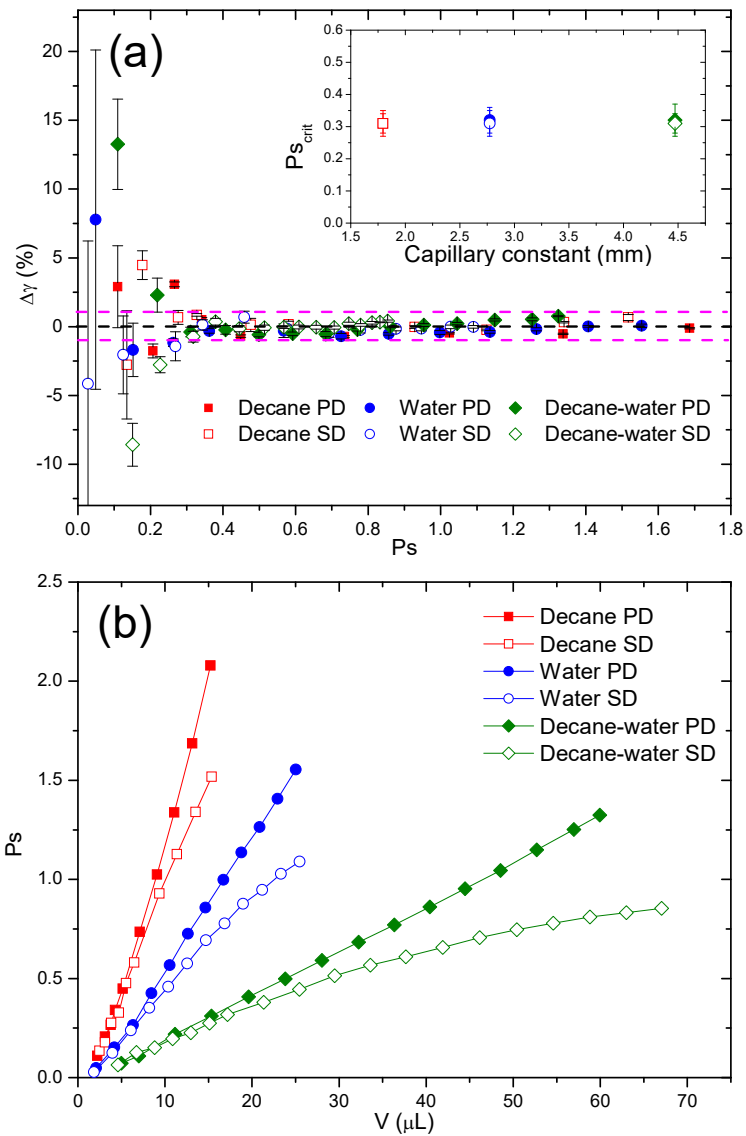


Figure 2.9 (a) Relative errors of measured surface/interfacial tensions ($\Delta\gamma$) for decane, water, and decane-water systems as a function of the shape parameter (Ps), using both PD and SD. It is found that the accuracy of surface/interfacial tension measurements deteriorates ($\Delta\gamma > 1\%$) upon reducing the Ps . As shown in the inset, the critical Ps (Ps_{crit}) is independent from the capillary constant. (b) The Ps as a function of the drop volume (V).

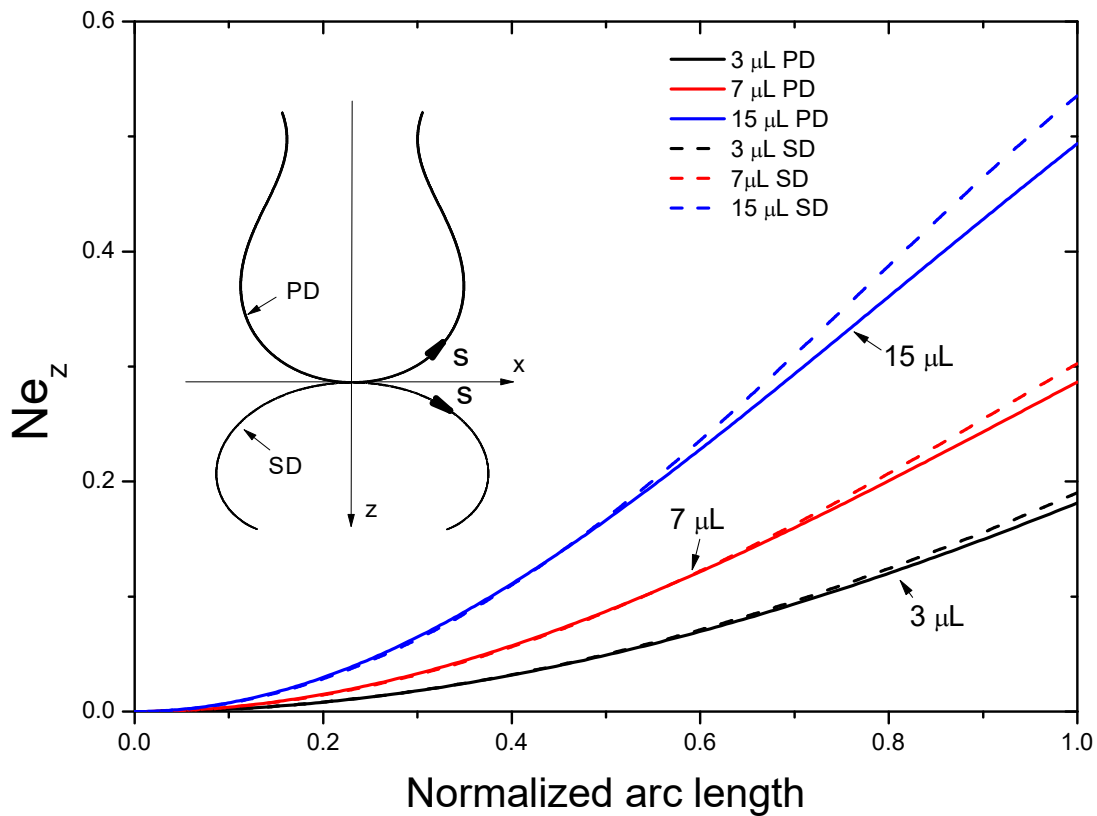


Figure 2.10 Theoretical calculation of the local Neumann number (Ne_z) along the normalized arc length from the drop apex to the three-phase contact line, for PD and SD of water with the volume of 3, 7, and 15 μL , respectively. These three volumes were selected to represent drop volumes less than, close to, and larger than the critical volume for water ($V_{\text{crit}} \approx 7 \mu\text{L}$), based on results shown in Figures 2.4 and 2.8. It shows that the Ne_z can be used to evaluate the relative importance of the local drop profile on the accuracy of ADSA.

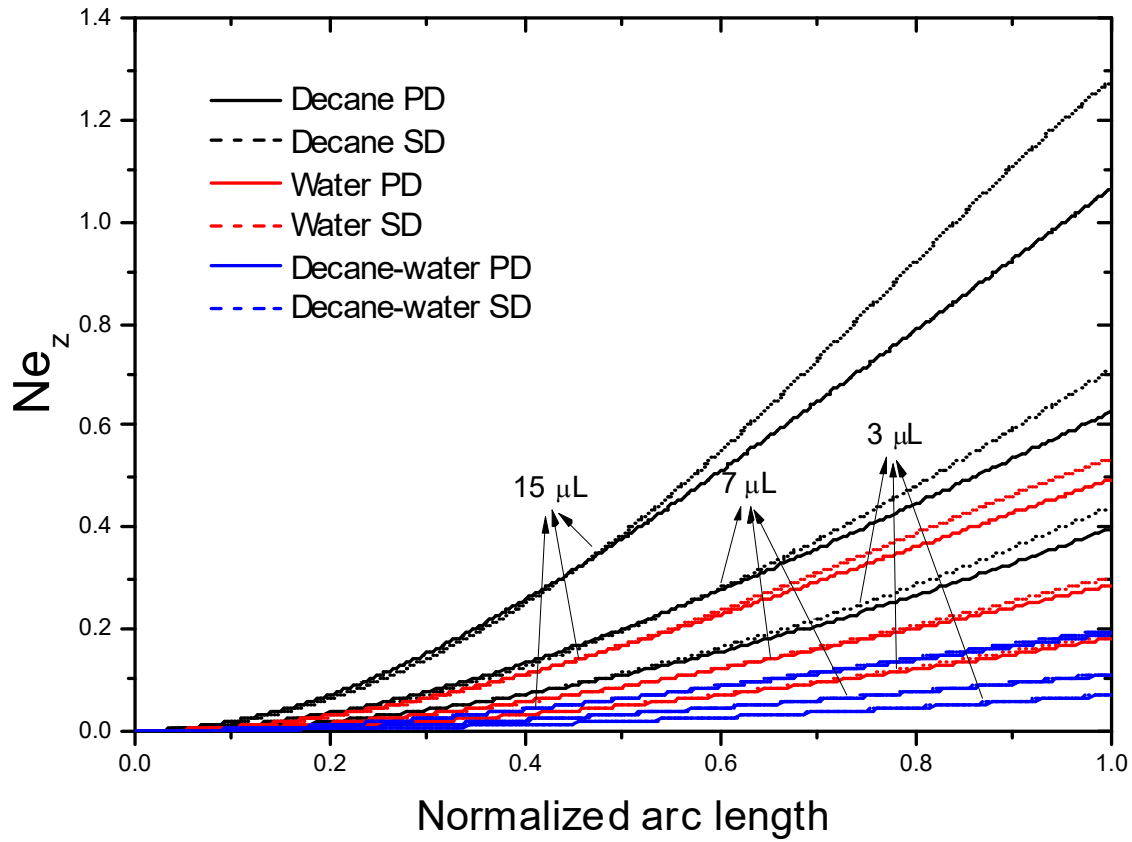


Figure 2.11 Theoretical calculation of the local Neumann number (Ne_z) along the normalized arc length from the drop apex to the three-phase contact line for PD and SD of decane, water, and decane-water with the volume of 3, 7, and 15 μL , respectively.

Table 2.1 Various definitions of the Bond number $Bo = \left(\frac{L}{c}\right)^2$ for evaluating the accuracy of drop shape analysis.

Definition	Symbol	Characteristic length (L)	Formula	Reference
Classical Bond number	Bo	R_0	$Bo = \frac{\Delta\rho g R_0^2}{\gamma}$	41
Worthington number	Wo	$\sqrt{\frac{V}{\pi D_t}}$	$Wo = \frac{\Delta\rho g V}{\gamma \pi D_t}$	40
Neumann number	Ne	$\sqrt{R_0 H}$	$Ne = \frac{\Delta\rho g R_0 H}{\gamma}$	This work

* L is the characteristic length; c is the capillary constant, $c = \sqrt{\frac{\gamma}{\Delta\rho g}}$.

Chapter 3. Development of the closed-loop ADSA

3.1 Introduction

Effective manipulation of liquid droplets plays an important role in a wide range of scientific and industrial applications, such as synthesis of thin-film materials,⁴⁹ control of interfacial reactions,⁵⁰ study of surface rheology,⁵¹ and operation of digital microfluidics.⁴ In these applications, droplets serve as a miniaturized platform that provides a number of unique advantages over traditional interfacial models such as the classical Langmuir trough.⁵ First, the small volume of droplets facilitates study of scarce or expensive samples, such as biological or clinical fluids. Second, compared to bulk systems, droplets possess a much larger surface-area-to-volume ratio that makes droplets an ideal soft platform for studying surface reaction and interfacial assembly. Third, due to system miniaturization, it is feasible to ensure a rigorous environmental control, such as temperature and experimental atmosphere, with the droplet system, thus allowing for environmental studies across the droplet surfaces.⁶

Compared to the control of a flat surface as in the classical Langmuir trough, effective control and manipulation of a single droplet is not a trivial task. In general, the profile of a free-standing droplet is determined by the balance of gravitational and surface tension forces as predicted by the Bond number, $Bo = \frac{\Delta\rho g R^2}{\gamma}$, where $\Delta\rho$ is the density difference across the drop surface, g is the gravitational acceleration, R is the characteristic radius of the droplet, and γ is the surface tension. Droplets with very small Bond numbers, such as micron-sized droplets, are generally considered as spherical beads.⁵² The key parameter for manipulating such droplets is their

volume; while the surface area can be calculated by a spherical approximation and the surface tension is routinely assumed to be a constant.⁵³ A number of techniques have been developed to manipulate the volume of micron-sized droplets.^{52, 53, 54}

However, when the Bond number is sufficiently large, *e.g.*, for millimeter-sized droplets and/or at the presence of surfactants, the drop profile can be significantly deformed by gravity to assume a Laplacian shape.^{5, 55} In these cases, the surface area of the droplet cannot be correlated with its volume using a simple spherical approximation. Meanwhile, the surface tension usually varies with the surface area at the presence of surfactants. Hence, all droplet properties, including its volume, surface area, and surface tension, need to be individually controlled for effective droplet manipulation. Nevertheless, in most applications, one can only control the drop volume using a high-precision syringe pump. Neither surface area nor surface tension of the droplet can be directly controlled with current techniques. Cabrerizo-Vilchez and coworkers have developed a fuzzy-logic algorithm to control the surface pressure or surface area of a pendant drop.⁵⁵ In spite of a suitable control method, the fuzzy-logic algorithm requires the definition of input and output fuzzy sets for every control process, which is not a trivial task.

In this chapter, we developed a novel feedback control method for manipulating millimeter-sized droplet based on axisymmetric drop shape analysis (ADSA). We have developed a high-speed ADSA algorithm capable of real-time analysis of droplet properties, including its volume, surface area, and surface tension. By coupling the real-time ADSA with a proportional-integral-derivative (PID) controlled motorized syringe, we have developed the first closed-loop ADSA that is capable of precisely controlling the volume, surface area, and surface tension of a millimeter-sized droplet.

To demonstrate the feasibility and advantages of this droplet manipulation method, we have engaged it in three applications of importance in various surface science studies. In the first application, we maintained the volume of a water droplet over a prolonged time period by automatically compensating natural evaporation. In the second application, we demonstrated the feasibility of controlling the surface area of an oscillating droplet for *in vitro* biophysical simulations of natural pulmonary surfactant. By precisely controlling surface area variations during dynamic droplet oscillation, our method allows high-fidelity *in vitro* biophysical simulations of respiratory mechanics. In the third application, we demonstrated the effective control of surface pressure during compression of a self-assembled phospholipid monolayer. By controlling surface pressure over time, we implemented the first *in situ* Langmuir-Blodgett (LB) transfer from a monolayer-covered droplet. All these applications have demonstrated that closed-loop ADSA is highly practical in automating droplet manipulation in a variety of material and surface science applications, such as thin-film fabrication, self-assembly, and biophysical study of pulmonary surfactant.

3.2 Materials and methods

3.2.1 Materials

The water used in this study was Milli-Q ultrapure water (Millipore, Billerica, MA). It has a resistivity greater than 18 M Ω ·cm at room temperature. The pulmonary surfactant used in this study was Infasurf (Calfactant), which was a gift from ONY Inc. (Amherst, MA). Infasurf was purified from whole-lung bronchopulmonary lavage of newborn calves. Through an extraction process, Infasurf retained all of the hydrophobic components of bovine endogenous surfactant including phospholipids, cholesterol, and most hydrophobic surfactant proteins (SP-B and SP-C).^{56, 57} Infasurf has a total phospholipid concentration of 35 mg/mL and is stored frozen in

sterilized vials. On the day of experiments, it was thawed and diluted to a phospholipid concentration of 5 mg/mL with a saline buffer of 0.9% NaCl, 1.5 mM CaCl₂, and 2.5 mM HEPES, adjusted to pH 7.0. Dipalmitoyl phosphatidylcholine (DPPC) was purchased from Avanti Polar Lipids (Alabaster, AL) and used without further purification. DPPC was dissolved in chloroform to form a 1 mg/mL stock solution.

3.2.2 Experimental methods

Since its development, ADSA has been routinely used as an open-loop system for determining properties of drop/bubble.^{10, 12} Here, we further developed ADSA into a closed-loop system in which droplet properties determined in real time are used as feedback control parameters to actuate the droplet towards desired targets.⁵⁸ A diagram of the feedback control loop is illustrated in **Figure 3.1**. Besides the essential components in CDS, a digital PID controller was directly integrated into ADSA. In the closed-loop feedback control system, ADSA continuously calculates the error, *i.e.*, the difference between the target values and the current values, and thereafter automatically actuates the droplet towards the target values using a motorized syringe (consisting of a high-precision servomotor and a piston-syringe system) with PID control. The transient state of the droplet can be controlled by administering proper PID gains.

To develop CDS into an automated control system, SD configuration was applied. The volume, surface area, and surface tension of the droplet are determined from real-time image analysis (*i.e.*, no prior image acquisition was needed) with the ultrafast ADSA algorithm capable of analyzing the drop shape at a frequency of 10 Hz.^{6, 58, 59} This processing speed is mainly limited by the computational demands for real-time ADSA analysis.

In comparison with previous droplet manipulation methods, the closed-loop ADSA possesses several advantages. (1) To the best of our knowledge, the closed-loop ADSA is the first method

capable of controlling the volume, surface area, or surface tension of millimeter-sized single droplets. Previous methods can only control drop volume. However, knowledge about the surface area and surface tension of the droplet can be only obtained by post-experimental analysis of drop images acquired during the experiments. Hence, control parameters such as area compression ratios and targeting surface tension values cannot be set *a priori*. In comparison, the closed-loop ADSA analyzes the deformed drop shape in real time and hence eliminates the need of image acquisition for post-analysis. Consequently, the closed-loop ADSA allows live manipulation of a droplet. (2) Since the closed-loop ADSA manipulates the droplet by directly controlling properties of the target droplet, it is independent of the physical methods of fluid actuation, regardless of the fluid is driven by a motorized syringe or by a piezoelectric transducer. (3) Being a free-standing method, although the closed-loop ADSA is demonstrated here with a sessile drop setup, it can be readily applied to manipulate other drop or bubble shapes.

For biophysical simulations of pulmonary surfactant, detailed experimental protocols can be found elsewhere.^{6, 59} Briefly, a droplet ($\sim 10 \mu\text{L}$) of 5 mg/mL Infasurf was dispensed onto the CDS drop pedestal, maintained within an environmental chamber that controls the physiologically relevant conditions, *i.e.*, 37 °C and 100% relative humidity. After drop formation, the surface tension quickly decreased to an equilibrium value of approximately 22-25 mN/m,⁶⁰ indicating formation of an adsorbed surfactant film at the air-water interface. Once the equilibrium was established, the adsorbed surfactant film was compressed and expanded at a rate of 5 seconds per cycle by withdrawing and injecting water into the droplet using the motorized syringe. The compression ratio was controlled to be less than 20% of the initial surface area to simulate normal tidal breathing. A minimum of five continuous compression–expansion cycles

were studied for each droplet. It was observed that the cycles became repeatable after the first cycle.

For the study of self-assembled phospholipid monolayers at room temperature, a tiny amount of 1 mg/mL DPPC stock solution was spread using a microsyringe onto a droplet of pure water of which the surface tension was recorded as γ_0 .⁶¹ The droplet was then slowly expanded to increase surface tension (γ) until the corresponding surface pressure ($\pi = \gamma_0 - \gamma$) was reduced to ~ 1 mN/m. The droplet was left undisturbed for an additional 1 min to allow evaporation of the solvent. The spread DPPC monolayer was subsequently compressed at a quasi-equilibrium rate of 0.06 cm²/min, corresponding to 0.17% initial surface area per second. Langmuir-Blodgett (LB) transfer from the droplet was implemented by lifting a small piece of freshly peeled mica sheet at a speed of 1 mm/min, under controlled surface pressure. Topographical images were obtained using an Innova AFM (Bruker, Santa Barbara, CA). Samples were scanned in air in contact mode with a silicon nitride cantilever of a spring constant of 0.12 N/m and a tip radius of 2 nm. Lateral structures were analyzed using Nanoscope Analysis (version 1.5).

3.3 Results and discussion

3.3.1 Control of drop volume and its application in compensating evaporation

In this study, we demonstrate direct control of drop volume with the closed-loop ADSA. **Figure 3.2** shows the manipulation of a 60 μ L water droplet on the CDS platform at room temperature. The volume of the droplet (panel c) was decreased and increased stepwise with a step of every 10 μ L, followed by steps of every 20 μ L and 40 μ L, respectively. Images of this droplet at different volumes are shown as inserts in panel a. It is clear that the volume change was controlled to be largely linear with respect to time and without significant overshoot once reaching the target values within a 1% tolerance. Response to the control was fast. Regardless of

the magnitude of volume change, the target values were reached within 1 second. It can be also seen that during the manipulation of drop volume, the surface tension (panel a) of pure water fluctuates at 71 ± 2 mN/m, in agreement with the literature value.⁶¹ The deviation mostly takes place upon reducing the drop volume. This is most likely due to traces of impurities (that cause surface tension decrease) and/or intrinsic artifacts of drop shape analysis at small volumes (that cause surface tension increase).^{40, 62}

We further demonstrate the usefulness of the ADSA-based volume control by solving a scientific problem, *i.e.*, droplet evaporation. Evaporation is an inevitable problem of any droplet-based apparatus in which the drop volume decreases with time due to evaporation at a rate affected by the surface area of the droplet, diffusivity of the liquid, and the environmental conditions.⁴⁰ For instance, protein adsorption may take several hours to complete, during which evaporation may cause significant artifact by contracting the air-water interface of the droplet.⁶³ ⁶⁴Another example in which the compensation of droplet evaporation is essential is the study of gas adsorption at the air-water interface.⁶⁵ Volume loss is especially problematic for small droplets as the highly curved drop surface increases the chemical potential of evaporation.⁶⁶ Here, we demonstrate that the ADSA-based volume control maintains a constant drop volume over a prolonged time period by automatically compensating the effect of evaporation. As shown in **Figure 3.3**, without control, the volume of a 60 μ L water droplet shrinks by 30% over 30 min due to natural evaporation. In comparison, with the ADSA-based control, the drop volume was maintained at constant over the same time period with volume variations less than 0.5%.

It should be noted that it is also possible to control the volume of a droplet using a high-precision syringe pump, if only the linear displacement of the syringe pump is properly calibrated and converted to variations in the drop volume. However, our ADSA-based method

represents a novel feedback control system that drives the motor to directly control the drop volume with the value determined in realtime by ADSA. Hence our method is more accurate, faster, and does not require calibration. The entire process is automatic without the need of any human intervention.

3.3.2 Control of surface area and its application in studying pulmonary surfactants

Compared to the control of drop volume, the control of surface area and surface tension of the droplet is exceedingly complicated due to the nonlinearity of these two properties. To demonstrate the nonlinearity of surface area and surface tension with respect to the drop volume, we have conducted a comparative experiment of shrinking three droplets of the same initial volume. These are a pure water droplet, a DPPC-covered water droplet, and an Infasurf droplet. **Figure 3.4** shows the surface area (panel a) and surface tension (panel b) of these three droplets as a function of the reducing volume. It is clear that only the surface area of the pure water droplet is nearly linearly correlated with the drop volume. Nonlinearity in surface area exists for both DPPC-covered and Infasurf droplets, due to drop deformation upon reducing volume. Surface tensions of all three droplets are nonlinearly correlated with the drop volume, in which the surface tension of pure water remains unchanged while reducing volume, and the surface tensions of DPPC-covered and Infasurf droplets decrease quickly to near-zero value upon reducing volume (*i.e.*, the compression of lipid monolayer at the air-water interface).

Nonlinearity of the surface area and surface tension renders the control of these two droplet properties using a regular syringe pump impossible. However, being a feedback control system, our closed-loop ADSA can readily control the surface area or surface tension of the droplet without additional difficulties compared to the control of drop volume. In this study, we demonstrate the direct control of droplet surface area with closed-loop ADSA.

We first demonstrate the ADSA-based area control as shown in **Figure 3.5**. The surface area of a 0.6 cm^2 water droplet (panel b) was decreased and increased stepwise with a step of every 0.1 cm^2 , followed by steps of every 0.2 cm^2 and 0.4 cm^2 , respectively. Images of this droplet at different surface areas are shown as inserts in panel a. It can be found that the change of surface area was controlled largely linear with respect to time without significant overshoot once reaching the target values within a 1% tolerance, with the similar tendency of drop volume control. During the manipulation of surface area, the surface tension (panel a) of pure water is largely unchanged and drop volume follows the same tendency of surface area.

We further demonstrate the usefulness of the ADSA-based area control by *in vitro* biophysical simulations of pulmonary surfactant (PS). A key requirement of *in vitro* biophysical simulations of PS is to mimic the intra-alveolar environment of the lungs. This requires not only rigorous control of experimental conditions to physiological relevance, such as the core body temperature of $37 \text{ }^\circ\text{C}$ and 100% relative humidity, but also high-fidelity simulation of respiratory cycles during normal tidal breathing, such as the respiratory rate (*e.g.*, 5 seconds per cycle) and the control of surface area variations to be less than 20% per cycle.⁶⁷ Numerous studies have demonstrated that variations in alveolar surface area during respiration are small.^{67, 68, 69} Surface area of the lungs does not change more than 30% during a deep breath between 40 and 100% total lung capacity (TLC). During normal tidal breathing between 40 and 50% TLC, the area variation is less than 10%.^{67, 68, 69} All this physiological evidence suggests that natural PS films must have a very low compressibility contributing to lung recoil.⁷⁰ However, direct control of surface area during droplet oscillation was not possible in previous *in vitro* simulations.

Figure 3.6 demonstrates the advantages of closed-loop ADSA in biophysical simulations of a natural PS, Infasurf, under physiologically relevant conditions. It can be seen that with surface

area control, the adsorbed surfactant film was compressed precisely by 15% area reduction (mimicking exhalation), and subsequently expanded back to its original area (mimicking inhalation). A minimum surface tension of ~ 2 mN/m was reached with the 15% compression, indicating a low film compressibility of approximately 0.5 (mN/m) $^{-1}$. The compression and expansion curves coincide closely with each other without showing a significant hysteresis, which represents an ideal biophysical simulation of the respiratory cycle of natural PS.

In contrast, without surface area control, the actual compression ratio of surfactant films cannot be set *prior to* the dynamic cycling experiments. Consequently, the surfactant films are commonly over compressed or under compressed, thus failing to mimic the physiological conditions of respiration. As the example shown in Figure 3.6, the surfactant film without area control was compressed by 22% area reduction. It is found that as soon as the area was reduced beyond 15%, the surface tension did not decrease anymore. Rather, the compression curve leveled off at the minimum surface tension, indicating extensive film collapse. Collapse of the alveolar surfactant film is uncommon in mammalian lungs under normal conditions.⁷¹ Hence, this extra area compression is considered to be "overcompression" that is an artifact introduced by the *in vitro* biophysical simulation.⁷² Because of this overcompression, the compression-expansion cycle shows a significant hysteresis loop. The area enclosed in the hysteresis loop indicates the amount of mechanical energy loss per respiratory cycle, which is again an artifact for *in vitro* biophysical simulation of natural PS.¹³

3.3.3 Control of surface tension/pressure

To demonstrate the control of surface tension/pressure, we used the CDS as a miniaturized Langmuir balance to study the compression isotherm of a self-assembled DPPC monolayer at room temperature. **Figure 3.7** shows the surface pressure of the DPPC monolayer as functions of

the relative surface area (π -A curve) and the compression time (π -t curve), respectively. It can be seen that the π -A curve is consistent with well-characterized DPPC compression isotherms reported in literature.^{56, 73, 74} At large surface area and low surface pressure, the DPPC monolayer is in a fluid-like liquid-expanded (LE) phase, while the surface pressure only increases slowly with area reduction. After passing a phase transition plateau at about 8.5 mN/m, the DPPC monolayer is transformed into a solid-like tilted-condensed (TC) phase at which the surface pressure increases rapidly with compression, indicating a very low film compressibility for the TC phase DPPC monolayer.⁷⁵

As demonstrated by the π -t curve shown in Figure 3.7, with the ADSA-based surface tension/pressure control, we were able to compress the DPPC monolayer to a target surface pressure (*i.e.*, 8.5, 20, 30, 40, 50, and 60 mN/m) and maintain it over a 100 s period. It can be seen that when the controlled pressure reaches 30 mN/m, a small overshoot appears due to hysteresis incurred by stiction of the piston-syringe system. However, the controller is able to correct the overshoot and bring the steady-state surface pressure to the target value. The steady-state error of this control is <1.5%.

The precise control of surface tension/pressure over time allows extended investigation of self-assembled monolayers and thin-films fabricated at the droplet surface. One such application is *in situ* Langmuir-Blodgett (LB) transfer from the droplet surface. To date, LB transfer of films from the air-water interface to a solid substrate under controlled surface pressure is primarily implemented with a Langmuir trough.⁷⁵ After LB transfer, the film can be studied in details by various microscopic and spectroscopic techniques for characterizing its lateral structure and molecular organization.^{56, 76, 77} Here, taking advantage of the ADSA-based surface tension/pressure control, we have implemented the first *in situ* LB transfer of DPPC monolayer

from the droplet surface. During the LB transfer, ADSA analysis was restricted to partial drop profiles that were not disturbed by the substrate passing the air-water interface. The insert in Figure 3.7 shows an AFM topographic image of the DPPC monolayer transferred within the phase transition plateau region, *i.e.*, 8.5 mN/m. The AFM image shows clearly coexistence of the LE phase and the signature kidney-shaped TC domains well-documented in literature.^{56, 78}

3.4 Summary

We have developed a novel closed-loop ADSA, integrated into the constrained drop surfactometer (CDS), for manipulating millimeter-sized droplets. The closed-loop ADSA extends applications of the traditional drop shape analysis from a surface tension measurement methodology to a sophisticated tool for automatically manipulating droplets in real-time. We have demonstrated the feasibility and advantages of closed-loop ADSA in three applications, including control of drop volume by automatically compensating natural evaporation, precise control of surface area variations for high-fidelity biophysical simulations of natural pulmonary surfactant, and steady control of surface pressure for *in situ* Langmuir-Blodgett transfer from droplets. All these applications have demonstrated the accuracy, versatility, applicability, and automation of this new ADSA-based droplet manipulation technique. Combining with CDS, the closed-loop ADSA holds great promise for advancing droplet manipulation in a variety of material and surface science applications, such as thin-film fabrication, self-assembly, and biophysical study of pulmonary surfactant.

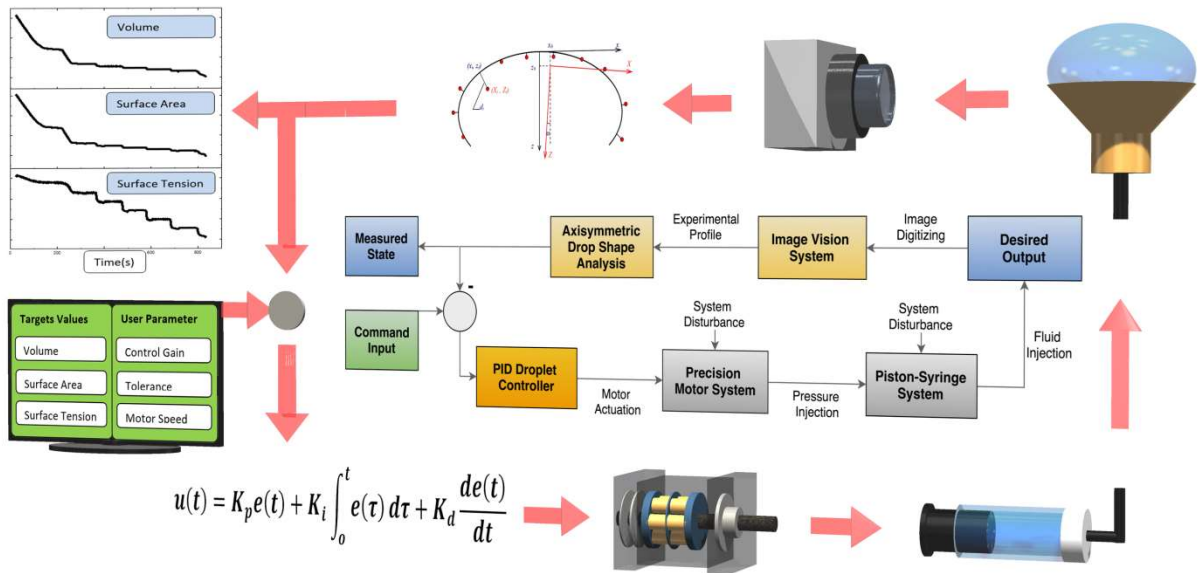


Figure 3.1 Diagram of the closed-loop axisymmetric drop shape analysis (ADSA) feedback control system integrated into the constrained drop surfactometer (CDS). In CDS, a liquid droplet is "constrained" on a 3-5 mm carefully machined pedestal with a knife-sharp edge. The droplet is continuously monitored by ADSA in real-time. Properties of the droplet, including its volume, surface area, and surface tension, are controlled with the closed-loop ADSA. An integrated PID controller continuously calculates the error, *i.e.*, the difference between the target values and the current values, and converts the error into a command signal with proper PID gains. The resultant command signal controls a motorized syringe, consisting of a high-precision servomotor and a piston-syringe system, to actuate the droplet towards the target values.

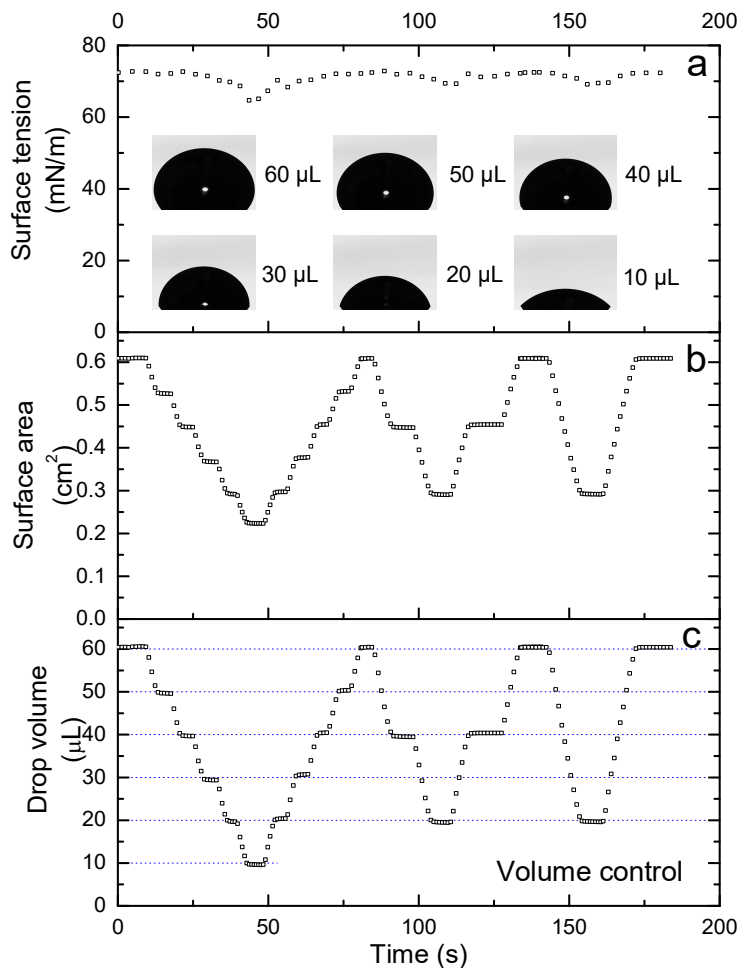


Figure 3.2 Demonstration of the closed-loop ADSA for controlling drop volume. The volume of a 60 μL water droplet (panel c) was decreased and increased stepwise with a step of every 10 μL , followed by steps of every 20 μL and 40 μL , respectively. Images of this droplet at different volumes are shown as inserts in panel a. It is clear that the change of volume was controlled to be largely linear without significant overshoot once reaching the target values within a 1% tolerance. During manipulation of drop volume, the surface tension (panel a) of pure water is largely unchanged, and the surface area (panel b) of the water droplet also varies largely linearly with respect to time.

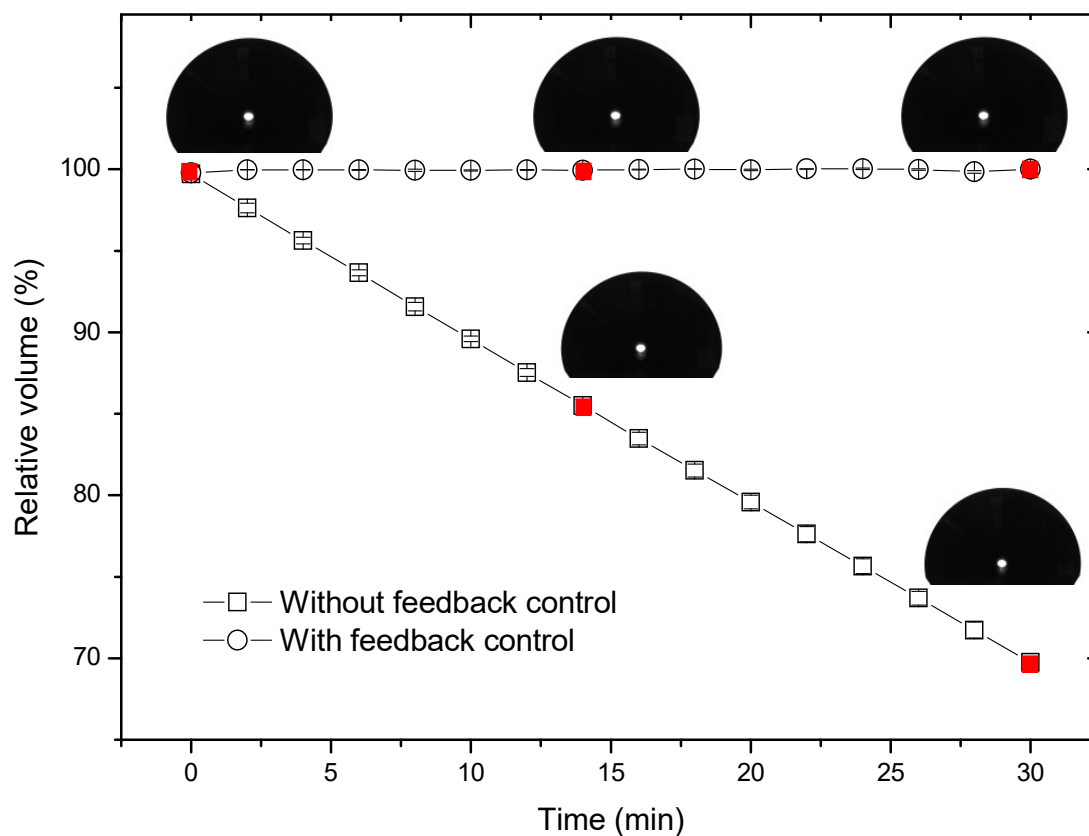


Figure 3.3 Demonstration of the closed-loop ADSA for maintaining a constant drop volume by automatically compensating evaporation. Without the control, the volume of a 60 μL water droplet shrinks by 30% over 30 min due to natural evaporation. With the control, the drop volume was maintained at constant over the same time period with volume variations less than 0.5%. Results are shown as mean \pm SD averaged from three repetitions. Inserts are drop images at different time points indicated by red solid symbols on the curves, showing changes in drop volume.

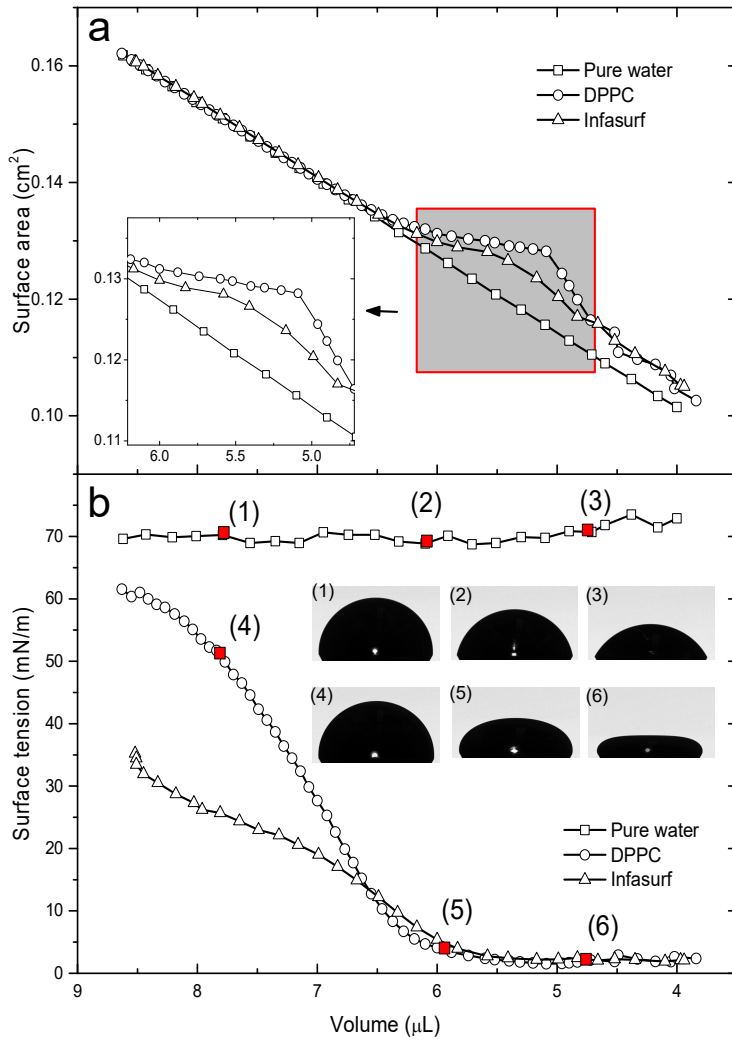


Figure 3.4 Nonlinearity of surface area (a) and surface tension (b) with respect to the drop volume. Three droplets, *i.e.*, a pure water droplet, a DPPC-covered droplet, and an Infasurf droplet, were shrunk linearly in volume. It is clear that only the surface area of the pure water droplet is nearly linearly correlated with the drop volume. Nonlinearity in surface area exists for both DPPC-covered and Infasurf droplets, due to drop deformation upon reducing volume. Surface tensions of all three droplets are nonlinearly correlated with the drop volume, in which the surface tension of pure water remains unchanged while reducing volume, and the surface tensions of DPPC-covered and Infasurf droplets decrease quickly to near-zero value upon reducing volume. Inserts are drop images at different volumes of the three droplets indicated by red solid symbols on the curves.

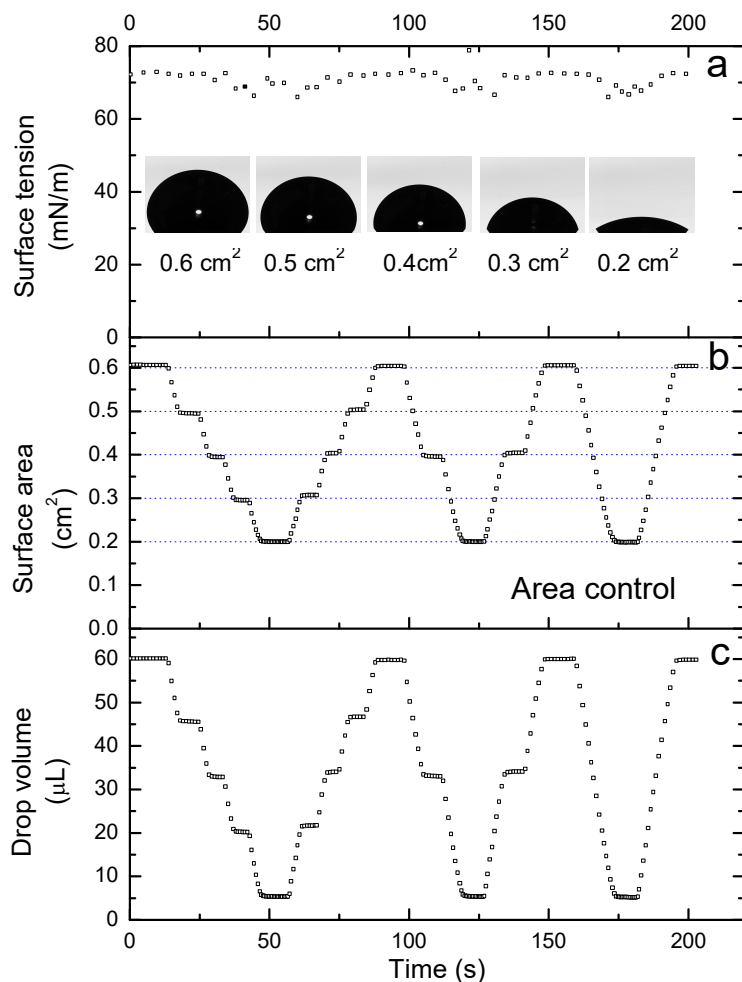


Figure 3.5 Demonstration of the closed-loop ADSA for controlling surface area. The surface area of a 0.6 cm² water droplet (panel b) was decreased and increased stepwise with a step of every 0.1 cm², followed by steps of every 0.2 cm² and 0.4 cm², respectively. Images of this droplet at different surface areas are shown as inserts in panel a. It can be found that the change of surface area was controlled largely linear with respect to time without significant overshoot once reaching the target values within a 1% tolerance, with the similar tendency of drop volume control. During the manipulation of surface area, the surface tension (panel a) of pure water is largely unchanged and drop volume follows the same tendency of surface area.

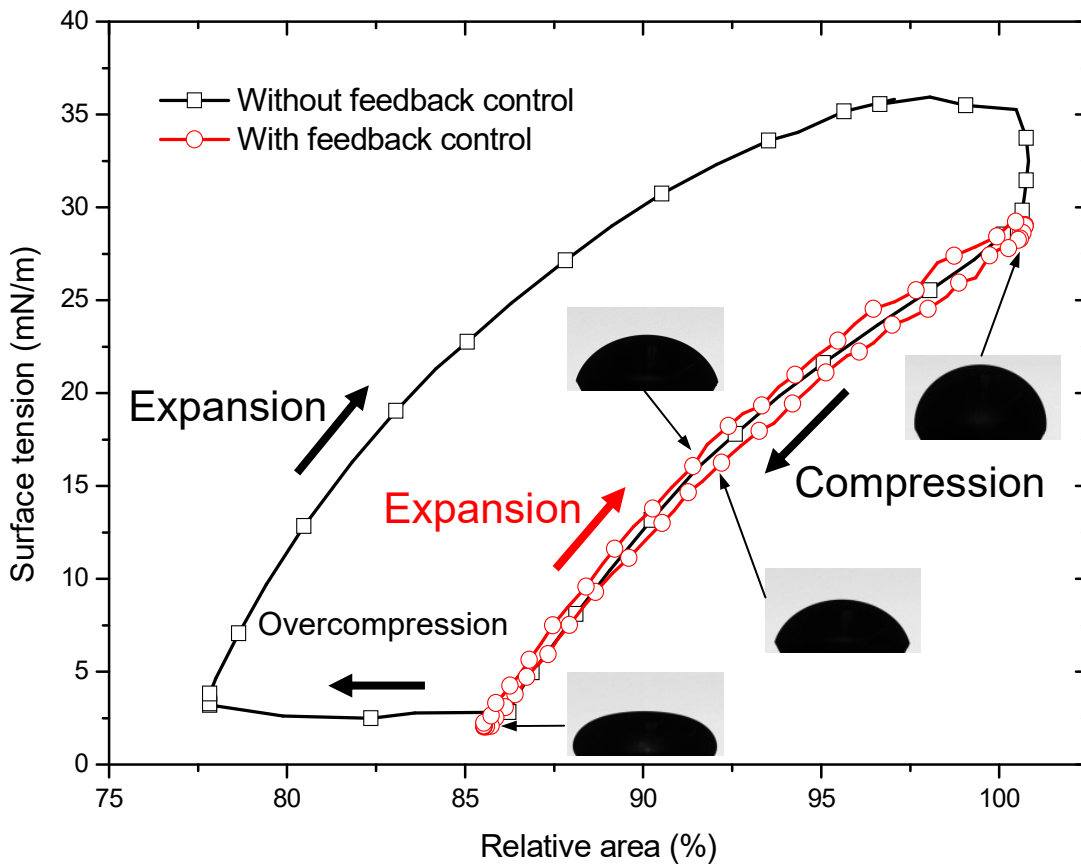


Figure 3.6 Demonstration of the closed-loop ADSA for controlling area variations in biophysical simulation of a natural pulmonary surfactant, Infasurf, under physiologically relevant conditions. With the area control, the surfactant film was compressed precisely by 15% area reduction, and subsequently expanded back to its original area. A minimum surface tension of ~ 2 mN/m was reached with the 15% compression. The compression and expansion curves coincide closely with each other without showing a significant hysteresis. Without the area control, the surfactant film was compressed by 22% area reduction. When the area was reduced beyond 15%, the surface tension did not decrease but leveled off at the minimum value, indicating extensive film collapse, which is an artifact due to overcompression of the surfactant film. Images of the droplets along the cycle path are demonstrative of surface tension being a function of drop shape.

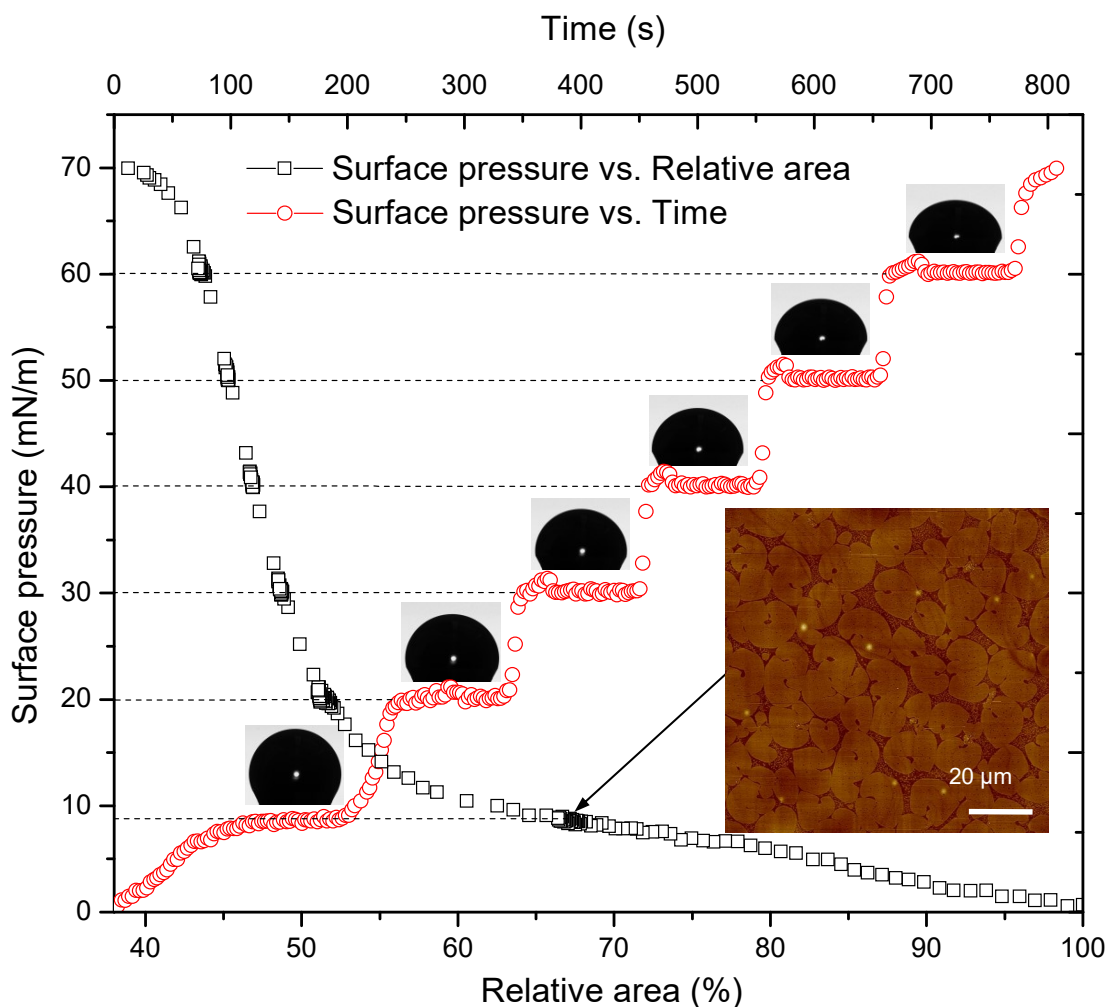


Figure 3.7 Demonstration of the closed-loop ADSA for controlling surface pressure for in situ Langmuir-Blodgett (LB) transfer of DPPC monolayers from the droplet. The obtained surface pressure-area curve is consistent with well-characterized DPPC compression isotherms reported in literature. The surface pressure-time curve shows the compression of the DPPC monolayer to a target surface pressure (*i.e.*, 8.5, 20, 30, 40, 50, and 60 mN/m) and maintained over a 100 s period. When the controlled pressure beyond 30 mN/m, a small overshoot appears due to the hysteresis incurred by stiction of the piston-syringe system. However, the controller is able to correct the overshoot and bring the steady-state surface pressure to the target value. The steady-state error of this control is <1.5%. The insert shows an AFM topographic image (100×100 μm; z-range 5 nm) of the DPPC monolayer transferred under a controlled surface pressure within the phase transition plateau region, *i.e.*, 8.5 mN/m. The image shows clearly coexistence of the LE phase and the signature kidney-shaped TC domains well-documented in literature.

Chapter 4. Study of surface dilational rheology

4.1 Introduction

Proteins and surfactants play a crucial role in a variety of fields, such as food industry, cosmetics, pharmacology, and coating processes.^{79, 80} Among these applications, the most important property of the proteins and surfactants is their adsorption at an interface, which affects many technological processes with a high surface area-volume ratio, *i.e.*, the formation and stabilization of the foams and emulsions. To characterize these adsorption layers at liquid-fluid interfaces, surface dilational rheology is an efficient approach. Surface dilational rheology provides information on the mobility of surfactants which is related to the stability behavior of foams and emulsions.^{26, 81} Moreover, the study of surface dilational rheology provides an opportunity to investigate the dynamic conformation changes of proteins and surfactants adsorbed at the liquid-fluid interface.^{82, 83, 84}

The surface dilational modulus is determined from the amplitudes of the surface area and surface tension oscillations, and from the phase shift between area and tension changes. A variety of methods have been developed for dilational rheology measurement, such as oscillating barrier,^{20, 21} capillary waves,²² bubble pressure,^{23, 24} and drop/bubble shape analysis.^{25, 26, 27} Among these methods, drop/bubble shape analysis stands out with a number of advantages. First, the surface/interfacial properties are calculated from the profile the drop/bubble without directly contacting the surface, thereby avoiding potential contaminations. Second, the drop/bubble can be oscillated with uniform expansion and compression, providing accurate results in characterizing the surface dilational rheology. Finally, usage of small quantities of

liquid sample usage facilitates the study of scarce or expensive sample, such as biological or clinical fluids.

To obtain dilational rheology measurements, the surface tension needs to be characterized in response to the sinusoidal oscillation of surface area. Though there are wide applications of the drop shape analysis in the study of rheology, surface area continues to be controlled in an indirect manner. Compared to the direct control of surface area in the oscillating barrier method, all existing drop/bubble methods are only able to directly control volume using a predefined waveform via an external pumping system, such as motorized syringe. The surface area is assumed to have a linear relation to the drop volume with the assumption of a standard spherical drop/bubble shape. However, with the presence of surfactant at the surface, the drop/bubble is largely deformed from the spherical shape, especially at low surface tension.⁵⁸ Thus, the development of a method that can directly control the surface area is desired.

In this study, we develop a novel waveform generator to directly oscillate the surface area in sinusoidal waveforms, using a feedback control system based on axisymmetric drop shape analysis (ADSA). ADSA is a computer-based surface tension measurement methodology first developed by Neumann and coworkers.^{10, 85} ADSA determines surface tension and surface area by calculating the best fit between the experimental profile and theoretical profiles generated by the Laplace equation of capillarity. We have developed a high-speed ADSA algorithm capable of real-time analysis of surface tension and surface area. By coupling the real-time ADSA with a proportional-integral-derivative (PID) controlled motorized syringe, we have developed a closed-loop ADSA that is capable of precisely control the surface area. For the first time, our methodological advance permitted direct control of surface area oscillated in a sinusoidal pattern,

thus resulting in a precise evaluation of the surface dilational rheological properties of complex fluids, including surfactants and proteins.

To demonstrate the feasibility of this waveform generator in surface rheology study, typical systems of low molecular-weight surfactant and proteins were selected. Non-ionic surfactant dodecyldimethylphosphine oxide ($C_{12}DMPO$) was characterized with different sinusoidal frequencies in a wide range of concentrations. The results were compared with theoretical models and existing experimental results. The dilational modulus of two proteins, β -casein and bovine serum albumin (BSA), were measured in the dynamic adsorption process. The results were compared with each other and the mechanism behind discrepancies was analyzed. All these applications have demonstrated that the waveform generator is a highly practical tool in studying surface dilational rheology.

4.2 Materials and methods

4.2.1 Development of a sinusoidal waveform generator

ADSA determines the surface tension and surface area by numerically fitting the experimental profile to theoretical profiles generated by the Laplace equation of capillarity until the best match is found.^{10, 12} Recently, ADSA was developed into a closed-loop control system where sampled droplet properties are fed back into the system to control the drop/bubble toward desired targets.⁵⁸ A precise target surface area can be reached through this PID control. Here, we extend the close-loop control to a waveform generator. A desired sinusoidal waveform is discretized, and through the discretized time steps, we can control the surface area in a sinusoidal waveform. The waveform can be discretized and controlled to time steps of up to 0.2s, limited by the motor latency between movements. Thus, the upper-limiting frequency of the sinusoidal waveform is around 0.5 Hz (with 10 movements in one period). Prior to every step, the error, *i.e.*, the

difference between the current value and the target value of the next step, is calculated. From this, the PID controller actuates the droplet through the motorized syringe. Moreover, from previous waveform periods, the PID gains are tuned to minimize errors of future periods. Furthermore, to mitigate potential oscillations generated by closed-loop control, an open-loop control component is added, parallel to the existing PID control components.

4.2.2 Materials

C₁₂DMPO (MW=246.4 g/mol), β -casein from bovine milk ($\geq 98\%$ 24kDa), and bovine serum albumin ($\geq 99\%$, ~ 66 kDa), was purchased from Sigma-Aldrich Chemical and used without further purification. Phosphate buffer solution with ion strength of 0.03 (pH=7) and surface tension of 72.5mN/m at 20 °C, prepared from Na₂HPO₄ and NaH₂PO₄ (from Sigma-Aldrich Chemical), was used to dissolve the surfactant and proteins. The water used was Milli-Q ultrapure water (Millipore, Billerica, MA) with a resistivity greater than 18 M Ω ·cm at room temperature. On the day of experiment, a stock solution was prepared and diluted to the desired concentrations. All the measurements were carried out at room temperature (20 \pm 1 °C).

4.2.3 Experimental methods

To demonstrate the capacity of the droplet waveform generator for dilational rheology measurement, we used an experimental setup called the constrained drop surfactometer (CDS), recently developed in our laboratory.^{6, 59, 86} **Figure 4.1** shows the schematic of the CDS setup and the closed-loop ADSA based waveform generator. The CDS is a miniaturized surface tensiometer that utilizes a single liquid droplet confined on a 3-mm diameter drop pedestal. The hydrophilic pedestal features a knife-sharp circular edge that maintains droplet integrity and prevents film leakage even at low surface tensions.⁸⁷ The droplet is manipulated using a

programmable motorized syringe (2.5 mL Gastight) with a maximum displacement speed of 5 mm/s and a resolution of 0.1 μm (equivalent to a volume resolution of approximately 4 nL). The droplet is illuminated with a red-color parallel backlight and is visualized with a machine vision camera with a maximum resolution of 1280 \times 1024 pixels and frame rate up to 30 frames per second. To characterize the properties of the drop, *i.e.*, surface area and surface tension, the real-time image (*i.e.*, no image acquisition was needed) is directly fed in an ultrafast ADSA algorithm capable of analyzing the drop shape up to a frequency of 10 Hz. A predefined sinusoidal curve is generated and used as the input for the feedback control system and the output is the response of the surface tension.

To measure the dilational rheology, a droplet of surfactant or protein solution prepared at the desired concentration, was dispensed onto the CDS drop pedestal. For C₁₂DMPO experiments, the surface tension was monitored continuously (the surface area was kept constant using the closed-loop ADSA⁵⁸) until equilibrium. Surface dilational rheology was measured when the equilibrium was reached. The surface area was oscillated at frequencies of 0.01, 0.025, 0.05, 0.1, and 0.2 Hz in concentrations varying between 0.013 and 0.42 mol/m³. For protein experiments, moduli during the adsorption procedure were measured. It was reported that the modulus *vs.* surface pressure curves, determined in the adsorption process, are independent of protein concentration.^{21, 82, 88} For the sake of comparison with existing literature values, the protein solution with concentration of 10 mg/L was selected. Oscillation of the surface area was carried out with the frequency of 0.1 Hz over the course of the adsorption process. Thus, we were able to simultaneously measure the dynamic surface tension and the modulus from the early stages of the adsorption process until equilibrium was reached.

Calculation of dilational modulus. The surface dilational modulus is defined as the increase in surface tension (γ) in response to a small relative increase in surface area (A)

$$E = \frac{d\gamma}{d \ln A} \quad (\text{Eq. 4.1})$$

In the oscillating system, the modulus is a complex quantity with both a real and an imaginary component defined as follows

$$E = E_r + iE_i \quad (\text{Eq. 4.2})$$

where E_r is the real component (elastic modulus) and E_i is the imaginary component (viscous modulus).

The total modulus can be regarded as a change in the energy of the system in response to the change in area. The elastic modulus can be thought as the energy stored in the system, while the viscous modulus reflects the loss of energy. The elastic and viscous moduli can also be expressed in terms of the total modulus ($|E|$) and the phase angle (φ) as follows

$$E_r = |E| \cos(\varphi) \quad (\text{Eq. 4.3})$$

$$E_i = |E| \sin(\varphi) \quad (\text{Eq. 4.4})$$

With a small amplitude harmonic perturbation of the surface area, the magnitude and phase of the surface tension response is directly associated to the dilational modulus. It was proven that sufficiently small amplitude of area deformation (*i.e.*, <10%) guaranteed a linear response.⁸⁹ In our experiments, the controlled amplitude of surface area oscillation is restricted within 10%. The surface area is oscillated following the predefined equation

$$A = A_0 + \tilde{A} \sin(2\pi t / \tau) \quad (\text{Eq. 4.5})$$

where A_0 is the offset of the surface area, \tilde{A} is the amplitude of the surface area oscillations, and τ is the period. The harmonic response of the surface tension γ reads

$$\gamma = \gamma_0 + \tilde{\gamma} \sin(2\pi t / \tau + \varphi) \quad (\text{Eq. 4.6})$$

where γ_0 is the offset of the surface tension, $\tilde{\gamma}$ is the amplitude, and φ is the phase shift of the surface tension to the surface area. From the control parameter of sinusoidal waveform for surface area, we can directly obtain A_0 and \tilde{A} . $\tilde{\gamma}$ and φ is calculated by curve fitting of the measured surface tension. Thus, the modulus can be calculated by

$$|E| = A_0 \frac{\tilde{\gamma}}{\tilde{A}} \quad (\text{Eq. 4.7})$$

$$E_r = A_0 \frac{\tilde{\gamma}}{\tilde{A}} \cos(\varphi) \quad (\text{Eq. 4.8})$$

$$E_i = A_0 \frac{\tilde{\gamma}}{\tilde{A}} \sin(\varphi) \quad (\text{Eq. 4.9})$$

4.3 Results and discussion

4.3.1 The accuracy of sinusoidal waveform generator

We first demonstrate the direct control of surface area with the closed-loop ADSA to generate a sinusoidal waveform with assigned parameters using a water droplet. **Figure 4.2** shows the manipulation of the droplet with the offset of surface area set as 0.2 cm^2 on the CDS platform at room temperature. The surface area was increased and decreased following the theoretical sinusoidal curve with amplitude of 10% (0.02 cm^2) and a period of 10 s. It can be found that the experimental area can closely follow the theoretical curves in this case with no overshoot in the amplitude and delay of the phase.

To quantify the accuracy of the controlled area as a function of frequency, the relative error between the measured surface area and the theoretical sinusoidal curve, *i.e.*, $\varepsilon = |A_{\text{measured}} - A_{\text{theoretical}}| / A_{\text{theoretical}}$, were provided. The relative errors of offset, amplitude, and period are determined with frequency varying from 0.01 Hz to 0.5 Hz, as shown in **Figure 4.3**. To compute the accuracy of the experimental results matching to the sinusoidal waveform in different frequencies, R^2 is also provided in the panel d. It can be found that when the frequency is below 0.2 Hz, the relative errors stay small with the period owning the highest accuracy, *i.e.*, $e_{\tau} < 0.05\%$. The relative error of the amplitude is the most sensitive parameter but is still less than 5% when frequency is below 0.2 Hz. Note that our method is also valid and with a high accuracy at lower frequency, *i.e.*, less than 0.01 Hz. When frequency increases to 0.5 Hz, the accuracy of the waveform decreases with the amplitude deviating the most from the theoretical curve, *i.e.*, $e_{\bar{A}}$ becomes larger than 10%. The R^2 shows the similar trend. When frequency is below 0.2 Hz, the R^2 is over 0.99, indicating that the experimental results closely follow the theoretical curve. The R^2 reduced to 0.97 once the frequency reaches to 0.5 Hz. The errors in the high frequency are mainly attributed to the fewer samples acquisition and the limitation of the motor response. It should be noted that, the limitation of the drop shape analysis is also close to the frequency of 0.5 Hz. A specific investigation indicates that the drop cannot be considered at mechanical equilibrium for frequencies beyond 1 Hz in air water systems.⁹⁰ This indicates that our method is applicable to almost the whole range of the drop shape analysis. It should also be noted that the frequency used in our study is in the low frequency range. The relaxation processes responsible for the dilational rheology of the surface, however, occur in a broad time-scale. To gain a comprehensive understanding of the relaxation processes, a combination of the methods with

different frequency range should be considered. In this study, we only focus on the slow relaxation processes in the surfactant and protein layers.

4.3.2 Dilational modulus of surfactants

To illustrate the procedure of modulus calculated from the experimental data, **Figure 4.4** shows an example of modulus calculated from the experimental measurement of C₁₂DMPO in the concentration of 0.115 mol/m³. The surface area is controlled the sinusoidal waveform with an offset of 0.2 cm², an amplitude of 0.02 cm² and a period of 10s, as shown in Figure 4.4 (a). The red curve indicates the predefined sinusoidal waveform and the open circle shows the experimental response. The information of the amplitude, offset and the period (or frequency) can be directly obtained from the predefined theoretical curve. Parallel with surface area oscillations, surface tension is acquired in real-time, as plotted in Figure 4.4 (b). Comparing the smooth control of surface area, the surface tension scatters slightly, due to the sensitivity of surface tension measurement to the environmental disturbance, the quality of acquired image, and image processing artifacts.⁹¹ To extract the information from the surface tension results, a best fitting procedure using the sinusoidal function is conducted, as indicated by the blue dash line. From the best fitting, the amplitude of the surface tension is ready to obtain, reading 0.24 mN/m in this case. The phase angle can be calculated by comparing the sinusoidal curve from surface area and surface tension, as shown in Figure 4.4 (c). A phase lag of surface area can be observed, indicating the film is viscoelastic. The phase lag is 24° in this experiment.

To demonstrate the feasibility of our method, a broad range of moduli for C₁₂DMPO were measured. Eight concentrations ranging from 0.013 to 0.42 mol/m³ was selected with frequency ranging from 0.01 to 0.2 Hz, as shown in **Figure 4.5**. It can be found that the modulus we measured ranges from the lowest value around 1 mN/m to the highest around 30 mN/m. The

elastic modulus is found to be always higher than viscous modulus, indicating the film is largely elastic. This is consistent with the results found for the other low molecular-weight surfactants.^{26,}
⁹² To validate the accuracy of our measurement, literature values available at frequency of 0.08 Hz, and 0.01 Hz measured from bubble pressure method are also listed in the figure.²³ It can be found that our results are almost identical with literatures, indicating the validity of our measurement.

To characterize the surfactant film for a better interpretation of the experimental data, a theoretical analysis is carried out. Assuming the diffusion transfer from/to the bulk as unique relaxation process, the elastic and viscous modulus can be described by²⁰

$$E_r = E_0 \frac{1+\xi}{1+2\xi+2\xi^2} \quad (\text{Eq. 4.10})$$

$$E_i = E_0 \frac{\xi}{1+2\xi+2\xi^2} \quad (\text{Eq. 4.11})$$

with

$$\zeta = \sqrt{\frac{\Omega_D \tau}{4\pi}} \quad (\text{Eq. 4.12})$$

where E_0 is the limiting elasticity. Ω_D is the characteristic frequency of the diffusion exchange. E_0 and Ω_D can be given by the concentration c as follows

$$E_0 = \frac{d\Pi}{d \ln \Gamma} \quad (\text{Eq. 4.13})$$

$$\Omega_D = D \left(\frac{dc}{d\Gamma} \right)^2 \quad (\text{Eq. 4.14})$$

where Π is the surface pressure defined by $\Pi = \gamma_0 - \gamma$. γ_0 is the surface tension of the pure interface, measured of 72.5 mN/m for the pure buffer solution in our experiments. D is the

diffusion coefficient. Γ measures the adsorption of the surfactant which can be expressed by the average molar area of the surfactant (ω) and the surface coverage of the surfactant (θ), denoted by

$$\Gamma = \frac{\theta}{\omega} \quad (\text{Eq. 4.15})$$

To improve the quality of data interpretation, a two-dimensional relative surface layer compressibility coefficient (ε) is introduced recently.⁹³ The ω is assumed to depend on Π and θ , denoted by

$$\omega = \omega_0(1 - \varepsilon\Pi\theta) \quad (\text{Eq. 4.16})$$

where ω_0 is the molar area of the surfactant at zero pressure. To correlate Π and c , the Langmuir equation of state and the adsorption isotherm are used, defined by

$$\Pi = -\frac{RT}{\omega_0} \ln(1 - \theta) \quad (\text{Eq. 4.17})$$

$$bc = \frac{\theta}{1-\theta} \quad (\text{Eq. 4.18})$$

Combining Equations 4.12-4.18, the E_0 and Ω_D are given by

$$E_0 = \frac{d\Pi}{d\ln\Gamma} = \frac{\frac{d\Pi}{d\theta}}{\frac{d\ln\Gamma}{d\theta}} = \frac{RTbc}{\omega_0} \frac{\omega_0(1+bc) - \varepsilon RTbc \ln(1+bc)}{\omega_0(1+bc) + \varepsilon RT(bc)^2} = \frac{RT}{\omega_0} bc \frac{A_1}{A_2} \quad (\text{Eq. 4.19})$$

$$\begin{aligned} \Omega_D &= \frac{D}{2} \left(\frac{dc}{d\Gamma} \right)^2 = \frac{D}{2} \left(\frac{\frac{dc}{d\theta}}{\frac{d\Gamma}{d\theta}} \right)^2 = \frac{D}{2} \left[\frac{1+bc}{b} \frac{\{\omega_{s0}(1+bc) - \varepsilon RTbc \ln(1+bc)\}^2}{\omega_0(1+bc) + \varepsilon RT(bc)^2} \right]^2 \\ &= \frac{D}{2} \left[\omega_0 \frac{1+bc}{b} \frac{\{A_1\}^2}{A_2} \right]^2 \end{aligned} \quad (\text{Eq. 4.20})$$

where

$$A_1 = (1 + bc) - \varepsilon \frac{RT}{\omega_0} bc \ln(1 + bc)$$

$$A_2 = (1 + bc) + \varepsilon \frac{RT}{\omega_0} (bc)^2$$

Thus, the modulus vs. concentration curve is determined by the four parameters, which are ω_0 , b , ε , and D . Using these parameters as the fitting parameters, the best fit theoretical curve is obtained as shown in Figure 4.5. The solid curves are the best fit to the theoretical equations to the E_r and E_i , given the fitting parameters in the **Table 4.1**. It is found that the theoretical curve can accurately describe the experimental data, except for the data for viscous modulus when the frequency is low. The theoretical values are always higher than the corresponding experimental results for viscous modulus at low frequency. This could be caused by the inadequate consideration of the different relaxation processes in the theoretical model. The lower values of the experimental data indicate that the smaller energy dissipation occurs in the film when the frequency is small. The diffusion transfer of surfactant from/to the bulk, which is considered as the unique relaxation process, may not dominate in this frequency range. Further investigations are needed to update the theoretical model at lower frequency.

The reference values of the four parameters are also provided in the Table 4.1.²⁷ The parameters directly fitted from our experiment are in good agreement to the reference values. The parameters ω_0 , and b are also validated in the Langmuir equation of state and the adsorption isotherm, as shown in **Figure 4.6**. It can be found that, the theoretical curve can accurately describe the adsorption isotherm. It should be noted that the slight discrepancy between the experimental data and the theoretical data at the concentrations of 0.019 mol/m^3 and 0.22 mol/m^3 could be caused by the experimental errors in the measurement. To quantify the discrepancy

between the experimental data and the theoretical curve, the sum of squared residuals (SSR) is used, defined by

$$SSR = \sum_{i=1}^n (y_i - f(c_i))^2 \quad (\text{Eq. 4.21})$$

where y_i is the i^{th} value of the experimental results (surface pressure), c_i is the i^{th} value of concentrations, and $f(c_i)$ is the equation of adsorption isotherm. The SSR is calculated to be 3.92 (eliminating the two obvious outliers) for the data in Figure 4.6. The small value of SSR indicates the tight fit of the model to the experimental data, which also provides evidence that our experimental data is accurate and reliable.

The combination of the experimental data and the theoretical analysis provides a better understanding of the behavior of adsorbed layer responding to the harmonic oscillation. It can be found in Figure 4.5 that both elastic and viscous moduli feature a maximum with increasing concentration at each frequency. To explain this, the effect of the surface coverage Γ and the exchange of surfactant between bulk and surface on the modulus with increasing surfactant concentration should be considered. According to Equation 4.13, the Γ increases with increasing concentration, thus resulting in a higher modulus. However, the molecular exchange rate between bulk and surface also becomes higher with the increasing surfactant concentration. The fast exchange of surfactant at high concentrations evens the surface tension gradient immediately. The competitive effect of the increasing Γ and the increasing molecular exchange on $E_r(c)$ and $E_i(c)$ curves lead to a maximum of modulus at a certain concentration.

When considering the apex of the modulus with different frequencies, it can be found that this maximum slightly shifts towards lower concentration with the decreasing frequency for both elastic and viscous modulus. The frequency dependent maximum can be ascribed to the influence of the exchange rate of the surfactant between bulk and the surface on the surface

tension gradient. Higher oscillating (frequencies) requires a higher exchange rate of surfactant molecules to even the gradient of surface tension within one period, involving a higher concentration. Therefore, the higher the frequency, the higher the surfactant concentration required for the peak of modulus.

It should be noted that a discrepancy is found between the experimental data and the theoretical curve at the concentration $c=0.42 \text{ mol/m}^3$. The experimental data are significantly smaller than the predicted theoretical curve. Note that this concentration is close to the critical micelle concentration (CMC) of C_{12}DMPO (0.55 mol/m^3). This indicates the inadequacy of the theoretical model in predicting the modulus near the CMC as the effect of micelles on the adsorption is not considered in the current theoretical model.

4.3.3 Dilational modulus of proteins

To demonstrate the feasibility of our method in dynamic measurement during adsorption, the moduli of two proteins are measured along the adsorption process. The modulus of adsorbed layers was measured as a function of surface pressure from the very early stages of surface layer formation (near zero surface pressure) to the state where the surface layer is close to saturation (close to the maximum surface pressure). In this case, the whole succession of modulus change in the layer after adsorption at the initial moment can be observed.

Figure 4.7 summarizes the adsorptions of BSA and β -casein and the dynamic modulus measured during the adsorption. It should be noted that the protein involves a relative long period of adsorption process ranging from hours to days. The evaporation of the solvent should be considered in such a long adsorption period. In the present study, we used the closed-loop ADSA to maintain the constant surface area during the adsorption. **Figure 4.8** shows the change of the surface tension with surface tension kept constant during the adsorption of BSA.

The adsorption curve in Figure 4.7 (a) indicates that the adsorption of β -casein reaches to equilibrium after 30 minutes, while the surface pressure of BSA continues to increase even after 80 minutes. It can be found that the surface pressure experiences a sharp increase at the initial stages and then a delay in growth. The studies of adsorption kinetics indicate a different mechanism during the adsorption.⁹⁴ The fast increase of surface pressure is ascribed to the protein diffusion from the bulk phase to the surface. The following slow change of surface pressure approaching to the equilibrium is related to conformational transitions in the adsorption layer. However, the monotonic adsorption isotherm provides limited information about these transition processes.

To unveil detail information during the adsorption process, the dynamical modulus during the adsorption was measured. Figure 4.7 (b) shows the measured modulus ($|E|$) and the phase angle ($\tan \phi$) for BSA and β -casein as a function of surface pressure. It can be found that $|E|$ of BSA increases with increasing surface pressure to a maximum value at the surface pressure around 10 mN/m. Upon further increase of the surface pressure, the modulus remains constant or somewhat decreases. $|E|$ of β -casein increases when the surface pressure increases to 4 mN/m and then decreases slightly and then increases to another local maximum. Comparing the value of modulus, it can be found that the $|E|$ of BSA is twice larger than that of β -casein when surface pressure exceeds 6 mN/m. The phase shift ($\tan \phi$) remains small in the entire range of surface pressure. The $\tan \phi$ does not exceed 0.05 for BSA and 0.2 for β -casein, respectively, even in the region of the modulus at its local maximum. Different from the low molecular-weight surfactants, both the BSA and β -casein surface layers are proven to be essentially elastic. Literature values of the BSA and β -casein measured from oscillating barrier method^{21, 82} using a similar frequency are also provided in the figure. It can be found that $|E|$ of β -casein is in good

agreement with the literature values. Our method is sensitive enough to detect the two local maxima of the modulus during adsorption. This is concordant with the results reported in existing literatures.^{82, 95, 96} $|E|$ of BSA agrees well when surface pressure is in the range of 0-6 mN/m. When surface pressure increases beyond 6 mN/m, our measured results are 20% smaller than the literature values. Such discrepancy can be caused by the differences in source of the protein, pH and ionic strength used in the experiment.²¹

Though sharing similar adsorption isotherms, the dilational moduli of BSA and β -casein exhibit large differences. $|E|$ of BSA is always larger than that of β -casein, except at the early stage when only a small amount of BSA is adsorbed. To explain this, two aspects contributing to the dilational modulus during the adsorption, the intra-protein structure transformation and the aggregated inter-protein network strength, is considered.⁹⁷ At early stage, the adsorbed proteins remain as individuals. The modulus in this stage is assumed to arise from increasing adsorption at the surface, the mechanism of which is similar to that of low molecular-weight surfactant. Compared to the flexible protein β -casein, the rigid protein BSA is more effective in restoring the previous state of the interface, resulting in a faster increase of dilational modulus.⁹⁷ With increasing surface pressures, the conformational changes result in the development of an interconnected network, meanwhile the structural flexibility of the adsorbed proteins increases with the unfolding of structure. In this stage, the slowly development of the inter-protein network gives rise to the slow increase in $|E|$, while the loss of internal structural stiffness of the protein levels off the modulus.⁹⁷ These two effects results in the maximum of the dilational modulus, as observed for BSA and β -casein. However, it can be found that the conformation transient introduces a more complicated influence on the modulus of the flexible protein β -casein, resulting two local maxima at the modulus vs. surface pressure curve.

4.4 Summary

We have developed a waveform generator, integrated into the constrained drop surfactometer (CDS), for surface area oscillation in the study of dilational rheology. The waveform generator can accurately generate a sinusoidal waveform in surface area in a wide range of frequency up to 0.2 Hz. We have demonstrated the feasibility and advantages of the surface area waveform generator in two applications, including the measurement of modulus for low molecular-weight surfactant in a wide range of concentration and frequencies and the measurement of dynamic modulus change of two proteins during the adsorption. All these applications have demonstrated the accuracy, versatility, and applicability of this new ADSA-based waveform generating technique. Combined with the CDS, the waveform generator holds great promise for advancing the surface rheology study.

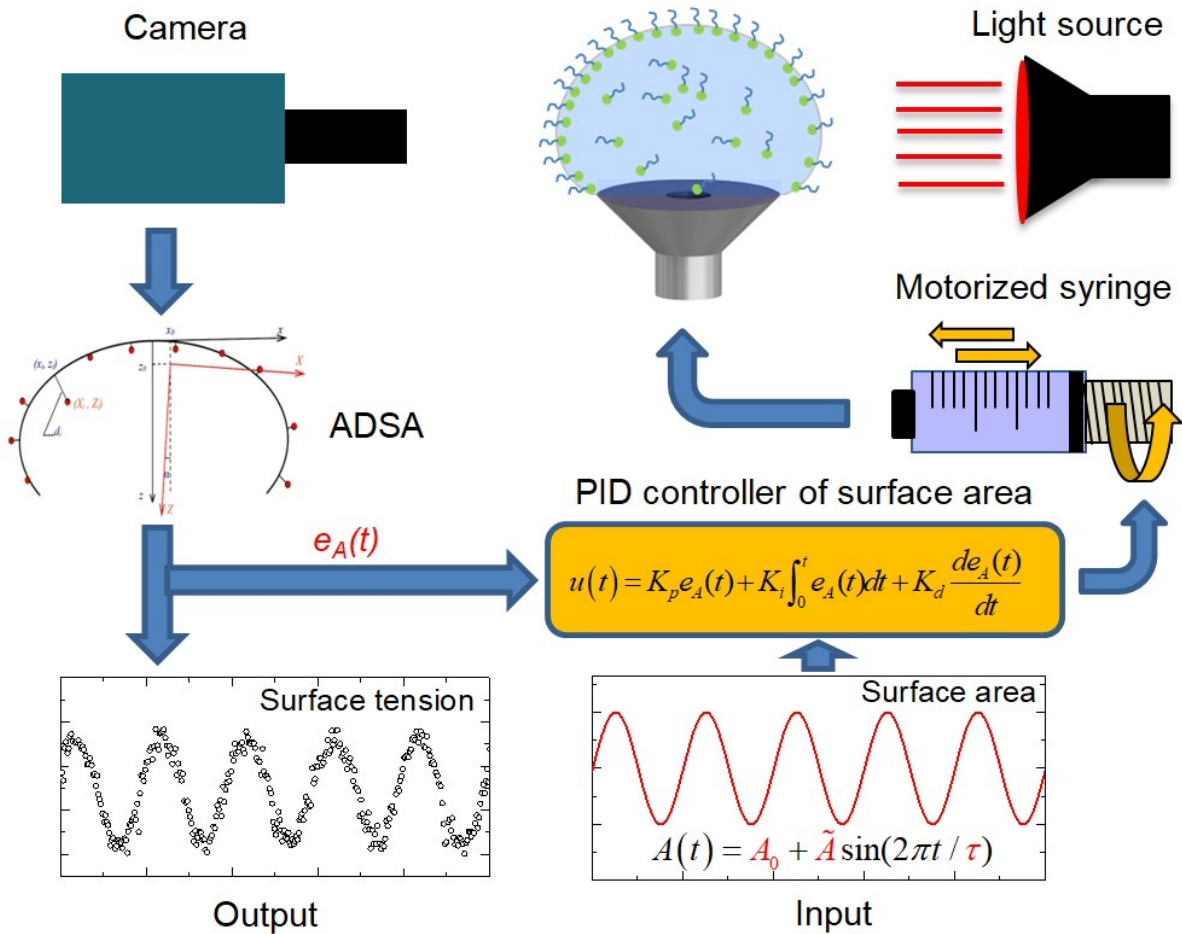


Figure 4.1 Schematic of the sinusoidal waveform generator using a closed-loop axisymmetric drop shape analysis (ADSA) feedback control system integrated into the constrained drop surfactometer (CDS). In the CDS, a liquid droplet is "constrained" on a 3 mm carefully machined pedestal with a knife-sharp edge. The droplet is continuously monitored by ADSA in real-time. Surface area is controlled to a sinusoidal waveform with the closed-loop ADSA. The resultant command signal controls a motorized syringe, consisting of a high-precision servomotor and a piston-syringe system, to actuate the droplet with surface area oscillating in sinusoidal waveform. Surface tension is the output for calculating the dilational modulus.

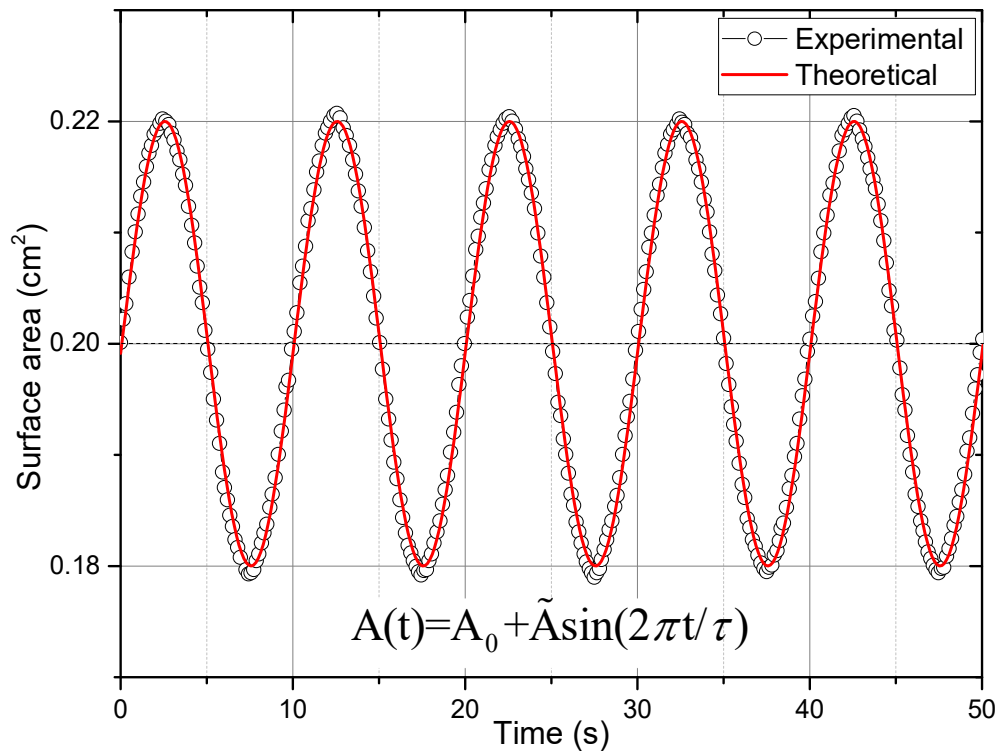


Figure 4.2 Demonstration of the waveform generator for oscillating the surface area (A) of a water droplet following the theoretical sinusoidal curve (Area offset $A_0 = 0.2 \text{ cm}^2$, Amplitude $\tilde{A} = 0.02 \text{ cm}^2$, Period $\tau = 10 \text{ s}$). It is clear that the change of surface area was controlled closely following the theoretic sinusoidal waveform.

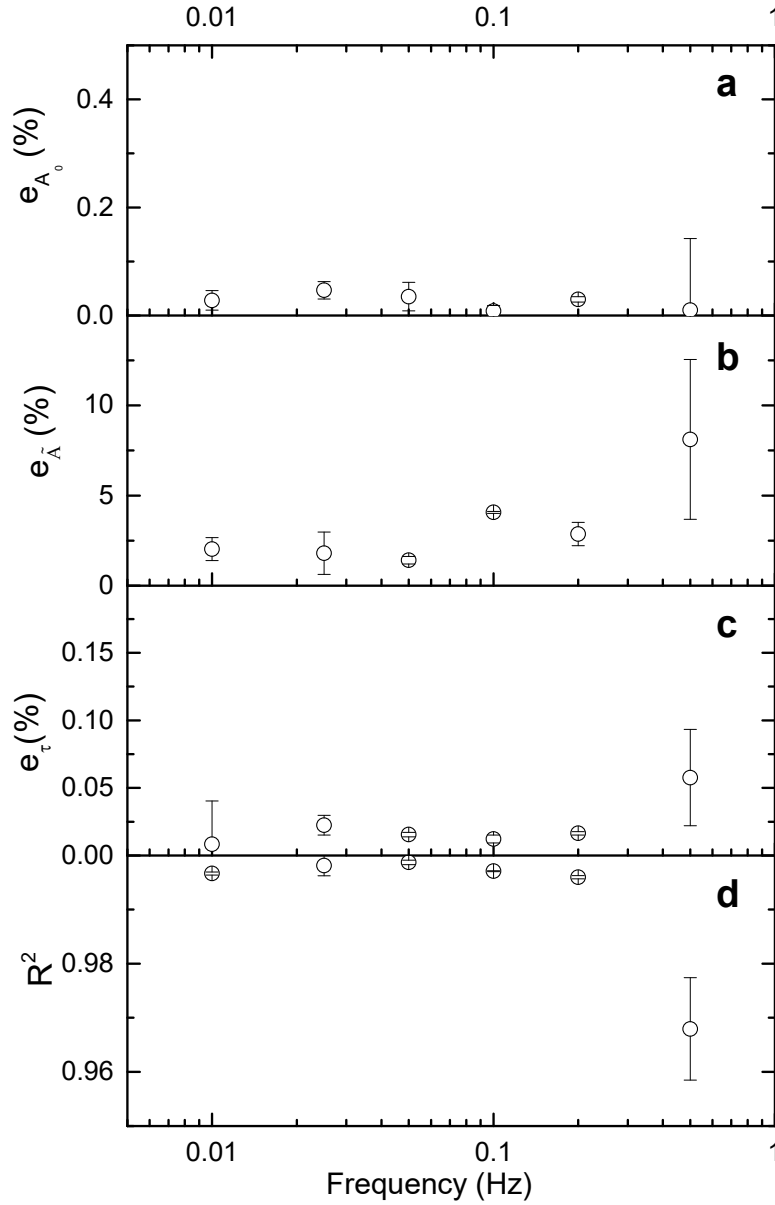


Figure 4.3 Relative errors ($\varepsilon = \frac{|A_{measured} - A_{theoretical}|}{A_{theoretical}}$) of area offset (ε_{A_0}), relative errors of amplitude ($\varepsilon_{\tilde{A}}$), relative errors of period (ε_{τ}) and R^2 as a function of frequency measured using the water droplet with the offset of 0.2 cm^2 and the amplitude of 0.02 cm^2 . It is clear that the relative errors of area offset, amplitude, and period stay small (*i.e.*, $\varepsilon_{A_0} < 0.5\%$, $\varepsilon_{\tilde{A}} < 5\%$, and $\varepsilon_{\tau} < 0.1\%$) and R^2 is larger than 0.99 for frequency from 0.01 Hz to 0.2 Hz. When frequency is increased to 0.5 Hz, the relative errors increase significantly with the $\varepsilon_{\Delta A}$ most sensitive to the frequency (increased to over 10%). The R^2 decreases to 0.96.

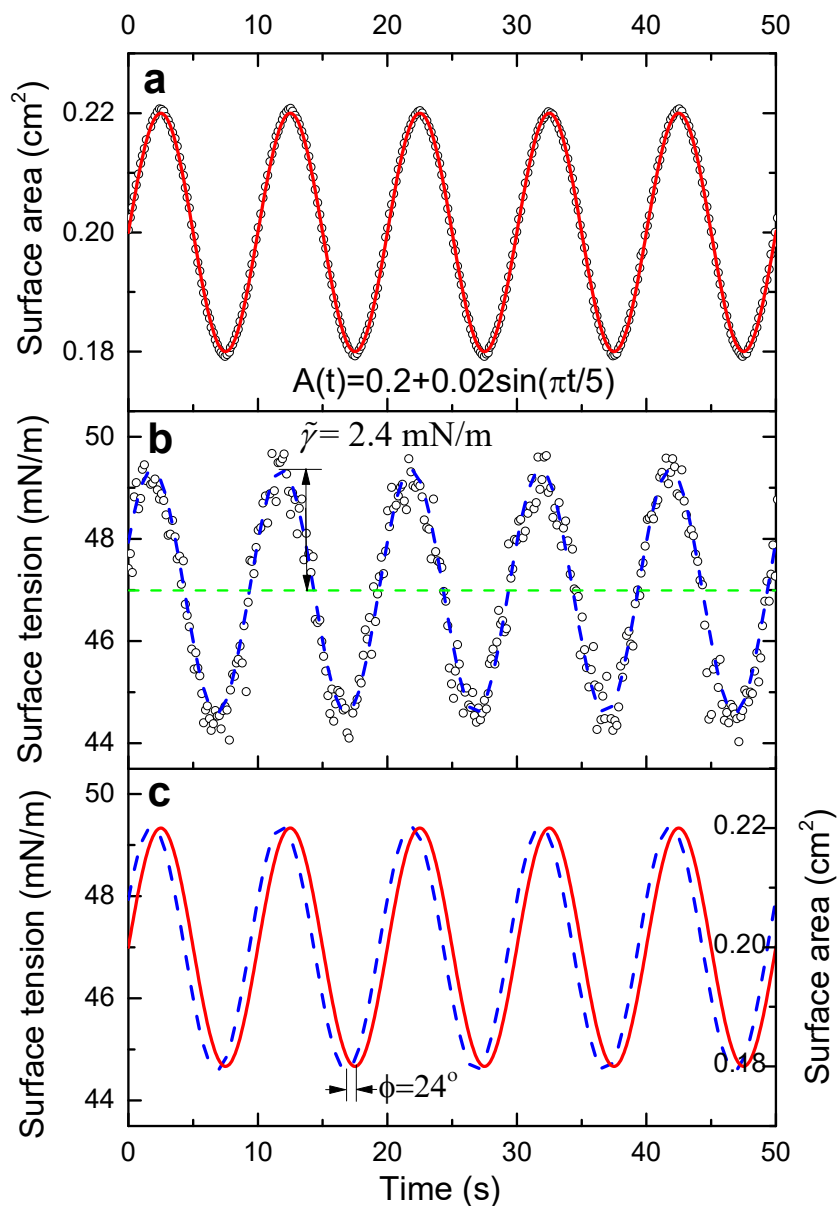


Figure 4.4 (a) Sinusoidal oscillations of the area of $C_{12}DMPO$ droplet with an offset of 0.2 cm^2 , an amplitude of 0.02 cm^2 , and a period of 10s. (b) Response of surface tension, and (c) Theoretical analysis of the surface area and surface tension. The dash blue curve is the best sine fitting of the surface tension and the red solid curve is obtained from the theoretical sinusoidal curve of surface area. It can be found that there exists phase lag of surface area, which is calculated to be 24° in this case. The amplitude of the surface tension can be read from the fitted sine curve.

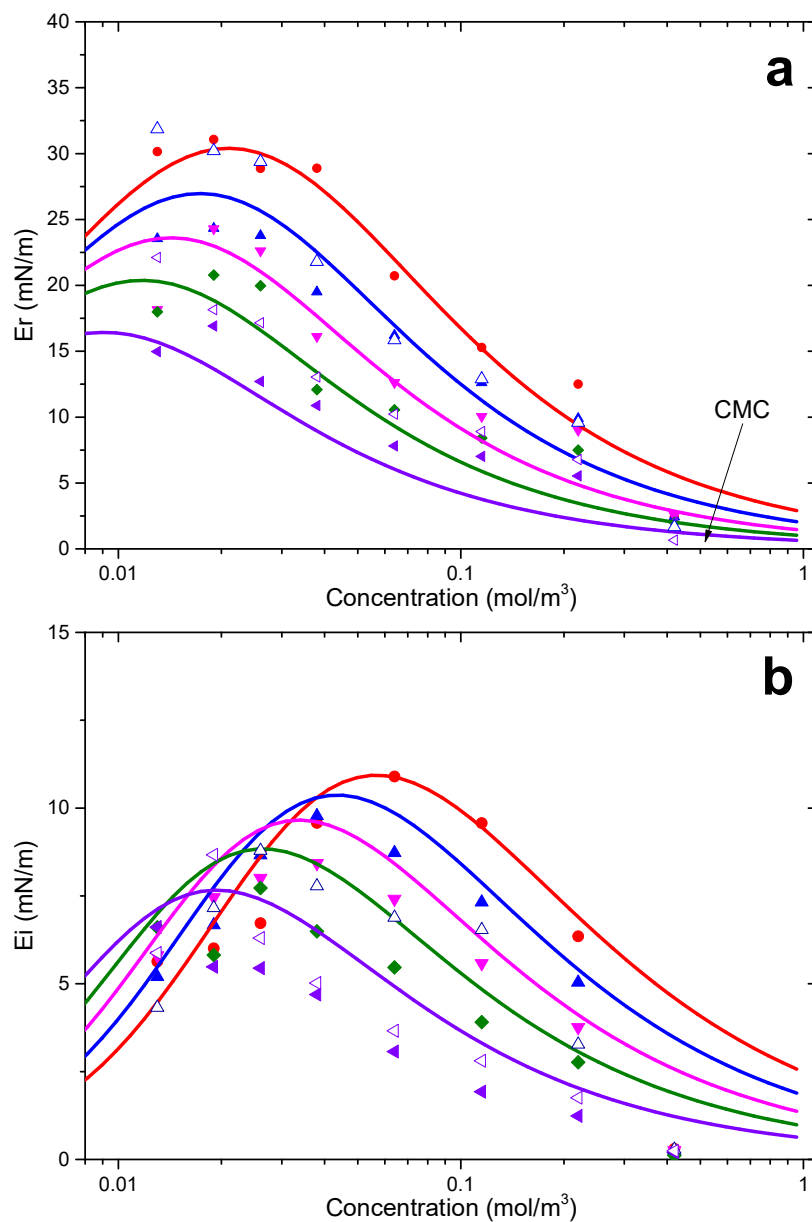


Figure 4.5 (a) Real and (b) imaginary parts of complex surface dilational modulus as a function of C₁₂DMPO concentration at oscillation frequency of (●) 0.2, (▲) 0.1, (▼) 0.05, (◆) 0.025, (◄) 0.01 Hz. The curves are theoretical fittings using the parameters in Table 4.1. Literature values at frequency of (△) 0.08 Hz and (◁) 0.01 Hz are also plotted in the figure. Both the elastic and viscous modulus features a maximum for a constant frequency. The maximum of dilational modulus shifts to lower concentration when the frequency reduces.

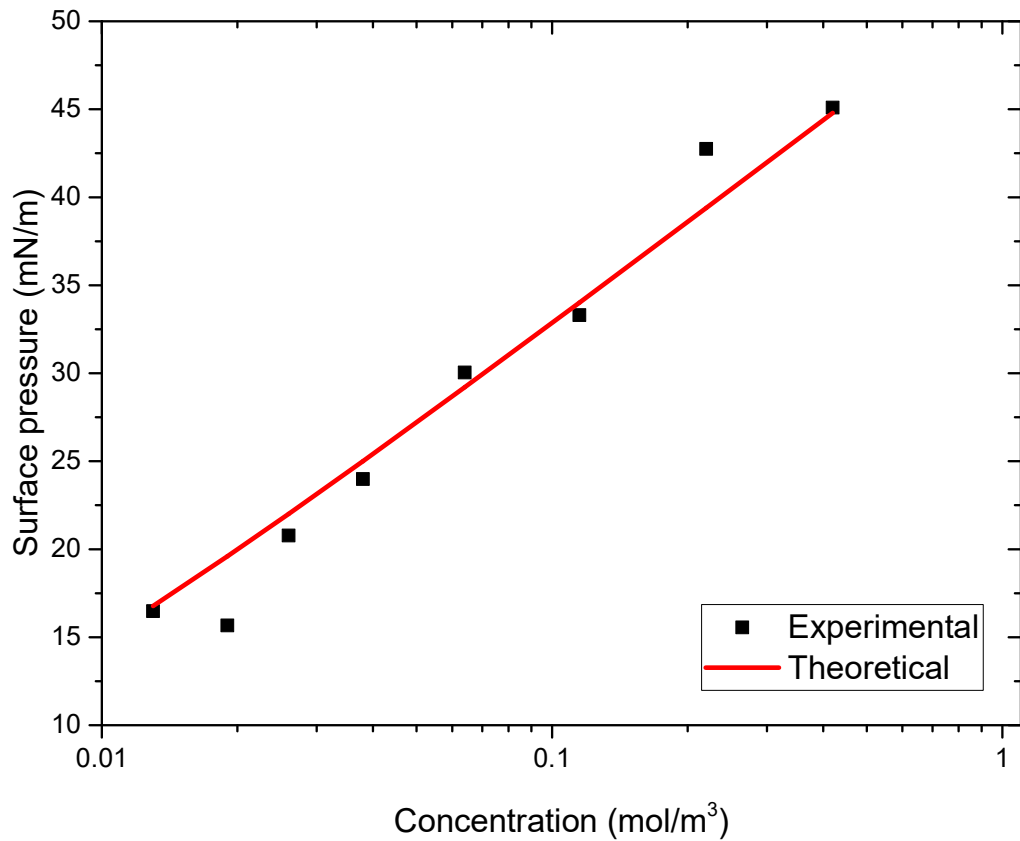


Figure 4.6 Adsorption isotherm of the surfactant $C_{12}DMPO$. The solid curve corresponds to the theoretical isotherm model. The parameters used in the theoretical model are presented in Table 4.1. It can be found that the theoretical isotherm using the parameters predicted by the surface rheology model can accurately describe the experimental data.

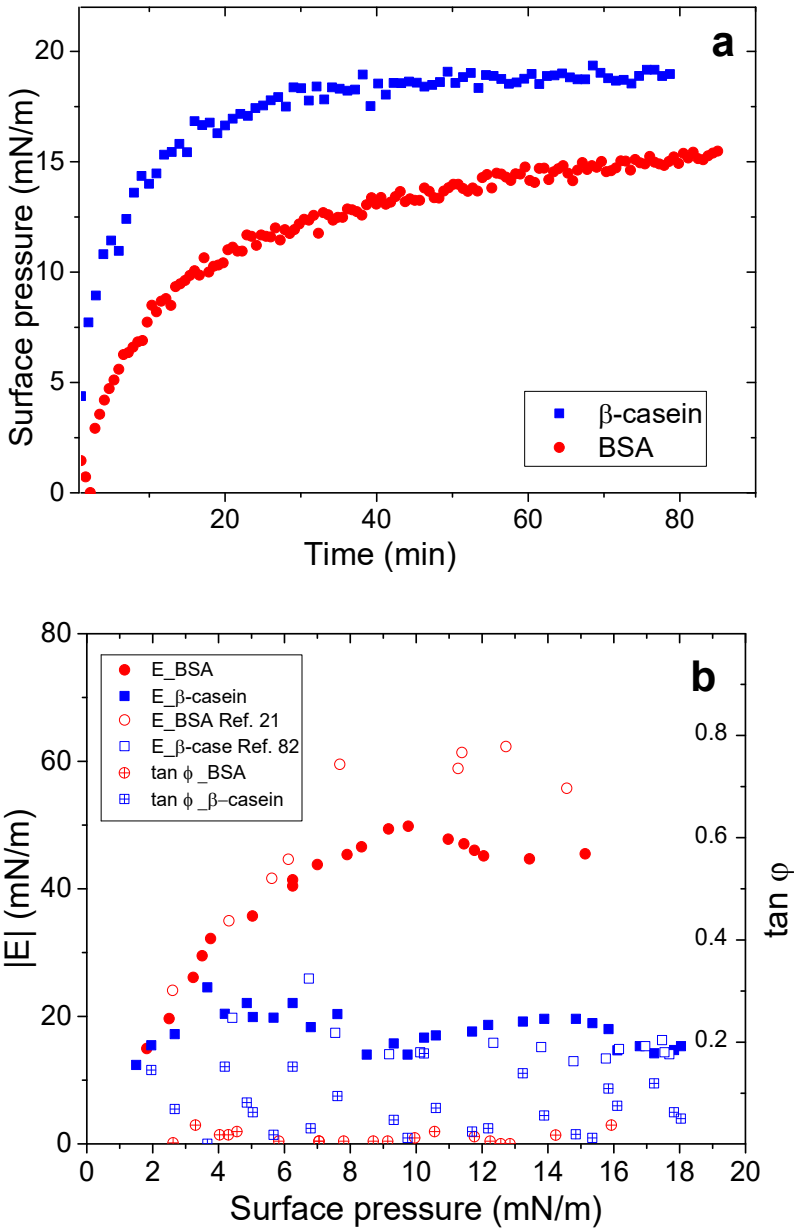


Figure 4.7 (a) Adsorption isotherm and (b) dynamic modulus and viscous phase angle vs. surface pressure for BSA and β -casein solutions at concentration of 10 mg/L and frequency of 0.1 Hz. Literature values of dynamic modulus of BSA and β -casein are also plotted in the Figure 4.7(b). The change of the modulus with the surface pressure indicates the co-influence of the intra-protein structure transform and the development of the inter-protein network on the surface rheology.

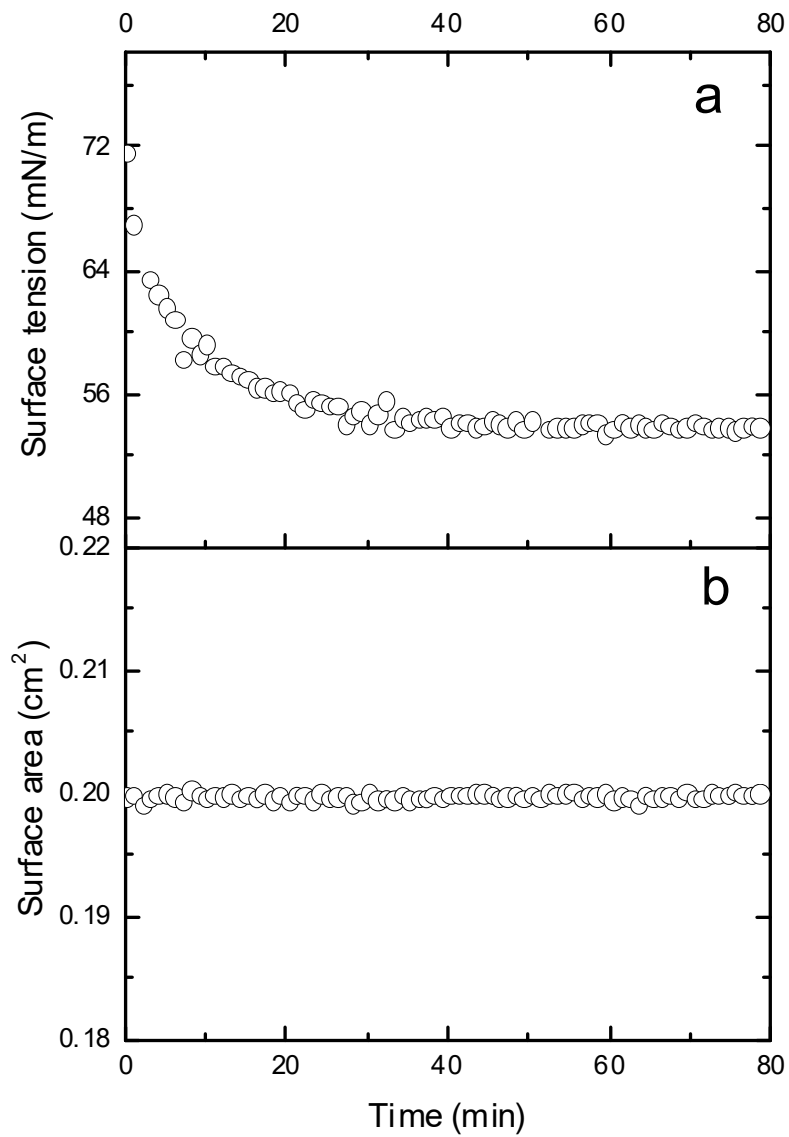


Figure 4.8 (a) Surface tension and (b) surface area as a function of time during adsorption of BSA using closed-loop ADSA to maintain the surface area at constant values.

Table 4.1 Fitting parameters for the adsorption isotherm and modulus of C₁₂DMPO obtained from fitted the data with the Model given by Equations 4.12-4.20. Literature values are list in the third column as a reference.

	Present	Ref. 83
$\omega_0(\text{m}^2/\text{mol})$	2.9×10^5	2.5×10^5
$b (\text{m}^3/\text{mol})$	4.9×10^2	1.9×10^2
$\varepsilon (\text{m}/\text{mN})$	1.0×10^{-2}	8.0×10^{-3}
$D (\text{m}^2/\text{s})$	3.2×10^{-10}	3.0×10^{-10}

Chapter 5. Other research involvements

In this chapter, we demonstrated the applications of the CDS in three researches done in my PhD period. In the first application, we used CDS to measure surface tension of scarce samples, i.e., surfactant of xylem sap residue. In the second application, we developed a subphase replacement system in CDS to study the multilayers formed by the pulmonary surfactant. In the third application, we used CDS to study the phospholipid self-assembly at oil-water interfaces.

5.1 Determining the surface tension of xylem surfactants

5.1.1 Introduction

The purpose of this research is to determine the surfactant properties of xylem sap residue. Vascular plants transport large quantities of water under negative pressure without constantly creating gas bubbles that would disable the systems. Attempts to replicate this feat in artificial systems have invariably resulted in rapid bubble formation, except under highly controlled and extremely simplified conditions, using pure water at mild pressure, with only hydrophilic surfaces present. The hydraulic system of vascular plants, the xylem, in contrast, is complex, with millions of conduits, potentially containing hydrophobic surfaces, dissolved gas-saturation or supersaturation, and surface active molecules that can lower surface tension, all of which factors increase the chances of bubble nucleation.^{98, 99} In this research, we try to explain how plants transport water under negative pressure. We hypothesized that xylem surfactants enable water transport under negative pressure by coating hydrophobic surfaces and nanobubbles, thereby keeping them below the critical size at which bubbles would expand to form embolisms.

¹⁰⁰ A hypothesized model for nanobubble formation in pit membranes is illustrated in **Figure 5.1**. A meniscus invading a pit membrane pores under a pressure gradient would almost certainly be coated by the lipid surfactants clogging the pores. Surface tension in a confined pore space clogged with surfactant micelles would be very low, and tight constrictions in the fibrous pore space would cause bubbles to snap off inside the pore. In this case, the lipid-based surfactants are a universal requirement for water transport under negative pressure.

However, determining the surfactant properties of xylem sap is not a trivial task. As the amount of surfactant existing in the xylem sap is tiny, the traditional technique, like Langmuir trough, is unable to handle such scarce sample. Using a small drop with volume around 10 μL in CDS, we are able to measure samples with volume less than 10 μL , using a spread technique. In this research, surfactants of xylem sap from two species *Geijera parviflora* and *Distictis buccinatoria*, were measured using CDS. The isotherms of the surfactant were compared. This research indicates the feasibility and reliability of the CDS in measuring scarce samples.

5.1.2 Materials and methods

Study species were selected as *Geijera parviflora* (evergreen tree, Rutaceae, Sapindales, malvids clade), and *Distictis buccinatoria* (DC.) Both of the species of the trees grew in the Fullerton Arboretum or on the California State University Fullerton campus in Fullerton, California, USA.

The dynamic surface tension of xylem sap was determined with the CDS. Ten milliliter of xylem sap was extracted from both *Distictis buccinatoria* and *Geijera parviflora* via the vacuum extraction method. Ten 1 mL of cell contamination controls were also collected from freshly cleaned xylem surfaces from the same stems and combined into a 10 mL sample. Sap and controls were lyophilized to obtain residues, including any surfactants in 1.5 mL Eppendorf

tubes. The residue samples were then dissolved in 10 μL of Millipore water, including cell contamination controls, and any residue clinging to walls was scraped off. The sample was then subjected to 2 minutes of ultrasonic treatment for mixing, and another 1 minute of ultrasonic treatment immediately before every measurement in the CDS.

To use the CDS for lyophilized xylem sap residue, a pure water droplet of $\sim 10 \mu\text{L}$ was formed on the CDS drop holder. A xylem sap residue sample of $\sim 1 \mu\text{L}$ was spread at the drop surface and allowed 5 min to reach equilibrium. Subsequently, the surfactant film was compressed at a rate of $\sim 20\%$ relative-area-per-second to concentrate the surfactant molecules at the drop surface. All measurements were conducted at room temperature of $20 \pm 1^\circ\text{C}$.

5.1.3 Results and discussion

Xylem surfactants were concentrated by lyophilizing sap from *Distictis buccinatoria* and *Geijera parviflora*, and their dynamic surface activity was determined via CDS. **Figure 5.2** shows the surface tension of xylem sap residue and cell contamination control residue of *Geijera parviflora* and *Distictis buccinatoria* as a function of drop surface area relative to the initial drop size. Both possessed strong surface activity that reached surface tension values below 5 mN/m when the adsorbed xylem surfactant films were contracted, similar to the behavior of pulmonary surfactants, which also consist of amphiphilic lipids and proteins.¹⁰¹ Lyophilized cell contamination residue in control samples did not show this surface tension-reducing capacity, except for a very weak effect at maximum surface contraction.

It can be found that the lipid-based surfactants clearly occur in angiosperm xylem. The lipid nature of xylem surfactants, from measurements of the area-dependent surface tension curves, indicates the high similarity to those found in pulmonary surfactants. The composition of both may be similar, with phospholipids as the main components and proteins possibly playing a role

in structuring the surfactant layers. Both of these very different systems would represent adaptations for gas-liquid interfaces operating under widely fluctuating pressure conditions that require variable surface tension for optimal function. The results from our CDS measurement indicates that the lipid-based insoluble surfactants act very differently from the commonly thought effect of the soluble surfactant in the xylem. This is because their micelles concentrate in pit membrane pores and their surface tension is variable and area dependent. The underlying mechanism for area-dependent surface tension is that insoluble surfactants (the so-called Langmuir film) are able to pack at the surface without collapse upon film compression. In contrast, soluble surfactant films (the so-called Gibbs film) usually collapse instantly upon compression. Though our CDS provided evidence for variable surface activity of xylem sap residue, the experimental behavior of concentrated xylem surfactants on small contracting and expanding droplets may differ from their behavior on gas-liquid nanointerfaces in xylem under negative pressure. Other techniques are under investigation in combination of CDS to unveil what the actual surface tension may be in functioning xylem.

5.2 Development of the subphase replacement technique

5.2.1 Introduction

Pulmonary surfactant (PS) coats a thin film at the air-water interface of the alveolar surface. The key function of PS is to reduce the work of breathing and to avoid alveolar collapse during expiration by reducing the surface tension of the alveolar surface.¹³ PS is composed of approximately 90% lipids and 10% proteins by weight.^{102, 103} Most of the lipids consist of phospholipids (PL, ~90-95 wt.%) with a small portion of neutral lipids (~5-10 wt.%), mainly cholesterol. Deficiency or dysfunction of PS causes severe respiratory diseases, among which respiratory distress syndrome (RDS) due to prematurity is the major disease of PS deficiency

worldwide.¹⁰⁴ Around 10% of all premature infants in developed countries are affected by RDS.¹⁰⁵ As a standard treatment to patients with RDS, exogenous surfactant replacement therapy has significantly reduced the infant mortality rate. Such clinical applications of PS entail the *in vitro* assessment of its biophysical properties, especially their structure-related function.

Traditionally, the direct visualization of film structures has been accomplished by Langmuir-Blodgett (LB) transfer technique in Langmuir trough. The transferred film was subsequently analyzed using microscopes, such as atomic force microscopy (AFM). However, the Langmuir trough is unable to fully mimic the intra-alveolar environment needed for simulating PS function in the lungs. The relative large size (usually $> 100 \text{ cm}^2$ in surface area) makes the device tremendous difficult to establish a unified temperature close to the surface, introducing artifacts in the measurements. More importantly, due to the large surface area, only spread film can be investigated in the LB trough, while the film in alveolar is subjected to the adsorption at the air-liquid surface from the aqueous.

Here we developed a novel method which enables us to directly visualize the lateral structure and molecular organization of natural pulmonary surfactant films after de novo adsorption. The droplet formation and oscillation was accomplished in the CDS with temperature rigorously controlled (i.e., 37 °C). A subphase replace system was developed to facilitate the liquid exchange in the droplet. It enables the subphase replaced by fresh buffer without disturbing the film at the surface. A miniaturized LB transfer system was developed to deposit the film. Using the CDS, we were able to better establish physiologically relevant conditions *in vitro* and provide additional insight on the composition-dependent nature of the surfactant biophysical properties.

5.2.2 Materials and methods

The PS used in this study was Infasurf (Calfactant), which was a gift from ONY Inc. (Amherst, MA). Infasurf was purified from whole-lung broncho-pulmonary lavage of newborn calves. Through an extraction process, Infasurf retained all of the hydrophobic components of bovine endogenous surfactant including phospholipids, cholesterol, and most hydrophobic surfactant proteins (SP-B and SP-C).^{57, 101} Infasurf has a total phospholipid concentration of 35 mg/mL and is stored frozen in sterilized vials. On the day of experiments, it was thawed and diluted to a phospholipid concentration of 1 mg/mL with a saline buffer of 0.9% NaCl, 1.5 mM CaCl₂, and 2.5 mM HEPES, adjusted to pH 7.0.

To facilitate the liquid exchange inside the drop, a double capillary holder has been developed in the CDS. It allows exchanging the subphase of the drop without disturbing the surface film and preserving the drop volume throughout the subphase exchange. Schematics of the CDS set-up with subphase replacement and LB transfer system under development is illustrated in **Figure 5.3**. The subphase replacement system includes a needle concentrically placed in a specially designed pedestal (with cone at the top) to facilitate subphase exchange with secondary liquid. The capillary needle is connected to a separate programmable motorized syringe. Details of the design are as the following. The fluid is delivered from inner needle (outer diameter of 0.82 mm and inner diameter of 0.51 mm) to the sessile drop on the top of the pedestal (outer diameter of 5 mm). The fluid is withdrawn from the pedestal through the annular space (inner diameter of 0.82 mm and outer diameter of 1.5 mm) between needle and the center hole of pedestal. Two servo motors work simultaneously to facilitate exchange of the fluid with the volume of drop unchanged during the replacement. In practice, the volume replacement should be performed slowly to avoid film disturbance.

For film visualization, a drop of PS was deposited on the pedestal in CDS, allowing the surfactant adsorbed to the surface. When the surface reaches its equilibrium, the vesicles were washed out using the subphase replace system. The surfactant films were then transferred to the surface of freshly cleaved mica using the LB technique. These films at constant surface tension were deposited onto the mica surface by elevating the previously submerged mica vertically through the air-water interface at a rate of 1mm/min. Topographical images were obtained using an Innova AFM (Bruker, Santa Barbara, CA). Samples were scanned in air in tapping mode with a silicon nitride cantilever with a spring constant of 0.12 N/m and a tip radius of 2 nm. Lateral structures were analyzed using Nanoscope Analysis (version 1.5).

5.2.3 Results and discussion

We first confirmed that the vesicles inside the subphase were fully washed out. A drop of 30 μL Infasurf solution was deposited on a 5-mm pedestal. A series of experiments were conducted with the subphase being replaced by once, twice, and three times of the original volume. For each experiment, 10 μL liquid was taken from the subphase using a 50 μL syringe and deposited on another 3-mm pedestal to check whether there were surface active components remaining in the subphase. **Figure 5.4** shows the surface tension vs. time for the original Infasurf droplet and the drop taken from different ratios of subphase replacement. It can be found that, after twice of the subphase replacement, the subphase is absent of surface active components, with the surface tension keeping steady after a certain time duration. This is close to the ratio done on pendant drop in literatures, indicating that three times of the original volume guarantees a complete subphase exchange.⁵⁰

To confirm that the film was not disturbed during the subphase replacement, we continuously monitored the surface properties of the drop (i.e., surface tension, surface area, and drop volume)

in the subphase procedure. **Figure 5.5** demonstrates the change of properties of the drop during subphase replacement and the dynamic cycling before and after subphase replacement. Surface tension, surface area, and drop volume were continuously monitored during the subphase replacement. It can be found surface tension, surface area, and drop volume were consistent during the subphase replacement. Integrity of the *de novo* adsorbed surfactant film after subphase replacement was examined by comparing the compression-expansion isotherms before and after the subphase replacement, as shown in Figure 5.5 (d).

Figure 5.6 shows the AFM topographic image of Infasurf film at 37 °C. The 3-D images shows uniform multilayer protrusions of <20 nm, which is in good agreement with the microstructure of the spread Infasurf film around the equilibrium spreading pressure.⁵⁷ A detail analysis of the structure indicate that most of the multilayers are around 5-6 nm in height (approximately 1-2 bilayers thickness). The formation of multilayers facilitates the film to reach low surface tension.

5.3 Phospholipid self-assembly at oil-water interfaces

5.3.1 Introduction

Phospholipids, as one of the major structural components in structuring and stabilizing biological interfaces as well as a well-defined model system for studying surface thermodynamics, thin-film materials, and colloidal soft matter, has received a lot of interest.^{106,}

¹⁰⁷ Though a lot of studies of phospholipids at the air-water surface have been carried out, very limited information is available about the structure and dynamics of the phospholipid film at liquid-liquid interface due to the complexity and difficulty to access experimentally. Taking advantage of the capability of CDS in interfacial tension measurement of oil-water interface, we characterized the isotherms of an important phospholipid, Dipalmitoyl phosphatidylcholine

(DPPC), at three different oil-water interfaces. The miniaturized LB transfer system aforementioned was used to deposit the film along the isotherm to investigate the structure change when compressing the film. The deposited film was examined by atomic force microscopy (AFM) to analyze the lateral structures.

5.3.2 Materials and methods

DPPC was purchased from Avanti Polar Lipids (Alabaster, AL) and used without further purification. DPPC was dissolved in chloroform to form a 1 mg/mL stock solution. The water used was Milli-Q ultrapure water (Millipore, Billerica, MA) with a resistivity greater than 18 M Ω ·cm at room temperature. Heptane, decane, and hexadecane were purchased from Fisher scientific. Heptane and decane were used without further purification. Hexadecane was purified with aluminum columns prior to experiments to remove surface active impurities.

The experiment was performed in CDS, the schematic of which is shown in **Figure 5.7**. A sessile drop of pure water was formed on the top of pedestal inside the oil. A special designed cuvette serves as the reservoir of the oil, from which the light can get through. The DPPC monolayer was spread onto the oil-water interface using a microsyringe. The droplet was then slowly expanded to increase surface tension until the corresponding surface pressure was reduced to ~ 5 mN/m. The droplet was left undisturbed for an additional 1 min for chloroform leaving the interface. The spread DPPC monolayer was subsequently compressed at a quasi-equilibrium rate of 0.05 cm²/min. The surface pressure and surface area were analyzed with ADSA in real-time.

LB transfer from the droplet was implemented by lifting a small piece of freshly peeled mica sheet at a speed of 1 mm/min. Topographical images were obtained using an Innova AFM (Bruker, Santa Barbara, CA). Samples were scanned in air in contact mode with a silicon nitride

cantilever of a spring constant of 0.12 N/m and a tip radius of 2 nm. Lateral structures were analyzed using Nanoscope Analysis (version 1.5).

5.3.3 Results and discussion

We first demonstrated that the chloroform exerted limited influence on the isotherm. The difference between air-water and oil-water experiments comes in the fact that the solvent can evaporate in the air while there is no chance for the solvent to evaporate in oil. Instead, the chloroform will settle down to the bottom of the cuvette because of the higher density of chloroform compared to the oil we used. To verify that the remaining of chloroform in the oil has no influence on the isotherm, we recorded the surface tension as a function of surface area for pure water-decane interface, the chloroform spread interface, and the DPPC spread interface upon compressing. The isotherms for the three systems can be found in **Figure 5.8**. The surface tension vs. relative surface area are identical between the pure water-decane interface and the chloroform spread interface, indicating the chloroform places no influence on the isotherm. The deviations of the results when the surface area (drop volume) is small come from the inaccurate calculation of ADSA. The discussion of the accuracy of ADSA upon reducing the drop volume can be found in Chapter 2.

We then compared the isotherm of DPPC at three different interfaces, i.e., heptane-water interface, decane-water interface, and hexdecane-water interface, as shown in **Figure 5.9**. With leakage-proof environment, CDS produces complete compression isotherms from near-zero to the collapse pressure. Similar to the isotherms in the air-water experiments, a clear liquid-expanded (LE) to tilted-condensed (TC) phase transition plateau was found. The surface pressure at which phase transitions occur rises with decreasing the length of carbon chain. The length of the phase transition plateau, which indicates the change of molecular area across the main

transition, reduces with decreasing the length of carbon chain. This is similar to the change of phase transitions upon reducing temperature.¹⁰⁷ Surface pressure (π_{tr}) at which phase transitions occur at the oil-water interface can be determined from the isothermal film compressibility:

$$\kappa = -\frac{1}{A} \left(\frac{\partial A}{\partial \pi} \right) \quad (\text{Eq. 5.1})$$

As shown in **Figure 5.10**, the surface pressure for phase transition is indicated by a peak in the isothermal film compressibility. At low surface pressure (i.e., $\pi < \pi_{tr}$), the DPPC monolayer is in a single disordered LE phase that features a relative high film compressibility. At high surface pressure (i.e., $\pi > \pi_{tr}$) The DPPC monolayer is in a single ordered TC phase that features a low compressibility (i.e., less than 0.05 (mN/m)^{-1}). This is in line with the results published for DPPC at air-water interface.¹⁰⁷ Inset of Figure 5.10 shows π_{tr} as a function of chain length of the oil. A linear relation can be found between π_{tr} and the carbon chain length of the oil. It can be found that the type of the oil can influence the flexibility of the molecules, similar to the effect of temperature on the DPPC isotherm.¹⁰⁷

To gain a structural understanding of the phase transitions, **Figure 5.11** shows the AFM topographic images of the DPPC monolayers at $\pi=10, 20, 30, 42 \text{ mN/m}$ for decane-water interface. It can be found that there is single phase at low surface pressure. When surface pressure increases, small domains (size less than $2 \mu\text{m}$) occurs. The domains start to compact with increasing the surface pressure. After phase transitions, the small domains compacted to single phase, indicating a small compressibility.

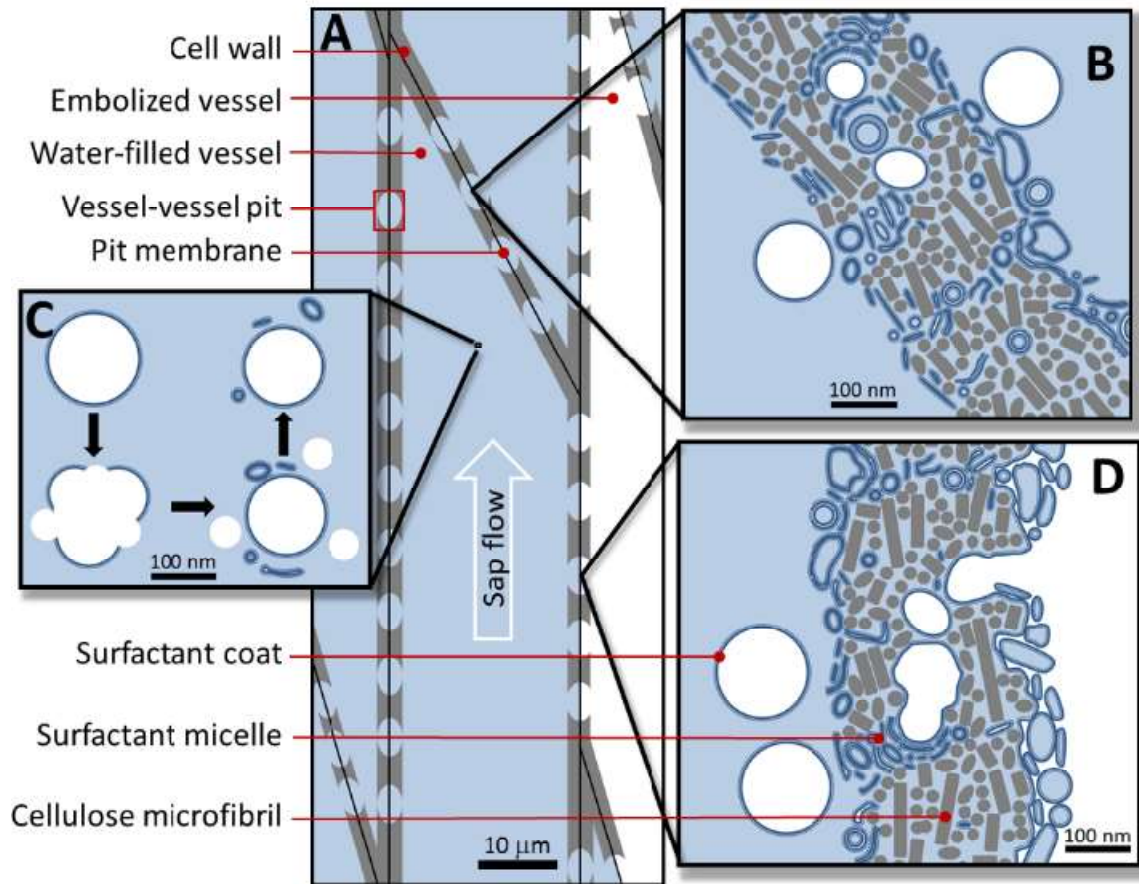


Figure 5.1 Visual model of the predicted dynamics of surfactant-coated nanobubbles in xylem. (A) Functional, sap-filled vessels (left, sap in light blue) bordering an embolized, air-filled vessel (right, air in white). (B) Surfactant-coated nanobubbles and micelles accumulating on and in a pit membrane between two functional vessels. (C) Hypothetical scenario for surfactant-coated nanobubble fragmenting under declining xylem pressure, thereby producing smaller coated nanobubbles, surfactant micelles, and much smaller, uncoated air bubbles with higher surface tension, which soon dissolve. (D) Air bubbles passing from embolized into sap-filled vessels through a large surfactant-filled nanopore in a vessel-vessel pit membrane, following the pressure gradient across the membrane. (Image courtesy of Dr. Jochen Schenk, California State University Fullerton.)

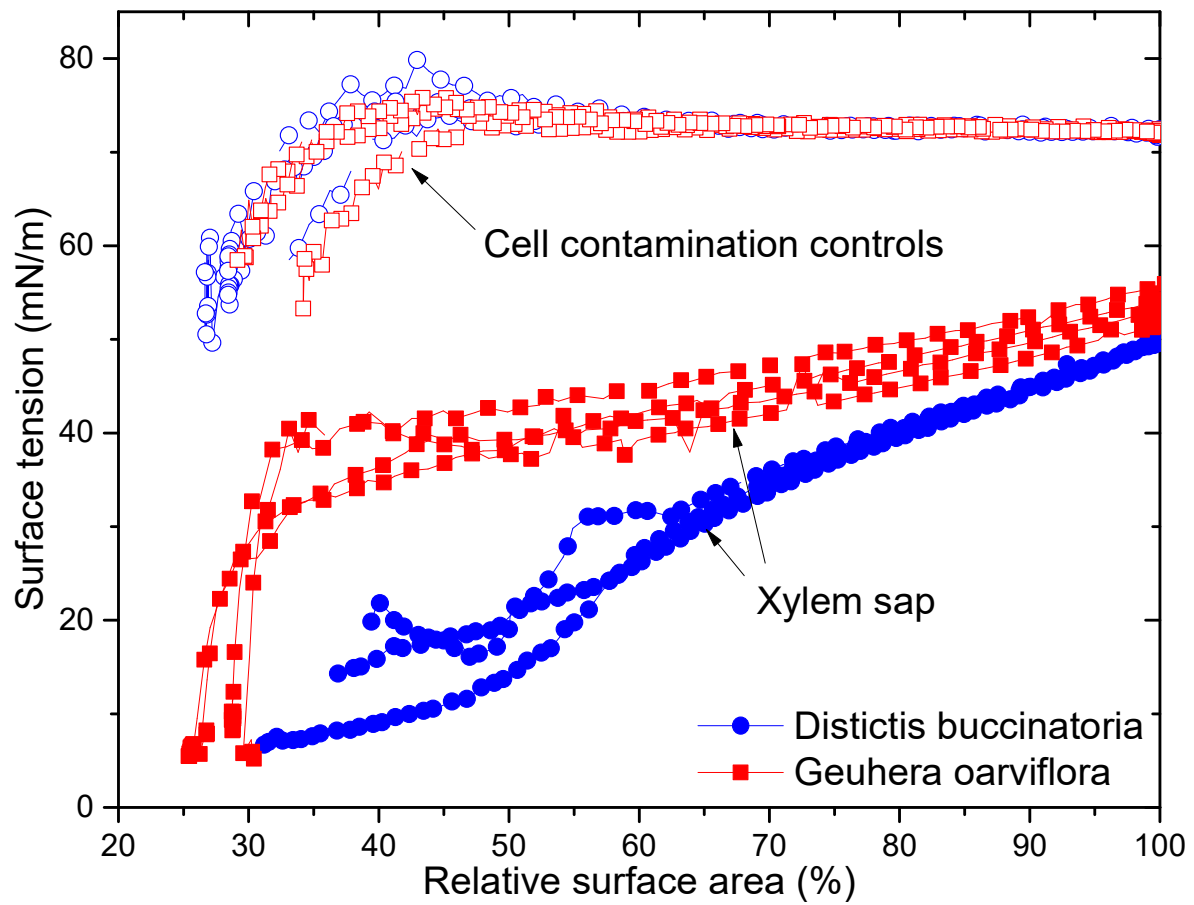


Figure 5.2 Surface tension of xylem sap residue and cell contamination control residue of *Geijera parviflora* and *Distictis buccinatoria* measured with CDS as a function of surface area relative to the initial drop size.

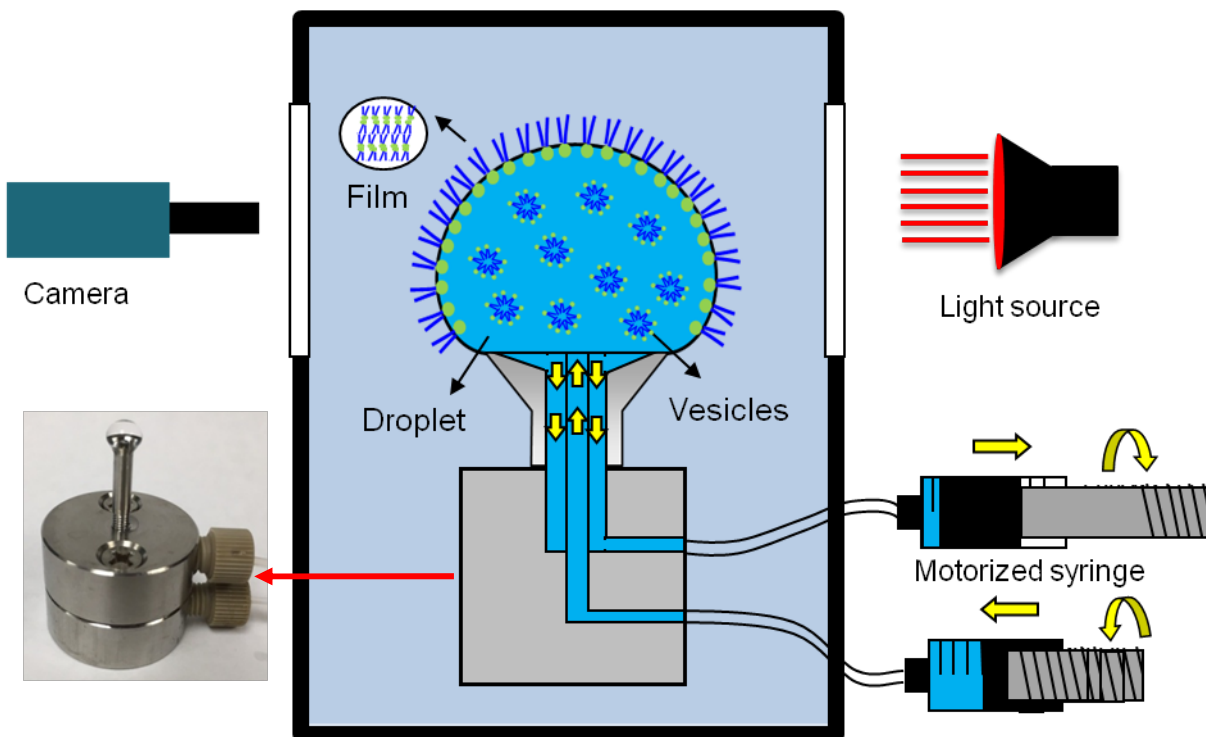


Figure 5.3 Schematic of the CDS set-up with subphase replacement. A liquid droplet was "constrained" on a 5 mm carefully machined pedestal with a knife-sharp edge, which is placed in an environmental control chamber with rigorous control of experimental conditions. The surface tension and other properties of the droplet are determined photographically from the shape of the droplet using ADSA. The liquid in the droplet can be replaced using a subphase replacement system with simultaneously injecting and withdrawing liquid by two motorized syringes.

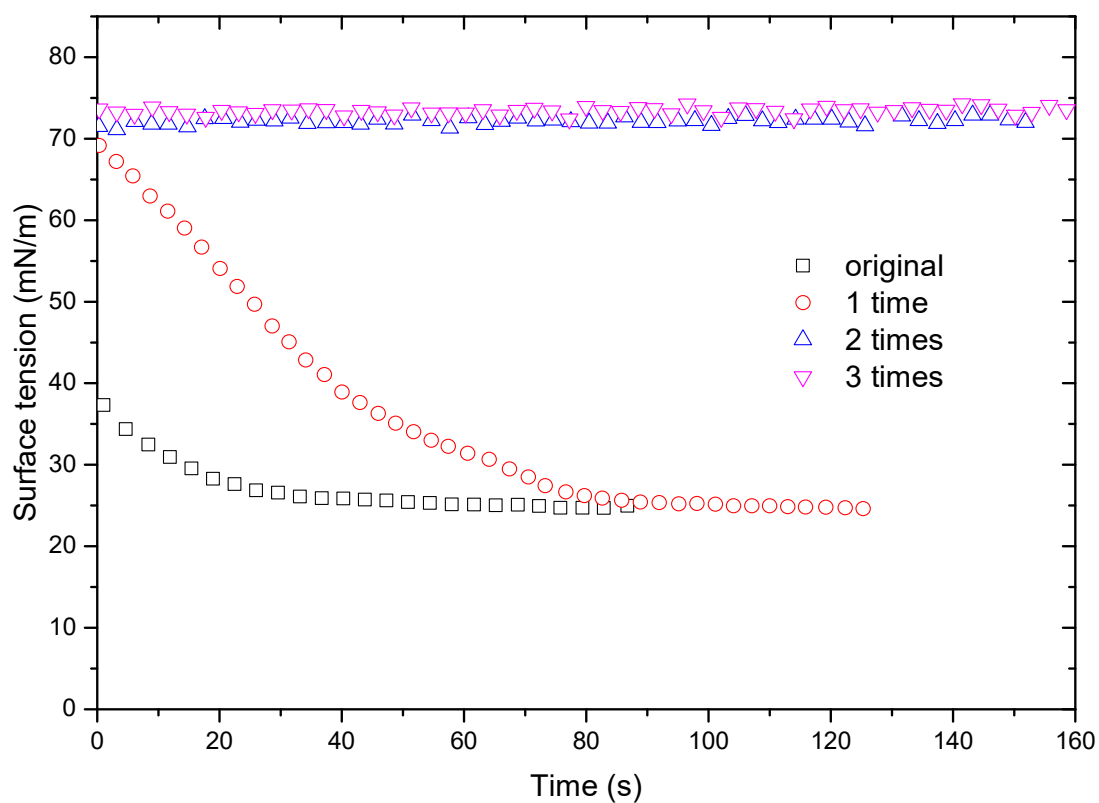


Figure 5.4 Surface activity check of the subphase after subphase replacement with once, twice, and three times of the original volume.

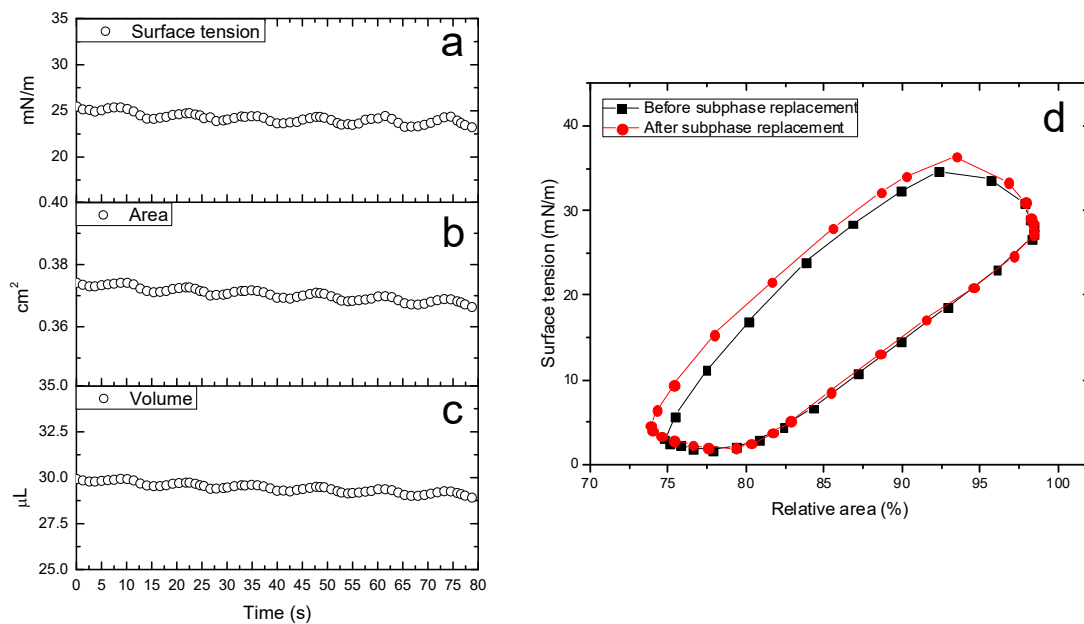


Figure 5.5 (a) Surface tension, (b) surface area, and (c) drop volume vs. Time during subphase replacement for the drop of Infasurf. (d) Subphase replaced Infasurf droplet biophysics showing no distinctive difference from *de novo* adsorbed film with vesicles in the subphase.

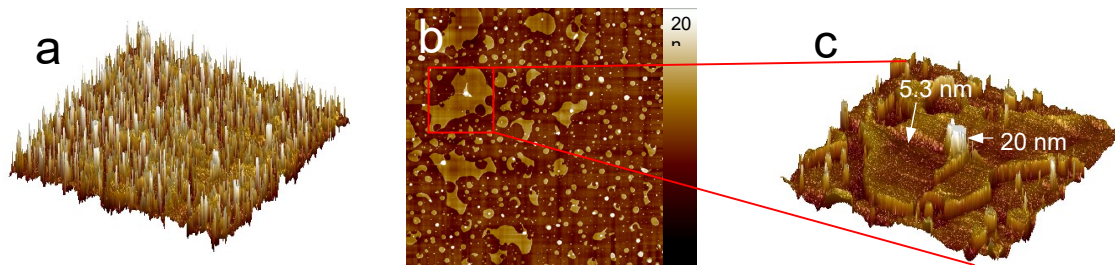


Figure 5.6 The characteristic AFM topographic images of Infasurf films at 37 °C. The AFM scan area was 20×20 μm with the full z-range of 20 nm for all 2D images. 3D images (a) show the height difference of multi-layers. Zooming-in 3D images (c) shows the detail structures of the multi-layers.

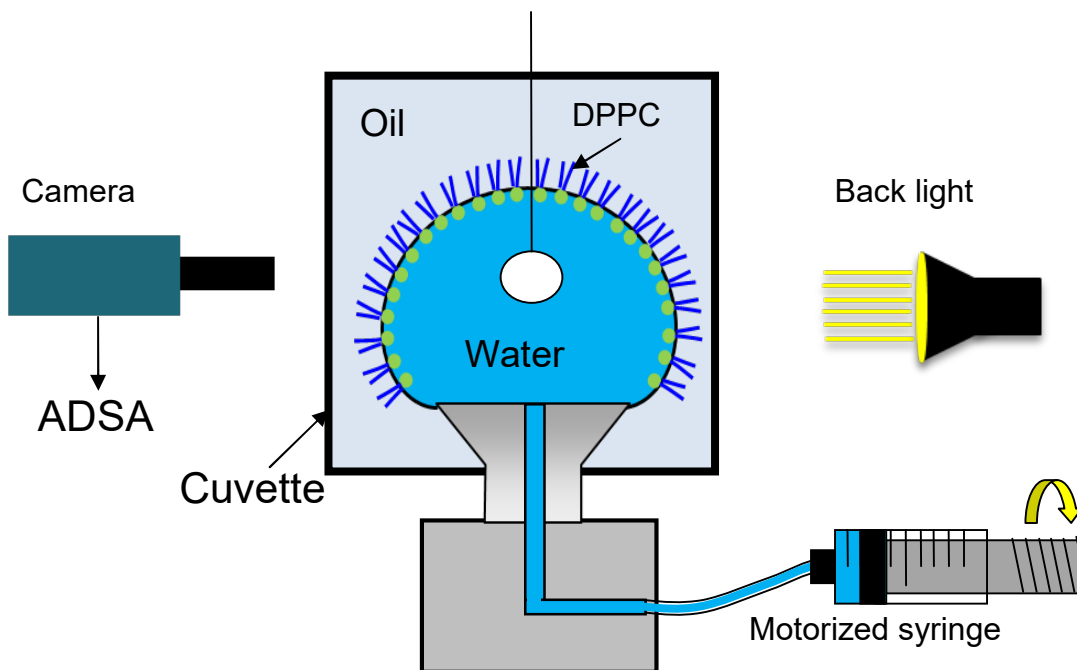


Figure 5.7 Schematic of the oil-water system. A water droplet was formed on the top of pedestal immersed inside the oil. A cuvette is used as the reservoir of the oil, from which the light can get through. The DPPC was spread on the oil-water interface using a micro-syringe. The DPPC monolayer was then compressed using the motorized syringe. At the meantime, the surface tension was monitored by ADSA in real-time. When the surface tension reaches to the value of interest, the film was deposited using a LB transfer technique.

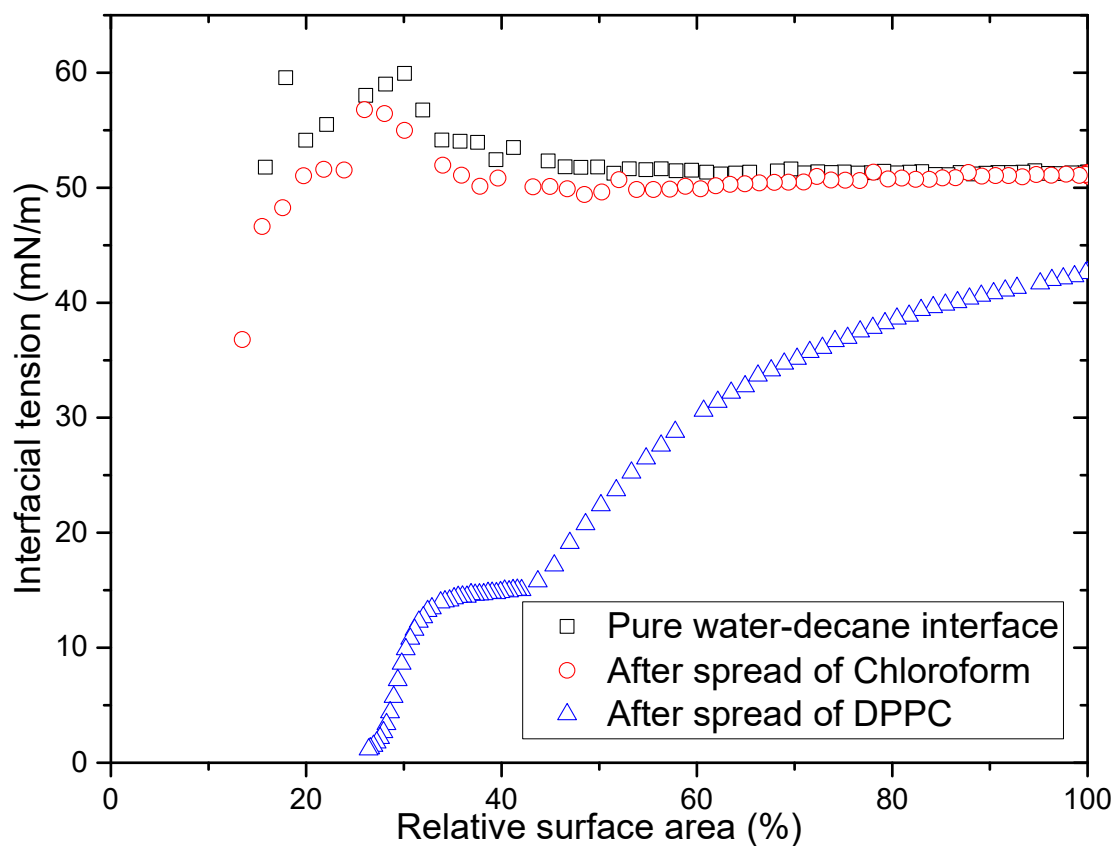


Figure 5.8 Validation of the influence of Chloroform on the isotherms. The pure oil-water interface, interface with spread Chloroform, and interface with spread DPPC were compressed. The isotherms indicate the spread of Chloroform has limited influence on the interface. The interfacial tension keeps almost constant upon compressing until at small surface area (small drop volume) where the ADSA gives inaccurate results.

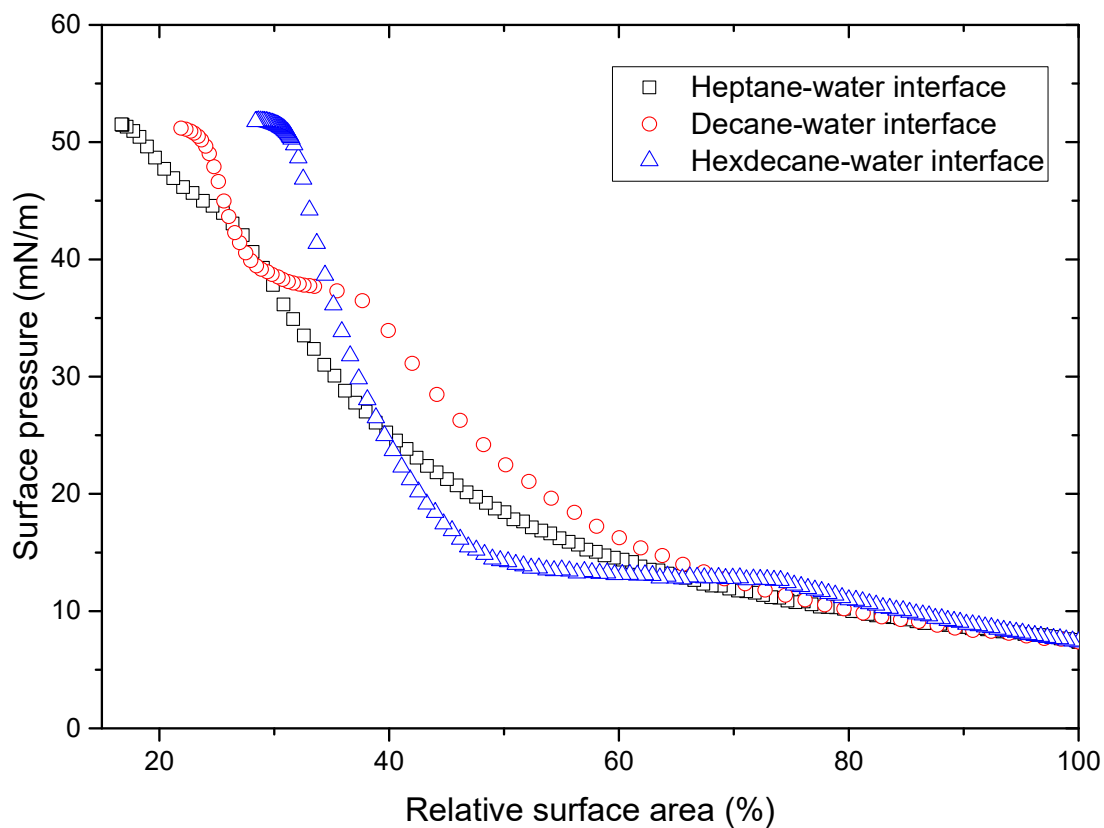


Figure 5.9 Isotherms of DPPC at three oil-water systems, i.e., heptane-water interface, decane-water interface, and hexadecane-water interface. It can be found that the oil places a significant influence on the phase transition.

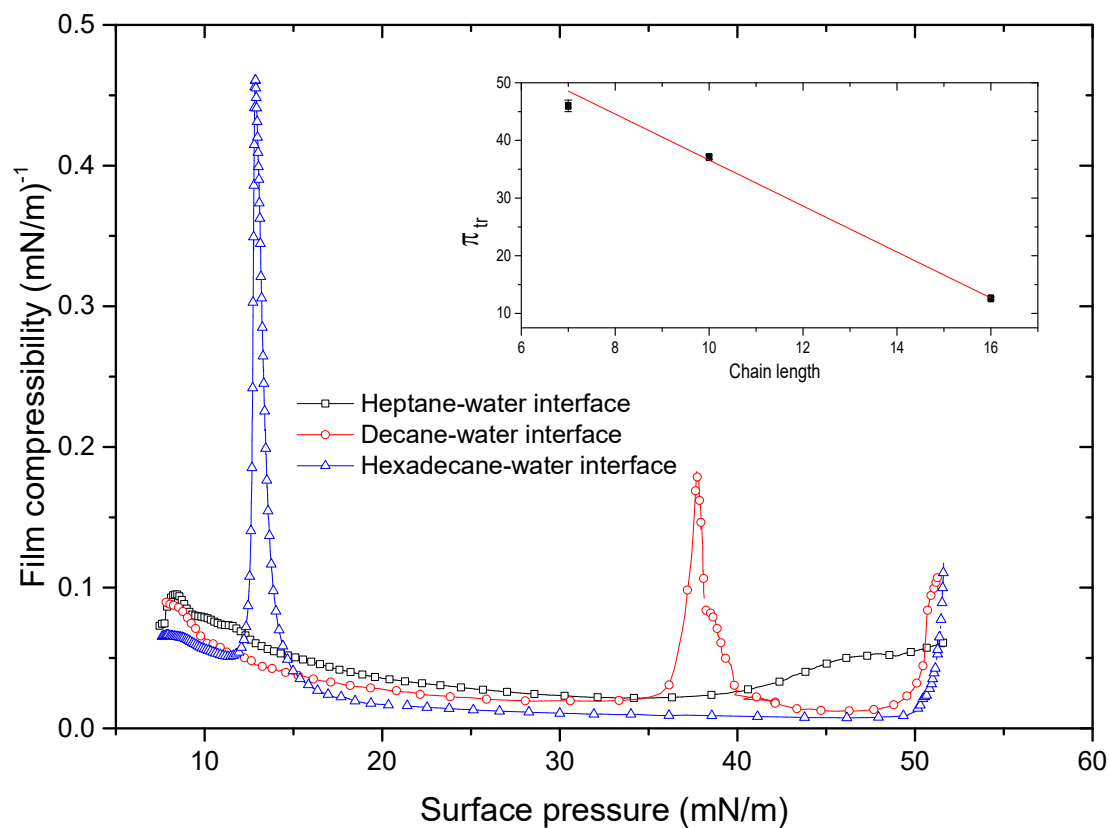


Figure 5.10 Film compressibility of DPPC monolayer in heptane-water interface, decane-water interface, and hexadecane-water interface. Locations of the peak compressibility define the surface pressure for phase transitions for the corresponding oil-water interface.

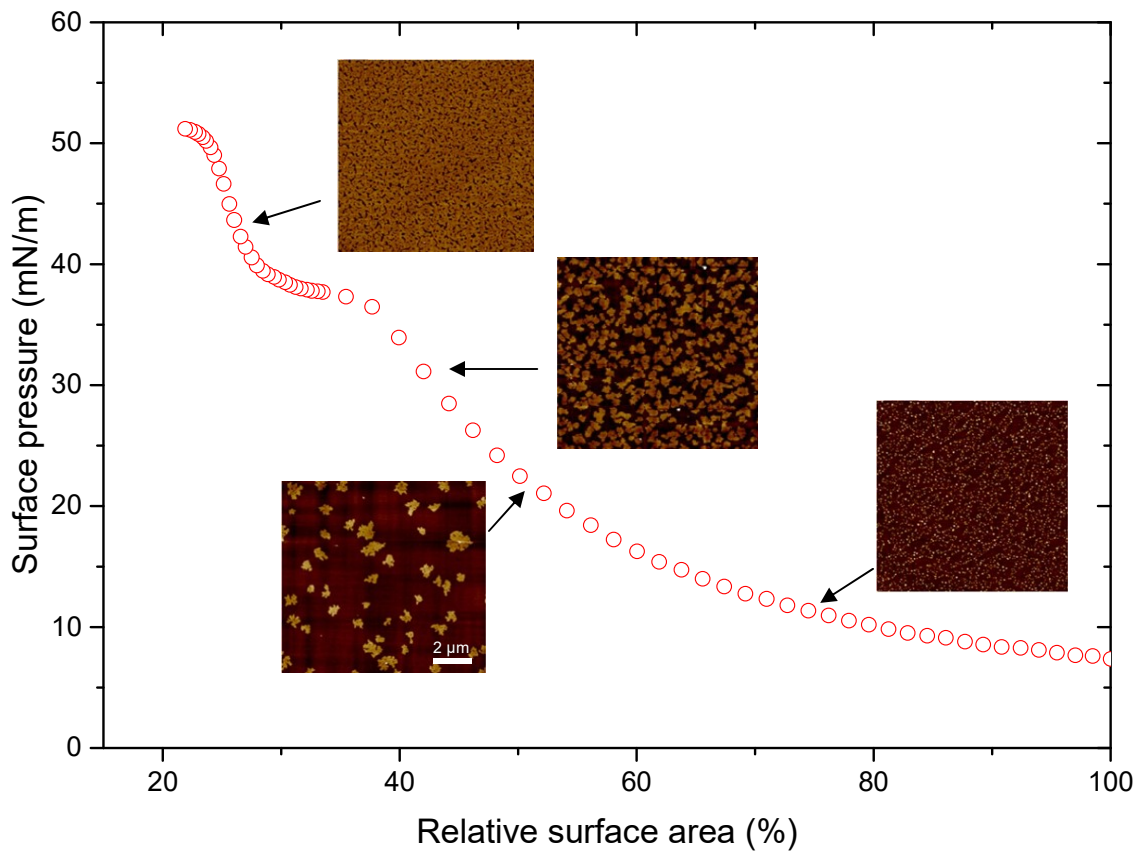


Figure 5.11 AFM topographic images of the DPPC monolayer at decane-water interface with surface pressure at 10, 20, 30, 42 mN/m. All AFM image have the same scanning size of $10 \times 10 \mu\text{m}$ and z-range of 5 nm. It can be found the growing and compacting of the domains with increasing surface pressure.

Chapter 6. Summary of main contributions and future directions

6.1 Summary of main contributions

1. We proposed a computational scheme of a unified drop/bubble coordinate system for ADSA in surface and interfacial tension measurement. Combined with ADSA, an experimental setup called the constrained drop surfactometer (CDS) was developed. The CDS is capable of measuring both surface and interfacial tensions from four configurations, *i.e.*, sessile drop, pendant drop, sessile bubble, and pendant bubble as a function of time and surface area variations. The measurements of surface tensions from six liquids and interfacial tensions from three oil-water interfaces proved the accuracy and feasibility of the CDS as a measurement tool.

2. We symmetrically studied different criteria/parameters in evaluating the accuracy of ADSA upon drop volume reduction. By scrutinizing the dependence of ADSA accuracy on the Bond number (Bo), Worthington number (Wo), and Shape parameter (Ps), for three representative systems with various capillary constants, we concluded that the classical Bo failed to predict the accuracy of drop shape analysis at very low drop volumes. We proposed the Neumann number $Ne \equiv \Delta\rho g R_0 H / \gamma$ to replace the classical Bond number in evaluating the accuracy of ADSA. The design rationale of this new dimensionless number lies in the use of the geometric mean of the radius of curvature at the drop apex (R_0) and the drop height (H) as the new characteristic length to represent the drop size, *i.e.*, $L = \sqrt{R_0 H}$. It is found that the Neumann number is capable of evaluating the accuracy of drop shape analysis. We have also demonstrated the usefulness of the

local Neumann number, $Ne_z \equiv \Delta\rho g R_0 z / \gamma$, in evaluating the contribution of the local drop profile to the surface tension measurement.

3. We developed a novel closed-loop ADSA (CL-ADSA), integrated into the CDS, for manipulating millimeter-sized droplets. CL-ADSA extends applications of the CDS from a surface tension measurement methodology to a sophisticated tool for automatically manipulating droplets in real-time. We have demonstrated the feasibility and advantages of CL-ADSA in three applications, including control of drop volume by automatically compensating natural evaporation, precise control of surface area variations for high-fidelity biophysical simulations of natural pulmonary surfactant, and steady control of surface pressure for *in situ* Langmuir-Blodgett transfer from droplets. Using CL-ADSA, CDS holds great promise for advancing droplet manipulation in a variety of material and surface science applications, such as thin-film fabrication, self-assembly, and biophysical study of pulmonary surfactant.

4. We developed a waveform generator in the CDS for surface area oscillations to study surface dilational rheology. The waveform generator can accurately oscillate surface area in a sinusoidal pattern with a wide range of frequency up to 0.2 Hz. This is, to the best of our knowledge, the first time that the surface area oscillation can be directly controlled in droplet-based experiments. We have demonstrated the feasibility and advantages of the surface area waveform generator in two applications, including the measurement of surface dilational modulus for surfactants in a wide range of concentrations and frequencies and the measurement of dynamic modulus change of two proteins during the adsorption. All these applications have demonstrated the accuracy, versatility, and applicability of this new waveform generating technique in surface rheology study.

5. We developed a double capillary holder for subphase replacement in a sessile drop. It allows the solution inside the drop to be replaced by fresh buffer without disturbing the film at the surface, thus enabling LB transfer on the adsorbed film. The subphase replacement technique was used to directly imaging the adsorbed pulmonary surfactants under physiological conditions, providing additional insight on the composition-dependent nature of the surfactant biophysical properties.

6.2 Future directions

6.2.1 Development of high-speed ADSA

In chapter 2, we have demonstrated the usefulness of local Neumann number in determining the contributions of points along the drop profile to the overall accuracy of the drop shape analysis. It was found that the contribution of points to the overall accuracy was not even along the profile. Drop profile close to the three-phase contact line contributes the most to the change of surface tension, applied for both PD and SD. The local Neumann number introduced a new way to define the weight factor in ADSA, as discussed in chapter 1. This provides a new approach to develop a high-speed ADSA with minimum sacrifice of accuracy. By scrutinizing the numerical procedure of ADSA, the number of the experimental points places a significant influence of the computational time. Specifically, the calculation of the normal distance between the experimental coordinate and the corresponding closet Laplacian profile for all points consumes most of the computational time. Thus, the reduction of experimental points is a promising way to accelerate the speed of ADSA. However, the reduction of points results in decreasing of the accuracy. The selection of points with high influence on the overall accuracy becomes essential in the development of high-speed ADSA. We will use the local Neumann

number as a guide for point selections with minimum influence on the accuracy. The high-speed ADSA will facilitate both surface tension measurement and the feed-back control system.

6.2.2. Surface dilational rheology measurement at oil-water interface

Chapter 4 demonstrated the accuracy, versatility, and applicability of the new ADSA-based waveform generator in CDS for studying surface dilational rheology of surfactants and proteins at air-water surface. Compared to the extensive literatures focusing on the air-water surface, limited information is available about the dilational rheology of proteins and surfactants at liquid-liquid interface due to the complexity and difficulty to access experimentally. In practice, a variety of dynamic processes take place at liquid-liquid interface, such as emulsion used in food industry, cosmetic, and oil recovery. Taking advantage of the CDS's capacity in measuring both surface/interfacial tension and surface rheology, as discussed in chapter 4 and chapter 5, our method is easy to be extended to the oil-water interfacial rheology study.

6.2.3 Development of the Langmuir-Schaefer transfer technique with the CDS

When the LB transfer was applied for film visualization in chapter 3 and 5, a small piece of freshly peeled mica was inserted in the droplet and then gradually lifted up to deposit the film. It was found in the experiment that the film would inevitably be disturbed during the transferring, especially in such small dimension. An alternative way to mitigate the interaction between the solid substrate and the film is to use Langmuir-Schaefer (LS) transfer technique.^{108, 109} The LS technique relies on horizontally transferring by touching the air-water interface from the airside. The film is deposit onto the substrate when touching the air-water interface instead of inserting into the subphase. However, it should be noted that the LS transfer technique requires a high hydrophobic and smooth surface, which is less accessible than the mica used in the LB transfer.

VITA

Jinlong Yang received his B.S. and M.S. degrees from the department of Mechanical Engineering, East China University of Science and Technology, Shanghai, China, in 2011 and 2014, respectively. He started his Ph.D. research in the department of Mechanical Engineering, University of Hawaii from 2014. During this graduate studies at the University of Hawaii, he worked as a research assistant in Lab of Biocolloids and Bointerfaces.

The following is a list of peer-reviewed journal papers, conference presentations published or in preparation based on the work of this thesis.

Papers published in refereed journals for publication

1. **Yang, J.**, Yu, K., & Zuo, Y. Y. (2017). Accuracy of axisymmetric drop shape analysis in determining surface and interfacial tensions. *Langmuir*, 33(36), 8914-8923.
2. Zuo, Y. Y., Chen, R., Wang, X., **Yang, J.**, Policova, Z., & Neumann, A. W. (2016). Phase transitions in dipalmitoylphosphatidylcholine monolayers. *Langmuir*, 32(33), 8501-8506.
3. Yu, K.,* **Yang, J.**,* & Zuo, Y. Y. (2016). Automated droplet manipulation using closed-loop axisymmetric drop shape analysis. *Langmuir*, 32(19), 4820-4826. (* equal contribution)
4. Schenk, H., Espino, S., Romo, D., Nima, N., Do, A., Michaud, J., Papahadjopoulos, S., **Yang, J.**, Zuo, Y. Y., Steppe, K., & Jansen, S. (2016). Xylem surfactants introduce a new element to the cohesion-tension theory. *Plant Physiology*, 173(1), 1177-1196.

Papers in preparation

1. **Yang, J.**, Yu, K., Tsuji, T., Jha, R., and Zuo, Y. Y., Surface dilational rheology measured by a droplet waveform generator. To be submitted to *ACS Applied Materials and Interfaces*.

2. Yu, K., **Yang, J.**, and Zuo, Y. Y., Arbitrary waveform generation through oscillating droplet.
To be submitted to *Applied Physics Letters*.

Conference Presentations

1. **Yang, J.**, Zuo, Y. Y., Determining surface and interfacial tensions with multiple drop and bubble configurations. *The International Chemical Congress of Pacific Basin Societies*, Hawaii, USA, 2015. (NSF travel award for this presentation)

References

1. He, Q.; Zhang, Y.; Lu, G.; Miller, R.; Möhwald, H.; Li, J. Dynamic adsorption and characterization of phospholipid and mixed phospholipid/protein layers at liquid/liquid interfaces. *Advances in colloid and interface science* **2008**, *140* (2), 67-76.
2. Cabrerizo-Vilchez, M. A.; Wege, H. A.; Holgado-Terriza, J. A.; Neumann, A. W. Axisymmetric drop shape analysis as penetration Langmuir balance. *Review of scientific instruments* **1999**, *70* (5), 2438-2444.
3. Russev, S. C.; Alexandrov, N.; Marinova, K. G.; Danov, K. D.; Denkov, N. D.; Lyutov, L.; Vulchev, V.; Bilke-Krause, C. Instrument and methods for surface dilatational rheology measurements. *Review of scientific instruments* **2008**, *79* (10), 104102.
4. Teh, S.-Y.; Lin, R.; Hung, L.-H.; Lee, A. P. Droplet microfluidics. *Lab on a Chip* **2008**, *8* (2), 198-220.
5. Neumann, A. W.; David, R.; Zuo, Y. *Applied surface thermodynamics*; CRC press 2010; Vol. 151.
6. Valle, R. P.; Wu, T.; Zuo, Y. Y. Biophysical influence of airborne carbon nanomaterials on natural pulmonary surfactant. *ACS nano* **2015**, *9* (5), 5413-21.
7. Bashforth, F.; Adams, J. C. *An attempt to test the theories of capillary action: by comparing the theoretical and measured forms of drops of fluid*; University Press 1883.
8. Fordham, S. In *On the calculation of surface tension from measurements of pendant drops*, Proceedings of the Royal Society of London A: Mathematical, Physical and Engineering Sciences, 1948; The Royal Society, pp 1-16.

9. Mills, O. Tables for use in the measurement of interfacial tensions between liquids with small density differences. *British Journal of Applied Physics* **1953**, 4 (8), 247.
10. Rotenberg, Y.; Boruvka, L.; Neumann, A. Determination of surface tension and contact angle from the shapes of axisymmetric fluid interfaces. *Journal of colloid and interface science* **1983**, 93 (1), 169-183.
11. Cheng, P.; Li, D.; Boruvka, L.; Rotenberg, Y.; Neumann, A. Automation of axisymmetric drop shape analysis for measurements of interfacial tensions and contact angles. *Colloids and Surfaces* **1990**, 43 (2), 151-167.
12. Del Río, O.; Neumann, A. Axisymmetric drop shape analysis: computational methods for the measurement of interfacial properties from the shape and dimensions of pendant and sessile drops. *Journal of colloid and interface science* **1997**, 196 (2), 136-147.
13. Zuo, Y. Y.; Veldhuizen, R. A. W.; Neumann, A. W.; Petersen, N. O.; Possmayer, F. Current perspectives in pulmonary surfactant—inhibition, enhancement and evaluation. *Biochimica et Biophysica Acta (BBA)-Biomembranes* **2008**, 1778 (10), 1947-1977.
14. Miller, R.; Aksenenko, E. V.; Zinkovych, I. I.; Fainerman, V. B. Adsorption of proteins at the aqueous solution/alkane interface: Co-adsorption of protein and alkane. *Advances in Colloid and Interface Science* **2015**, 222, 509-516.
15. Kalantarian, A.; Ninomiya, H.; Saad, S. M.; David, R.; Winklbauer, R.; Neumann, A. W. Axisymmetric drop shape analysis for estimating the surface tension of cell aggregates by centrifugation. *Biophysical journal* **2009**, 96 (4), 1606-1616.
16. Yang, D.; Gu, Y. Interfacial interactions between crude oil and CO₂ under reservoir conditions. *Petroleum science and technology* **2005**, 23 (9-10), 1099-1112.

17. Miller, R.; Ferri, J. K.; Javadi, A.; Krägel, J.; Mucic, N.; Wüstneck, R. Rheology of interfacial layers. *Colloid and Polymer Science* **2010**, *288* (9), 937-950.
18. Langevin, D. Influence of interfacial rheology on foam and emulsion properties. *Advances in Colloid and Interface Science* **2000**, *88* (1-2), 209-222.
19. Ravera, F.; Loglio, G.; Kovalchuk, V. I. Interfacial dilational rheology by oscillating bubble/drop methods. *Current Opinion in Colloid & Interface Science* **2010**, *15* (4), 217-228.
20. Lucassen, J.; Van Den Tempel, M. Dynamic measurements of dilational properties of a liquid interface. *Chemical Engineering Science* **1972**, *27* (6), 1283-1291.
21. Benjamins, J.; Lucassen-Reynders, E. Surface dilational rheology of proteins adsorbed at air/water and oil/water interfaces. *Studies in Interface Science* **1998**, *7*, 341-384.
22. Noskov, B. A.; Akentiev, A. V.; Bilibin, A. Y.; Zorin, I. M.; Miller, R. Dilational surface viscoelasticity of polymer solutions. *Advances in Colloid and Interface Science* **2003**, *104* (1), 245-271.
23. Kovalchuk, V. I.; Krägel, J.; Makievski, A. V.; Ravera, F.; Liggieri, L.; Loglio, G.; Fainerman, V. B.; Miller, R. Rheological surface properties of C12DMPO solution as obtained from amplitude- and phase-frequency characteristics of an oscillating bubble system. *Journal of Colloid and Interface Science* **2004**, *280* (2), 498-505.
24. Wantke, K.-D.; Fruhner, H. Determination of surface dilational viscosity using the oscillating bubble method. *Journal of colloid and interface science* **2001**, *237* (2), 185-199.
25. Loglio, G.; Pandolfini, P.; Miller, R.; Makievski, A.; Ravera, F.; Ferrari, M.; Liggieri, L. Drop and Bubble Shape Analysis As a Tool for Dilational Rheological Studies of Interfacial Layers. *Studies in Interface Science; Möbius, D.; Miller, R., Eds*, 439-483.

26. Stubenrauch, C.; Miller, R. Stability of foam films and surface rheology: an oscillating bubble study at low frequencies. *The Journal of Physical Chemistry B* **2004**, *108* (20), 6412-6421.
27. Kotsmar, C.; Kragel, J.; Kovalchuk, V. I.; Aksenenko, E. V.; Fainerman, V. B.; Miller, R. Dilation and shear rheology of mixed β -casein/surfactant adsorption layers. *The Journal of Physical Chemistry B* **2008**, *113* (1), 103-113.
28. Zuo, Y. Y.; Ding, M.; Bateni, A.; Hoorfar, M.; Neumann, A. W. Improvement of interfacial tension measurement using a captive bubble in conjunction with axisymmetric drop shape analysis (ADSA). *Colloids and Surfaces A: Physicochemical and Engineering Aspects* **2004**, *250* (1-3), 233-246.
29. Saad, S. M.; Neumann, A. W. Axisymmetric Drop Shape Analysis (ADSA): An Outline. *Adv Colloid Interface Sci* **2016**, *238*, 62-87.
30. Jasper, J. J. The surface tension of pure liquid compounds. *Journal of physical and chemical reference data* **1972**, *1* (4), 841-1010.
31. Korosi, G.; Kovats, E. S. Density and surface tension of 83 organic liquids. *Journal of Chemical & Engineering Data* **1981**, *26* (3), 323-332.
32. Lechner, M.; Wohlfarth, C.; Wohlfarth, B. *Surface tension of pure liquids and binary liquid mixtures*; Springer 1997.
33. Kwok, D. Y.; Hui, W.; Lin, R.; Neumann, A. W. Liquid-Fluid Interfacial-Tensions Measured by Axisymmetrical Drop Shape-Analysis - Comparison between the Pattern of Interfacial-Tensions of Liquid-Liquid and Solid-Liquid Systems. *Langmuir* **1995**, *11* (7), 2669-2673.

34. Goebel, A.; Lunkenheimer, K. Interfacial tension of the water/n-alkane interface. *Langmuir* **1997**, *13* (2), 369-372.
35. Georgiadis, A.; Maitland, G.; Trusler, J. P. M.; Bismarck, A. Interfacial Tension Measurements of the (H₂O + n-Decane + CO₂) Ternary System at Elevated Pressures and Temperatures. *J Chem Eng Data* **2011**, *56* (12), 4900-4908.
36. Ferrera, C.; Montanero, J. M.; Cabezas, M. G. An analysis of the sensitivity of pendant drops and liquid bridges to measure the interfacial tension. *Measurement Science and Technology* **2007**, *18* (12), 3713-3723.
37. Neeson, M. J.; Chan, D. Y.; Tabor, R. F. Compound pendant drop tensiometry for interfacial tension measurement at zero bond number. *Langmuir* **2014**, *30* (51), 15388-15391.
38. Hoorfar, M.; Kurz, M. A.; Neumann, A. W. Evaluation of the surface tension measurement of axisymmetric drop shape analysis (ADSA) using a shape parameter. *Colloids and Surfaces A: Physicochemical and Engineering Aspects* **2005**, *260* (1-3), 277-285.
39. Saad, S. M. I.; Policova, Z.; Acosta, E. J.; Neumann, A. W. Range of validity of drop shape techniques for surface tension measurement. *Langmuir* **2010**, *26* (17), 14004-14013.
40. Berry, J. D.; Neeson, M. J.; Dagastine, R. R.; Chan, D. Y. C.; Tabor, R. F. Measurement of surface and interfacial tension using pendant drop tensiometry. *Journal of Colloid and Interface Science* **2015**, *454*, 226-237.
41. Bond, W. N.; Newton, D. A. LXXXII. Bubbles, drops, and Stokes' law. (Paper 2). *The London, Edinburgh, and Dublin Philosophical Magazine and Journal of Science* **1928**, *5* (30), 794-800.
42. Berg, J. C. *An Introduction to Interfaces and Colloids: The Bridge to Nanoscience*; World Scientific: Singapore, 2010.

43. Alvarez, N. J.; Walker, L. M.; Anna, S. L. A non-gradient based algorithm for the determination of surface tension from a pendant drop: Application to low Bond number drop shapes. *Journal of colloid and interface science* **2009**, *333* (2), 557-562.
44. Saad, S. M. I.; Neumann, A. W. Total Gaussian curvature, drop shapes and the range of applicability of drop shape techniques. *Advances in Colloid and Interface Science* **2014**, *204*, 1-14.
45. Saad, S. M.; Neumann, A. W. Total Gaussian curvature, drop shapes and the range of applicability of drop shape techniques. *Advances in colloid and interface science* **2014**, *204*, 1-14.
46. Malcolm, J. D.; Elliott, C. D. Interfacial tension from height and diameter of a single sessile drop or captive bubble. *The Canadian Journal of Chemical Engineering* **1980**, *58* (2), 151-153.
47. Prokop, R. M.; Rio, O. I. D.; Niyakan, N.; Neumann, A. W. Interfacial tension from the height and diameter of sessile drops and captive bubbles with an arbitrary contact angle. *The Canadian Journal of Chemical Engineering* **1996**, *74* (4), 534-541.
48. Kalantarian, A.; David, R.; Chen, J.; Neumann, A. W. Simultaneous Measurement of Contact Angle and Surface Tension Using Axisymmetric Drop-Shape Analysis-No Apex (ADSA-NA). *Langmuir* **2011**, *27* (7), 3485-3495.
49. He, Q.; Zhang, Y.; Lu, G.; Miller, R.; Mohwald, H.; Li, J. Dynamic adsorption and characterization of phospholipid and mixed phospholipid/protein layers at liquid/liquid interfaces. *Adv Colloid Interface Sci* **2008**, *140* (2), 67-76.
50. Cabrerizo-Vilchez, M. A.; Wege, H. A.; Holgado-Terriza, J. A.; Neumann, A. W. Axisymmetric drop shape analysis as penetration Langmuir balance. *Rev Sci Instrum* **1999**, *70* (5), 2438-2444.

51. Russev, S. C.; Alexandrov, N.; Marinova, K. G.; Danov, K. D.; Denkov, N. D.; Lyutov, L.; Vulchev, V.; Bilke-Krause, C. Instrument and methods for surface dilatational rheology measurements. *The Review of scientific instruments* **2008**, *79* (10), 104102.
52. Baratian, D.; Cavalli, A.; van den Ende, D.; Mugele, F. On the shape of a droplet in a wedge: new insight from electrowetting. *Soft matter* **2015**, *11* (39), 7717-7721.
53. Gong, J.; Kim, C.-J. All-electronic droplet generation on-chip with real-time feedback control for EWOD digital microfluidics. *Lab on a Chip* **2008**, *8* (6), 898-906.
54. Miller, E.; Rotea, M.; Rothstein, J. P. Microfluidic device incorporating closed loop feedback control for uniform and tunable production of micro-droplets. *Lab on a Chip* **2010**, *10* (10), 1293-1301.
55. Wege, H. A.; Holgado-Terriza, J. A.; Cabrerizo-Vilchez, M. A. Development of a constant surface pressure penetration langmuir balance based on axisymmetric drop shape analysis. *J Colloid Interface Sci* **2002**, *249* (2), 263-73.
56. Zhang, H.; Fan, Q.; Wang, Y. E.; Neal, C. R.; Zuo, Y. Y. Comparative study of clinical pulmonary surfactants using atomic force microscopy. *Biochimica et biophysica acta* **2011**, *1808*, 1832-1842.
57. Zhang, H.; Wang, Y. E.; Fan, Q.; Zuo, Y. Y. On the low surface tension of lung surfactant. *Langmuir* **2011**, *27* (13), 8351-8358.
58. Yu, K.; Yang, J.; Zuo, Y. Y. Automated droplet manipulation using closed-loop axisymmetric drop shape analysis. *Langmuir* **2016**, *32* (19), 4820-4826.
59. Valle, R. P.; Huang, C. L.; Loo, J. S. C.; Zuo, Y. Y. Increasing Hydrophobicity of Nanoparticles Intensifies Lung Surfactant Film Inhibition and Particle Retention. *ACS Sustainable Chemistry & Engineering* **2014**, *2* (7), 1574-1580.

60. Dagan, M. P.; Hall, S. B. The Equilibrium Spreading Tension of Pulmonary Surfactant. *Langmuir* **2015**, *31* (48), 13063-7.
61. Jasper, J. J. The surface tension of pure liquid compounds. *J. Phys. Chem. Ref. Data* **1972**, *1* (4), 841-1009.
62. Saad, S. M.; Neumann, A. W. Total Gaussian curvature, drop shapes and the range of applicability of drop shape techniques. *Adv Colloid Interface Sci* **2014**, *204*, 1-14.
63. Miller, R.; Fainerman, V. B.; Makievski, A. V.; Kragel, J.; Grigoriev, D. O.; Kazakov, V. N.; Sinyachenko, O. V. Dynamics of protein and mixed protein/surfactant adsorption layers at the water/fluid interface. *Adv Colloid Interface Sci* **2000**, *86* (1-2), 39-82.
64. Mitropoulos, V.; Mütze, A.; Fischer, P. Mechanical properties of protein adsorption layers at the air/water and oil/water interface: A comparison in light of the thermodynamical stability of proteins. *Advances in Colloid and Interface Science* **2014**, *206*, 195-206.
65. Tankovsky, N.; Zografov, N.; Andreeva, A. Gas-adsorption dynamics at the water–air interface, revealed by resonant droplet tensiometry. *Chemical Engineering Science* **2016**, *144*, 283-287.
66. Bonaccorso, E.; Butt, H. J. Microdrops on atomic force microscope cantilevers: evaporation of water and spring constant calibration. *The journal of physical chemistry. B* **2005**, *109* (1), 253-63.
67. Bachofen, H.; Schurch, S.; Urbinelli, M.; Weibel, E. R. Relations among alveolar surface tension, surface area, volume, and recoil pressure. *J. Appl. Physiol.* **1987**, *62* (5), 1878-1887.
68. Bachofen, H.; Schürch, S. Alveolar surface forces and lung architecture. *Comparative Biochemistry and Physiology - A Molecular and Integrative Physiology* **2001**, *129* (1), 183-193.

69. Kcharge, A. B.; Wu, Y.; Perlman, C. E. Surface tension in situ in flooded alveolus unaltered by albumin. *Journal of Applied Physiology* **2014**, *117* (5), 440-451.
70. Pikhova, B.; Schram, V.; Hall, S. B. Pulmonary surfactant: phase behavior and function. *Current opinion in structural biology* **2002**, *12* (4), 487-94.
71. Possmayer, F.; Hall, S. B.; Haller, T.; Petersen, N. O.; Zuo, Y. Y.; Bernardino de la Serna, J.; Postle, A. D.; Veldhuizen, R. A. W.; Orgeig, S. Recent advances in alveolar biology: Some new looks at the alveolar interface. *Respiratory Physiology & Neurobiology* **2010**, *173* (Supplement 1), S55-S64.
72. Rugonyi, S.; Biswas, S. C.; Hall, S. B. The biophysical function of pulmonary surfactant. *Respiratory physiology & neurobiology* **2008**, *163* (1-3), 244-55.
73. Yan, W.; Biswas, S. C.; Laderas, T. G.; Hall, S. B. The melting of pulmonary surfactant monolayers. *J Appl Physiol* **2007**, *102* (5), 1739-45.
74. Saad, S. M.; Policova, Z.; Acosta, E. J.; Hair, M. L.; Neumann, A. W. Mixed DPPC/DPPG monolayers at very high film compression. *Langmuir* **2009**, *25* (18), 10907-12.
75. Kaganer, V. M.; Mohwald, H.; Dutta, P. Structure and phase transitions in Langmuir monolayers. *Rev. Mod. Phys.* **1999**, *71* (3), 779-819.
76. Keating, E.; Zuo, Y. Y.; Tadayyon, S. M.; Petersen, N. O.; Possmayer, F.; Veldhuizen, R. A. A modified squeeze-out mechanism for generating high surface pressures with pulmonary surfactant. *Biochim Biophys Acta* **2012**, *1818* (5), 1225-34.
77. Zuo, Y. Y.; Veldhuizen, R. A.; Neumann, A. W.; Petersen, N. O.; Possmayer, F. Current perspectives in pulmonary surfactant--inhibition, enhancement and evaluation. *Biochimica et biophysica acta* **2008**, *1778* (10), 1947-77.

78. McConlogue, C. W.; Vanderlick, T. K. A close look at domain formation in DPPC monolayers. *Langmuir* **1997**, *13* (26), 7158-7164.
79. Miller, R.; Liggieri, L. *Interfacial rheology*; CRC Press 2009; Vol. 1.
80. Möbius, D.; Miller, R. *Proteins at liquid interfaces*; Elsevier 1998; Vol. 7.
81. Georgieva, D.; Schmitt, V.; Leal-Calderon, F.; Langevin, D. On the possible role of surface elasticity in emulsion stability. *Langmuir* **2009**, *25* (10), 5565-5573.
82. Noskov, B.; Latnikova, A.; Lin, S.-Y.; Loglio, G.; Miller, R. Dynamic surface elasticity of β -casein solutions during adsorption. *The Journal of Physical Chemistry C* **2007**, *111* (45), 16895-16901.
83. Noskov, B. A.; Milyaeva, O. Y.; Lin, S.-Y.; Loglio, G.; Miller, R. Dynamic properties of β -casein/surfactant adsorption layers. *Colloids and Surfaces A: Physicochemical and Engineering Aspects* **2012**, *413*, 84-91.
84. Benjamins, J.; Lyklema, J.; Lucassen-Reynders, E. Compression/expansion rheology of oil/water interfaces with adsorbed proteins. Comparison with the air/water surface. *Langmuir* **2006**, *22* (14), 6181-6188.
85. del Rio, O.; Neumann, A. W. Axisymmetric drop shape analysis: computational methods for the measurement of interfacial properties from the shape and dimensions of pendant and sessile drops. *Journal of colloid and interface science* **1997**, *196* (2), 136-147.
86. Yang, J.; Yu, K.; Zuo, Y. Y. Accuracy of Axisymmetric Drop Shape Analysis in Determining Surface and Interfacial Tensions. *Langmuir* **2017**, *33* (36), 8914-8923.
87. Laura, M.; Lu, J. J.; Chan, Y. W.; Ng, A.; Zhang, L.; Hoorfar, M.; Policova, Z.; Grundke, K.; Neumann, A. W. Constrained sessile drop as a new configuration to measure low surface tension in lung surfactant systems. *Journal of Applied Physiology* **2004**, *97* (2), 704-715.

88. Joos, P. Approach for an equation of state for adsorbed protein surfaces. *Biochimica et Biophysica Acta (BBA)-Biomembranes* **1975**, *375* (1), 1-9.
89. Loglio, G.; Pandolfini, P.; Miller, R.; Makievski, A.; Krägel, J.; Ravera, F. Oscillation of interfacial properties in liquid systems: Assessment of harmonic distortion. *Physical Chemistry Chemical Physics* **2004**, *6* (7), 1375-1379.
90. Leser, M. E.; Acquistapace, S.; Cagna, A.; Makievski, A. V.; Miller, R. Limits of oscillation frequencies in drop and bubble shape tensiometry. *Colloids and Surfaces A: Physicochemical and Engineering Aspects* **2005**, *261* (1-3), 25-28.
91. Hoorfar, M.; W. Neumann, A. Recent progress in Axisymmetric Drop Shape Analysis (ADSA). *Advances in Colloid and Interface Science* **2006**, *121* (1-3), 25-49.
92. Fainerman, V. B.; Lylyk, S. V.; Aksenenko, E. V.; Petkov, J. T.; Yorke, J.; Miller, R. Surface tension isotherms, adsorption dynamics and dilational visco-elasticity of sodium dodecyl sulphate solutions. *Colloids and Surfaces A: Physicochemical and Engineering Aspects* **2010**, *354* (1-3), 8-15.
93. Fainerman, V. B.; Lucassen-Reynders, E. H.; Miller, R. Description of the adsorption behaviour of proteins at water/fluid interfaces in the framework of a two-dimensional solution model. *Advances in Colloid and Interface Science* **2003**, *106* (1-3), 237-259.
94. Miller, R.; Fainerman, V. B.; Aksenenko, E. V.; Leser, M. E.; Michel, M. Dynamic Surface Tension and Adsorption Kinetics of β -Casein at the Solution/Air Interface. *Langmuir* **2004**, *20* (3), 771-777.
95. Maldonado-Valderrama, J.; Wege, H. A.; Rodríguez-Valverde, M. A.; Gálvez-Ruiz, M. J.; Cabrerizo-Vílchez, M. A. Comparative Study of Adsorbed and Spread β -Casein Monolayers at the Water–Air Interface with the Pendant Drop Technique. *Langmuir* **2003**, *19* (20), 8436-8442.

96. Lucassen-Reynders, E. H.; Fainerman, V. B.; Miller, R. Surface Dilational Modulus or Gibbs' Elasticity of Protein Adsorption Layers. *The Journal of Physical Chemistry B* **2004**, *108* (26), 9173-9176.
97. Casção Pereira, L. G.; Théodoly, O.; Blanch, H. W.; Radke, C. J. Dilatational rheology of BSA conformers at the air/water interface. *Langmuir* **2003**, *19* (6), 2349-2356.
98. Jansen, S.; Schenk, H. J. On the ascent of sap in the presence of bubbles. *American Journal of Botany* **2015**, *102* (10), 1561-1563.
99. Gartner, B. L.; Moore, J. R.; Gardiner, B. A. Gas in stems: abundance and potential consequences for tree biomechanics. *Tree Physiology* **2004**, *24* (11), 1239-1250.
100. Schenk, H. J.; Espino, S.; Romo, D. M.; Nima, N.; Do, A. Y.; Michaud, J. M.; Papahadjopoulos-Sternberg, B.; Yang, J.; Zuo, Y. Y.; Steppe, K. Xylem surfactants introduce a new element to the cohesion-tension theory. *Plant physiology* **2016**, pp. 01039.2016.
101. Zhang, H.; Fan, Q.; Wang, Y. E.; Neal, C. R.; Zuo, Y. Y. Comparative study of clinical pulmonary surfactants using atomic force microscopy. *Biochimica et Biophysica Acta (BBA)-Biomembranes* **2011**, *1808* (7), 1832-1842.
102. Veldhuizen, R.; Nag, K.; Orgeig, S.; Possmayer, F. The role of lipids in pulmonary surfactant. *Biochimica et Biophysica Acta (BBA)-Molecular Basis of Disease* **1998**, *1408* (2), 90-108.
103. Postle, A. D.; Heeley, E. L.; Wilton, D. C. A comparison of the molecular species compositions of mammalian lung surfactant phospholipids. *Comparative Biochemistry and Physiology Part A: Molecular & Integrative Physiology* **2001**, *129* (1), 65-73.
104. Notter, R. H. *Lung surfactants: basic science and clinical applications*; CRC Press 2000.

105. Martin, J. A.; Hamilton, B. E.; Sutton, P. D.; Ventura, S. J.; Menacker, F.; Munson, M. L. Births: final data for 2002. *National vital statistics reports : from the Centers for Disease Control and Prevention, National Center for Health Statistics, National Vital Statistics System* **2003**, 52 (10), 1-113.
106. Pichot, R.; Watson, R. L.; Norton, I. T. Phospholipids at the interface: current trends and challenges. *International journal of molecular sciences* **2013**, 14 (6), 11767-11794.
107. Zuo, Y. Y.; Chen, R.; Wang, X.; Yang, J.; Policova, Z.; Neumann, A. W. Phase Transitions in Dipalmitoylphosphatidylcholine Monolayers. *Langmuir* **2016**, 32 (33), 8501-8506.
108. Langmuir, I.; Schaefer, V. J. Activities of Urease and Pepsin Monolayers. *Journal of the American Chemical Society* **1938**, 60 (6), 1351-1360.
109. Lee, S.; Virtanen, J. A.; Virtanen, S. A.; Penner, R. M. Assembly of fatty acid bilayers on hydrophobic substrates using a horizontal deposition procedure. *Langmuir : the ACS journal of surfaces and colloids* **1992**, 8 (5), 1243-1246.